Lorentz force velocimetry in liquid metal two-phase flow applications

Dissertation

zur Erlangung des akademischen Grades

Doktoringenieur (Dr.-Ing.)

vorgelegt der

Fakultät für Maschinenbau der
Technischen Universität Ilmenau

von Herrn

M.Sc. Ze Lyu

geboren am 26. März 1990 in Sichuan, China

1. Gutachter:	apl. Prof. Dr.-Ing. habil. Christian Karcher, Ilmenau
2. Gutachter:	PD Dr. rer. nat. habil. Thomas Boeck, Ilmenau
3. Gutachter:	Univ.-Prof. Dr. rer. nat. habil. André Thess, Stuttgart

Tag der Einreichung:	06. November 2018
Tag der wissenschaftlichen Aussprache:	28. Februar 2019

urn:nbn:de:gbv:ilm1-2019000035

Abstract

Two-phase flows of an electrically conducting liquid occur in a number of metallurgical processes. For example, in continuous casting of steel, argon bubbles are injected in order to prevent clogging of the submerged entry nozzle. Bubbles are also introduced into the stirring ladle during steel production to mix the melt in the mold and to catch impurities to the bath surface, where they can be then selectively excluded. For the purpose of process and quality controls, it is necessary to measure and record such transport process of two-phase flows.

Among the various methods to measure them, one promising candidate is the so-called Lorenz force velocimetry (LFV). It is based on measuring the flow-induced force acting on an externally arranged permanent magnet near the flow. According to the scaling-laws of Magnetohydrodynamic (MHD), this Lorentz force is proportional to the electrical conductivity and velocity of the melt. LFV has the significant advantage of being contact-less, which allows it to perform measurements of local velocity distribution or determination of global flow rate in hot and chemically aggressive substances even in industrial applications in the high temperature range. The functionality of LFV has already been demonstrated in a series of laboratory experiments of alloy GaInSn at room-temperature as well as in field tests in the aluminum and steel sectors.

Motivated by applying this measurement method to liquid metal two-phase flows and thus to extend applications of LFV to industrially relevant problems, a series of model experiments with liquid GaInSn are carried out, by which electrically non-conductive gas bubbles or solid particles move inside liquid metal. The aim of the investigations is to demonstrate whether the measured force signals can be used to make reproducible statements about bubble or particle size as well as their velocity and position. The difficulty of this task is that the electrically non-conductive bubbles or particles are not directly detectable by LFV, but only their dynamic interactions with the melt.

In the present work, the Lorentz force is measured by an Interferometric-Optic-Force-Sensor (IOFS) coupled with a small cubic NdFeB-based permanent magnet. The reproducible Lorentz force signals for particles and bubbles are recorded and evaluated. Corresponding numerical models show good agreement with the measurements, and they are used to explore larger parameter spaces. We analyze the dependence of the peak values of Lorentz force on the particle velocity, particle diameter, magnetic field strength as well as the distance between particle and liquid. These results form the basis for the application of LFV for detecting particle or bubble in liquid metal flows. Two further tests of LFV for bubbles rising in liquid tin at high temperature and in liquid GaInSn under ambient magnetic field ($\sim$ 1 T) are achieved respectively. They show the functionality of LFV for particle or bubble detection not only in laboratory environment but also under harsh industrial-production conditions.

Zusammenfassung

Zweiphasenströmungen elektrischer leitfähiger Flüssigkeiten treten in einer Reihe von metallurgischen Prozessen auf. Zum Beispiel werden beim Stranggießen von Stahl Argonblasen in die Schmelze eingelassen, um ein Zusetzen des Tauchrohrs durch das Anlagern von Oxiden zu verhindern, die Schmelze in der Kokille zu mischen und zu homogenisieren sowie Verunreinigungen an die Badoberfläche zu transportieren, wo diese dann gezielt abgezogen werden können. Für eine lückenlose Prozess- und Qualitätskontrolle ist es unabdingbar, solche zweiphasigen Strömungstransportvorgänge messtechnisch zu erfassen.

Unter den verschiedenen Strömungsmessverfahren für Flüssigmetalle ist die neu entwickelte Lorentzkraft-Anemometrie (LKA) ein vielversprechender Variante. Sie beruht auf der Messung der strömungsinduzierten Kraft, die sogenannte Lorentzkraft, die auf ein extern in der Nähe der Strömung angeordnetes Permanentmagnetsystem wirkt. Diese Lorentzkraft ist nach den Gesetzmäßigkeiten der Magnetofluiddynamik direkt proportional zur Geschwindigkeit bzw. zur Durchflussmenge der Schmelzenströmung und der elekrischen Leitfähigkeit der Schmelze. Der wesentliche Vorteil der LKA ist ihr berührungsfreier und nicht intrusiver Charakter, der es auch bei industriellen Anwendungen im Hochtemperaturbereich erlaubt, Messungen zur lokalen Geschwindigkeitsverteilung bzw. Bestimmung des globalen Durchflusses in heißen und chemisch aggressiven Substanzen durchzuführen. Die Funktionalität der LKA wurde bereits in einer Reihe von Laborexperimenten mit der bei Raumtemperatur schmelzflüssigen Modelllegierung GaInSn sowie in Feldtests im Aluminium- und Stahlbereich nachgewiesen.

Die vorliegende Arbeit setzt sich zum Ziel, dieses Messverfahren auf Flüssigmetall-Zweiphasenströmungen anzuwenden und damit den Einsatzbereich der LKA auf industriell relevante Problemstellungen zu erweitern. Hierzu werden eine Reihe von Modellexperimenten mit der Testschmelze GaInSn durchgeführt, in denen sich elektrisch nicht leitfähige Gasblasen oder Festkörperpartikel bewegen. Das Ziel der Untersuchungen ist die Beantwortung der Frage, ob aus den gemessenen Kraftsignalen reproduzierbare Aussagen über Blasen- bzw. Partikelgröße sowie deren Geschwindigkeit und Position treffen lassen. Die Schwierigkeit bei dieser Aufgabe besteht darin, dass die elektrisch nicht leitfähigen Blasen oder Partikel nicht direkt mittels LKA detektierbar sind, sondern nur ihre dynamischen Wechselwirkungen mit der Schmelze.

In allen Experimenten erfolgt die Kraftmessung durch einen interferometrisch-optischen Kraftsensor (IOFS), der an einen kleinen würfelförmigen Permanentmagnet auf NdFeB-Basis gekoppelt ist. Die Kraftsignale für Partikel und Blasen werden erfasst und ausgewertet. Im

Detail werden die Abhängigkeit des Maximalwertes der Lorentzkraft vom Partikeldurchmesser, von der Magnetfeldstärke, vom Abstand zwischen Partikel und Wand sowie der Partikelgeschwindigkeit analysiert. Die Ergebnisse bilden die Grundlage für die erfolgreiche Anwendung der LKA zur Partikel- oder Blasenerkennung in Flüssigmetallströmungen. Die experimentellen Untersuchungen werden zudem durch entsprechende numerischen Simulationen flankiert. Es zeigen sich gute bis sehr gute eine gute Übereinstimmungen zwischen den experimentellen Beobachtungen und den theoretischen Voraussagen. In zwei weiteren Testexperimenten, in denen die Dynamik von aufsteigenden Blasen in einer Hochtemperaturschmelze und unter dem Einfluss eines starken Hintergrundmagnetfelds (bis 1 T) mittels LKA analysiert werden, bestätigen die Leistungsfähigkeit der Messmethode nicht nur unter Laborbedingungen, sondern auch unter rauen industrienahen Produktionsbedingungen.

Contents

Chapter 1

Introduction

1.1 Motivation

Two-phase flows of an electrically conducting liquid occur in a number of metallurgical processes. For example, in continuous casting of steel, argon bubbles are injected in order to prevent clogging of the submerged entry nozzle. Bubbles are also introduced into the stirring ladle during steel production to mix the melt in the mold and to transport impurities to the bath surface, where they can be then selectively excluded. The investigations on liquid metal two-phase flows have a long history (details in section 2.3.1), which are not only of fundamental interest but also of practical importance. There exists various methods to measure liquid metal flows, which will be described later in section 2.3.2. Among them, one promising candidate is the termed Lorentz force velocimetry (LFV) [123], which is based on measuring the flow-induced force acting on an externally arranged permanent magnet near the flow.

Non-contact is the main advantage of LFV, since by other intrusive approaches the wetting or electric contact between the probe and liquid metal is alway crucial and challenging. Earlier work has demonstrated the capability of LFV to evaluate the overall flow rate [123] as well as the local velocity in the vicinity of the magnet [41]. LFV is also proved to be robust in high-temperature plant-environment [53, 137]. A review of the state-of-the-art of LFV is illustrated in section 2.3.3. However, concerning LFV for two-phase flow applications, there exists few investigations to the author's knowledge. The following pioneer studies have connections to such topic:

- Some colleagues performed non-destructive testing of solid body defects by the termed Lorentz force eddy current testing (LET) [12, 131, 149]. They investigated the perturbations on Lorentz force due to the effects of non-conducting defects in solid metal, which is moving at a constant speed near LET system. Such effect plays a role in liquid metal two-phase flow as well, because the bubbles and particles in liquid metal are often non-conducting and can be considered as "defects" in the liquid domain. Compared to the solid body case, Lorentz forces of liquid metal two-phase flow should have more fluctuations due to the effects of local flows.

- One preliminary test of LFV for bubble detection was done by C. Heinicke. She injected argon bubbles into a vessel of liquid metal initially at rest. LFV was installed on the side of the vessel to record the perturbations on Lorentz force due to the local flow induced by the bubble motions.

- Another test was performed by F. Samsami. She moved a magnet below a layer of liquid metal initially at rest and thus the displacement flow was generated (so-called "magnetic obstacle"). LFV was installed on the side of the vessel to record the perturbations. The fluctuating Lorentz force should reflect the vortices.

However the latter two experiments have restrictions on the configurations due to limited time. There exist brief internal reports however no publication.

Inspired by the previous investigations and motivated by extending LFV to broader applications, the present work focus on the feasibility study of LFV in liquid metal two-phase flow applications.

1.2 Scope of the thesis

Due to the complexity of two-phase flows, we start in this work with a simplified configuration, where particles or bubbles move in a vertical tube of liquid metal initially at rest. We focus on the experimental investigations. Some numerical modelings are performed on the side. The goal of the present work is the feasibility study of LFV to detect liquid metal flow around bubbles or particles. We aim to answer the following general questions:

- What is the reaction on LFV in the vicinity of electrically conducting flow around particle or bubble, and conversely, what is its influence on the flow?

- Is it feasible to detect particle or bubble in liquid metal using LFV? If so, how much information of the flow around bubbles or particles can we reconstruct from the Lorentz force measurement?

- Which algorithm or method suits best for the processing of Lorentz force signals?

- Is LFV also suitable for such flow in harsh environment, so that it can be further developed for industrial applications?

- What are the advantages and limitations of LFV for such applications?

Unless stated otherwise, the working fluid is eutectic alloy consisting of gallium, indium, and tin - GaInSn. In particle experiments, the rigid non-conducting plastic sphere is used to model the particle and its velocity is controlled by an linear driver. In bubble investigations, the argon is injected via a nozzle on the bottom of liquid container and a constant volume for each bubble is maintained. The effects of bubble's deformation or expansion during rising process are neglected in numerical investigations. A customized Interferometric-Optic-Force-Sensor (IOFS) with a cubic magnet attached to it serves as the LFV sensor. Its principle will be illustrated in section 2.5. The detailed problem definition is described in section 3.1 later.

The thesis is structured as follows. In chapter 2 we describe the physical model of the problem and state-of-the-art. An overview of the principle of the IOFS used in the present work is also provided. In chapter 3 we focus on the experiments of particle motion in liquid GaInSn. Later on, in chapter 4 the experiments of bubble rising in liquid GaInSn are presented. Chapter 4 includes the additional experimental tests of bubble rising in liquid tin at high temperature and bubble rising in GaInSn under horizontal ambient magnetic field, which shows the capability of LFV under harsh environments. Finally, in chapter 5 we summarize the present work and give an outlook.

Chapter 2

Background

This chapter gives firstly a brief introduction to MHD. In section 2.2 the governing equations of MHD are described. The state-of-the-art in the field of liquid metal two-phase flow and its measurement techniques is described in sections 2.3.1 and 2.3.2 respectively. Section 2.3.3 shows the previous studies of LFV for various applications and their link to the present work. The principle of LFV in the present work and its technical details are shown in sections 2.4 and 2.5, respectively.

2.1 Short introduction to Magnetohydrodynamics

Magnetohydrodynamics (MHD) is the study of electromagnetic interaction of magnetic fields and conducting fluids. The word "magnetohydrodynamics" is derived from magneto- meaning magnetic field and hydrodynamics meaning fluid mechanics. The fluids in question must be electrically conducting and non-magnetic, and examples of such fluids include liquid metals (such as mercury, gallium, sodium, molten iron, etc.), hot ionised gases (plasmas) and electrolytes. The field of MHD became apparent by Hartmann (1937), when he performed experiments on liquid metal channel flow in magnetic field. Later on, the discovery of Alfvén wave [3] is a significant milestone. Nowadays, after decades of research, fruitful progress has been made to develop MHD theory and its applications, e.g. [15]:

- **Astrophysics**. It is now estimated that about 99% of the known universe is plasma, where MHD plays a significant role. The phenomena such as the Alfvén wave, accretion processes, sunspots, solar wind are all related to MHD.
- **Geophysics**, in which dynamo theory is used to explain the presence of anomalously long-lived magnetic fields in astrophysical bodies such as Earth or Sun. Researchers are also attempting to confirm the correlation between earthquakes and MHD phenomena of earth.
- **Engineering**. MHD is related to engineering problems such as MHD power generator, crystal growth, nuclear applications (e.g. cooling of nuclear reactors, plasma confinement), and metal productions (e.g. solidification of binary alloy, levitation, electromagnetic control of casting) among others.

Although MHD can be found in a wide variety of fields, the physical principles are the same. It is worth to state briefly here the nature of MHD coupling in liquid, which can be split, although somewhat artificially, into three parts [15]:

1. Induction: the relative movement between a conducting fluid and a magnetic field develops electrical currents in accordance with Faraday's law of induction.
2. Induced magnetic field: these induced currents must, according to Ampère's law, give rise to a second, induced magnetic field. This adds to the original magnetic field and the change is usually such that the fluid "drags" the magnetic field lines along with it.
3. Lorentz force: the combined magnetic field interacts with the induced current density to give rise to a Lorentz force, which is generally directed as to inhibit the relative movement of the magnetic field and the fluid.

To be more specific, the magnetic field has two mechanisms of propagation in a media, i.e. diffusion and advection. A key parameter, the magnetic Reynolds number Re_m, describes the ratio of the magnetic field advection to diffusion. The above effects 2 and 3 contribute to the advection of magnetic field, and they have similar consequences: the relative movement between the fluid and magnetic field tend to be reduced. In astrophysical and geophysical applications, the effects of magnetic field advection are generally so strong, i.e. $Re_m \gg 1$, that the magnetic field is altered both inside and outside the media by the relative motion. While in liquid metal applications, where $Re_m \ll 1$, the induced magnetic field is small and ignored. The magnetic field in this case can be considered resulting only from magnet source and not involving in time (more details in section 2.2.2).

Another aspect of the effect 3 above is the counter-force experienced by the magnetic field lines, e.g. those of the permanent magnet. According to Newton's 3rd law, this re-action force on the magnet equals to the volumetric integral of the Lorentz forces experienced by the liquid. One technique based on this principle is the termed "Lorentz force velocimetry" (LFV) [123, 124]. The focus of present work is to expedite LFV to liquid metal two-phase flow applications. The physical model of MHD and a detailed background of liquid metal two-phase flow will follow next.

2.2 Physical model and approximations

The physical model of MHD is a combination of Navier-Stokes equations and a reduced form of Maxwell's equations. We restrict the discussion to incompressible, viscous, electrically conducting (but not magnetic or dielectric) fluids.

2.2.1 Governing equations

Generally we consider liquid metal as incompressible and therefore we have the mass conservation as

$$\nabla \cdot \boldsymbol{u} = 0. \tag{2.1}$$

where $\boldsymbol{u}$ represents the velocity of the liquid. And the Navier-Stokes equations describe the conservation of momentum:

$$\rho \frac{\partial \boldsymbol{u}}{\partial t} + \rho(\boldsymbol{u} \cdot \nabla)\boldsymbol{u} = -\nabla p + \mu \nabla^2 \boldsymbol{u} + \rho \boldsymbol{f}, \tag{2.2}$$

where p is the pressure, ρ the density, μ the dynamic viscosity and $\boldsymbol{f}$ represents the body acceleration forces, e.g. gravity, electrostatic force and Lorentz force. Other effects like temperature, energy are not considered in the present work. Lorentz force is of interest as the body force in liquid metal, which is derived from the simplified Maxwell's equations. In liquid metal MHD applications, the classical Maxwell's equations are simplified based on the following assumptions [15]:

- no free charge within the liquid domain,
- no displacement current within the liquid domain,
- any speeds are finite comparing to the speed of magnetic diffusion.

Thus the simplified Maxwell's equations can be written as (per unit volume) [15]:

$$\begin{aligned}
\nabla \times \boldsymbol{E} &= -\frac{\partial \boldsymbol{B}}{\partial t} && \text{(Faraday's law)} && (2.3)\\
\nabla \cdot \boldsymbol{B} &= 0 && \text{(Solenoidal nature of } B\text{)} && (2.4)\\
\nabla \times \boldsymbol{B} &= \mu_0 \boldsymbol{j} && \text{(Ampère-Maxwell equation)} && (2.5)\\
\nabla \cdot \boldsymbol{j} &= 0 && \text{(charge conservation)} && (2.6)\\
\boldsymbol{j} &= \sigma(\boldsymbol{E} + \boldsymbol{u} \times \boldsymbol{B}) && \text{(Ohm's law)} && (2.7)\\
\boldsymbol{f} &= \boldsymbol{j} \times \boldsymbol{B} && \text{(Lorentz force)} && (2.8)
\end{aligned}$$

where $\boldsymbol{E}$ is the electric field, $\boldsymbol{B}$ the magnetic field, $\boldsymbol{j}$ the electrical current density, μ_0 the magnetic permeability of vacuum and σ the electrical conductivity of the liquid. Finally, from equations (2.3 to 2.8) one may read the scaling of reaction force $\boldsymbol{F_L}$ on the permanent magnet:

$$F_L = -\int_V \boldsymbol{f} \mathrm{d}V \sim (k) \cdot \sigma u B^2 L^3, \tag{2.9}$$

where L represents the length-scale of the flow. Since there does not exist analytical expressions to calculate F_L directly (except some fictitious cases), it is essential to reveal the calibration fraction k for each geometry. The scaling of Lorentz force will be discussed again in section 2.3.3.

2.2.2 The quasi-static approximation

If we combine the equations (2.3, 2.5, 2.7), we obtain the temporal evolution of $\boldsymbol{B}$:

$$\frac{\partial \boldsymbol{B}}{\partial t} = \nabla \times \left(\boldsymbol{u} \times \boldsymbol{B} - \frac{1}{\mu_0 \sigma} \nabla \times \boldsymbol{B} \right) = \nabla \times (\boldsymbol{u} \times \boldsymbol{B}) + \frac{1}{\mu_0 \sigma} \nabla^2 \boldsymbol{B}, \tag{2.10}$$

which is the so-called induction equation or advection-diffusion equation for $\boldsymbol{B}$. As mentioned earlier in section 2.1, we see in equation (2.10) the term $\nabla \times (\boldsymbol{u} \times \boldsymbol{B})$ as the advection and the term $\nabla^2 \boldsymbol{B}$ as the diffusion of magnetic flux. Additionally, considering the coefficient $\frac{1}{\mu_0 \sigma}$ in equation (2.10), velocity scale u and the characteristic length L, we may introduce the definition of one of the most important dimensionless parameters - magnetic Reynolds number:

$$Re_m = \mu_0 \sigma u L \sim \frac{\text{magnetic advection}}{\text{magnetic diffusion}}. \tag{2.11}$$

In most MHD laboratory experiments and industry processes,we have $Re_m \sim 10^{-4} - 10^{-1} \ll 1$ [15]. According to equation (2.10), when $Re_m \ll 1$, the magnetic induction is dominated by diffusion, and the advection term of the magnetic field is small and negligible. This is commonly known as the low-Re_m or quasi-static approximation in liquid metal MHD. Thus we obtain a simplified model which ignores the induced magnetic field $\boldsymbol{b}$, i.e.:

$$\boldsymbol{B} = \boldsymbol{B}_0 + \boldsymbol{b} \approx \boldsymbol{B}_0, \tag{2.12}$$

where $\boldsymbol{B}_0$ is the static magnetic flux generate by the magnet source. By this simplification, equation (2.3) simplifies to $\nabla \times \boldsymbol{E} = 0$, which means the electric field $\boldsymbol{E}$ is curl-free and can be expressed as the gradient of a scalar potential ϕ as $\boldsymbol{E} = -\nabla \phi$. Thus equation (2.7) becomes

$$\boldsymbol{j} = \sigma(-\nabla \phi + \boldsymbol{u} \times \boldsymbol{B}_0), \tag{2.13}$$

and Lorentz force, as the body force in Navier-Stokes (equations 2.2 and 2.8), becomes

$$\boldsymbol{f} = \boldsymbol{j} \times \boldsymbol{B}_0. \tag{2.14}$$

Then, combining the charge conservations (equation 2.6) and equation (2.13), the scalar potential ϕ can be solved by the Poisson's equation with suitable boundary conditions:

$$\nabla^2 \phi = \nabla \cdot (\boldsymbol{u} \times \boldsymbol{B}_0). \tag{2.15}$$

Equation (2.15) is the core of the so-called "electric potential method" under quasi-static approximation, which is widely used in liquid metal MHD.

2.2.3 The kinematic approximation

The kinematic approximation means that the terms of Lorentz force are removed from the liquid momentum equation (2.2). This is acceptable when

$$N = \frac{\sigma B^2 L}{\rho u} \sim \frac{\text{Lorentz force}}{\text{inertia}} \ll 1, \tag{2.16}$$

where N is the interaction parameter. In this approach, the velocity field $\boldsymbol{u}$ satisfy the pure hydrodynamic system and thus, equation (2.15) can be further simplified as

$$\nabla^2 \phi = \nabla \cdot (\boldsymbol{u}_{\text{hydro}} \times \boldsymbol{B}_0), \tag{2.17}$$

where $\boldsymbol{u}_{\text{hydro}}$ denotes the corresponding velocity field in pure hydrodynamic system.

Although the kinematic approximation neglects the effects of Lorentz force on the liquid motion, it has the advantages of being easy to implement and fast to iterate, which suits well as an tool for early-stage design and qualitative estimation of the phenomena.

2.3 State of the art

2.3.1 Liquid metal two-phase flows

Liquid metal two-phase flows are important in numerous technological processes. In the nuclear fusion process, the fast reactor needs to be cooled with liquid sodium. In metallurgical industries, liquid metal two-phase flows occur during the de-oxidation of copper as well as the melt refining in steel-making. Concerning the products of Light-Emitting Diode, liquid metal with boiling is also applied as coolant. Although many studies involving air-water two-phase flow phenomena started early (see e.g. Mallock [69], Minnaert [73], Van Krevelen and Hoftijzer [133], and Wijngaarden [143]), the investigations concerning liquid metal two-phase flows just became apparent in the 1960s [45, 59]. The sub-topics related to two-phase flow are:

- MHD flow with interfaces (e.g. selective melting and casting, stirring, levitation, liquid metal batteries)
- MHD gas-liquid two-phase flow in a duct
- Bubbles/particles behavior and their mixing/stirring in liquid metal

Here, we touch upon just two of them, namely liquid metal two-phase flow in a duct and bubble or particle motion in liquid metals.

Two-phase flow in a duct of liquid metals

One topic for the pioneer scientists in MHD were liquid metal two-phase flows in duct driven by external pumps, which was mainly motivated by nuclear and fusion applications. In such flows, gas bubbles are added to the liquid metal for various purposes: to modify the pressure drop, the turbulent fluctuations, the properties of heat transfer and so on [152]. Thome [125] conducted the first experiments of liquid metal two-phase flow and observed that the magnetic field tended to increase the slip ratio and make the gas distribution more uniform in the field direction, because the large difference in conductivity between the two phases led to greater electromagnetic forces on the liquid. He also provided a simplified model to predict pressure drop of MHD duct flow under the influence of magnetic field. This topic was followed by many researchers. For instance, Neal and Bankoff [80] investigated nitrogen-mercury flow via the local pressure measurement. Owen et al. [83] improved the prediction of pressure drop for large Hartmann numbers. M. Saito et al. [99] conducted similar experiments and reported that the MHD pressure drop of the two-phase flow became a little higher than that of single phase liquid flow. Similar conclusion came from Dunn [22] as well. These data were later in good correlation by the model of Dobran [18]. The detailed measurements of heat transfer and the local properties of bubble were achieved as well. Michiyoshi et al. [71] used customized electrical resistivity probe (originated from Serizawa et al. [111]) to reveal the distribution data of local void fraction, bubble impact rate, bubble velocity, bubble length and their spectrum. Fabris et al. [30] conducted similar measurements firstly with the hot-film and resistivity probes. Such measurement with a broader parameter space was then explored by Gherson and Lykoudis [35]. Up to now scientists are still progressing on such experiments [27, 47, 58, 110, 118, 122]. A comprehensive review and outlook can be found in Morley et al. [79]. However, to my knowledge, there seems lack of studies in this direction in the recent fifteen years, perhaps because nuclear energy and fusion are considered as "environmentally-unfriendly" in many countries and the corresponding research has been therefore sidelined.

Bubble or particle motion in liquid metals

On the other hand, bubbles or particles swirling around in liquid is a popular topic. We refer to S. Eckert et al. [27], Fröhlich et al. [32], C. Zhang [152], and J. Zhang and Ni [154] as good reviews for bubbles rising in liquid metal. Scientists studied the flows generated by bubbles rising in liquid metals, perhaps inspired by the air-water experiments (e.g. Degaleesan et al. [16], Hartunian and Sears [39], Krevelen and Hoftijzer [54], Leibson et al. [57], and Saffman

[98]). Following the pioneer experiments (see e.g. Andreini et al. [6], Y. Mori et al. [78], and Sano and K. Mori [102]), Irons and Guthrie [48] summarized the scaling of bubble diameters in low and high temperature alloys. A more detailed measurement can be found in Iguchi et al. [46]. Later on, many researchers tested the feasibility of new measurement techniques in liquid metal bubbly flow applications [76], which turned out to be very successful and led to fruitful findings, of which we will give a short summary later. Numerical simulations achieved good agreement with experiment, and they play a significant role as it can reveal much more details of the flow (see e.g. Schwarz and Fröhlich [109], Shin and Kang [112], Tran et al. [127], Tschisgale et al. [129], J. Zhang and Ni [153], and J. Zhang et al. [155]). Additionally, not only the characteristics of single bubbles but also bubble chains and its distributions are interesting for researchers (see e.g. Heitkam et al. [42], Keplinger et al. [51], Krishnapisharody and Irons [55], Krull et al. [56], Rakoczy and Masiuk [93], and C. Zhang et al. [151]). Based on the knowledge of bubbles motion in liquid metal, attentions were also paid to metallurgical processes such as the gas-jet behavior in casting [77] and gas-stirred bath [103]. The topic of steel-casting with gas-jet is attracting eyes as well (e.g. Arcos-Gutierrez et al. [8], Bai and Thomas [9], and Pfeiler et al. [87]).

2.3.2 Measurement techniques for liquid metal flows

From the history of MHD research, it is obvious that the measurement technology serves as significant assistance to the liquid metal MHD investigations. We refer to Ratajczak et al. [94] as excellent review. The measurement techniques for local MHD flow structures and selected publications are summarized as follows:

- Electric potential probe [11, 52, 75, 88] or Vives probe [97]. It is based on measuring the local electrical potential of a flow under static magnetic field. The probe is submerged into the flow and a good electrical contact with the liquid is required. The drawback is that the obtained electrical potential cannot reflect well the liquid velocity in the very-near wall region (Hartmann boundary layer) due to the significant currents there.

- Electrical resistivity probe [26, 30, 71] is generally applied for the problem of void fraction. It is based on the electrical contact between the probe and the liquid. The resistivity of the probe may drop significantly if a conducting liquid flows through it and vice versa if it meets the gas phase. Again, the contact between the probe and liquid is always an issue.

- Hot-film anemometry [31, 35, 116] is another classical approach. It depends on the scaling of the resistivity of probe as well, except that the probe in this case is heated to some temperature above the ambient, and its resistivity changes due to the cooling effect of the flow.

- Sensitive pressure probe / pitot tube [80, 148] is an intrusive method based on the pressure transducers.
- Optic-mechanical method [25, 29] is an innovative method for opaque liquid. It is based on the displacement of the tiny mechanical components submerged into the flow.
- Ultrasonic techniques and its sub-types are widely used in liquid metal MHD:
  - Ultrasonic Doppler Velocimetry (UDV) [1, 20, 24, 115, 117, 135, 150] and UDV with waveguides for applications at higher temperature [28]. Its application in fluid dynamics relies on the pulsed Doppler method, where an emitter sends periodically a short ultrasonic burst and a receiver collects continuously echoes issues from targets that may be present in the path of the ultrasonic beam. By sampling the incoming echoes at the same time relative to the emission of the bursts, the velocity of the particles can be computed.
  - Ultrasound Transit-Time Technique (UTTT) [7, 96] is an innovative technique for bubble applications. It is used to determine the size and velocity of gas bubbles in liquid metals. This is achieved by measuring the ultrasound transit time between the ultrasound sender/receiver and the reflecting bubbles.
- Imaging by high energy radiation, namely γ ray [99, 125], X ray [13, 14, 46, 74, 126] and neutron [100, 104, 105, 119]. The measurement relies on the attenuation of the ray. If we have tracers, or density changes in the melt, the flow can be actually visualized. Therefore it is very good for the applications of two-phase flow and solidification. The measurement data are generally 2D, and can be extended to 3D under careful experimental configuration or data-processing. However due to the high density of liquid metals, the attenuation of the rays is very high so that the thickness of liquid metal domain is limited, typically in the range of $1 - 10$ cm.
- Inductive method for local flow structure is another broad topic:
  - Electromagnetic (resistivity/conductivity/capacitance) tomography [5, 23, 36, 67, 86, 144, 146], other methods by inductive coils [37, 38, 122], and contactless electromagnetic phase-shift flowmeter [89]. These methods relies on the temporal revolution of magnetic field ($\partial \boldsymbol{B}/\partial t$). By these techniques a time-alternating magnetic filed is applied to the liquid domain, and the reacting-alternating induced magnetic field is recorded by electronics nearby. The information of the flow is then reconstructed by the difference between the applied magnetic field and the induced one.
  - Contactless inductive flow tomography (CIFT) [95, 114, 145] applies globally a static magnetic field to the flow. The velocity is reconstructed from the advection term of the magnetic field induced by the flow ($\boldsymbol{u} \times \boldsymbol{B}$).

  - Lorentz force velocimetry (LFV) [41, 44, 61], as a innovative subtype of the inductive method, applies static magnetic field to the flow as well. However we measure the reaction force on the source of the magnetic field, which is equivalent to Lorentz force within the liquid due to Newton's 3rd law.

Among the above techniques, as also mentioned in section 1.1, by the contacting techniques the sensor must be submerged into the liquid or embedded in the wall, therefore the wetting or electric contact between the probe and liquid is alway crucial. On the other hand, LFV has the advantage of non-intrusive as well as easy-to-integration, since the magnet source (e.g. a permanent magnet) and sensing part (e.g. a commercial force sensor) are combined in one body at low cost. As will be discussed soon in section 2.3.3, LFV has the potential to resolve the measurement problem for complex flows even under harsh environment like high temperature, vibration or under ambient electromagnetic noise, which makes it appealing for industry applications like metallurgy. Therefore in the present work we focus on the feasibility study of LFV for complex liquid metal flows. There exist already plentiful investigations of LFV for liquid metal MHD. An overview of its state-of-art and applications will follow.

2.3.3 LFV in MHD applications

As also mentioned in section 1.1, Lorentz force velocimetry is a non-contact technique for velocity measurement in electrically conducting fluids. It is based on exposing the flow to a magnetic field and measuring the force acting upon the magnetic sources [123]. In liquid metal applications, LFV can be constructed in two different ways, i.e. the static flowmeters where the magnet system is at rest and one measures the force acting on it, or the rotary flowmeters where the magnets are arranged on a rotating wheel and the spinning velocity is a measure of the flow velocity [124]. The rotary LFV is beyond the topic of present work.

As described in the physical model (section 2.2.1), the proportionality of LFV to flow velocity is the core of this technique, namely

$$F_L \sim (k) \cdot \sigma u B^2. \tag{2.18}$$

The previous studies of LFV may be categorized based on the above key parameters:

- Regarding electrical conductivity σ:
  - electrolytes $\sim 10^{-6} - 10^{2}$ S/m were successfully measured by LFV [2, 17, 134, 136, 141]. The weight of magnet system was ~ 1 kg, and the forces were $10^{-8} \sim 10^{-6}$ N.
  - liquid metals $\sim 10^{3} - 10^{6}$ S/m such as liquid GaInSn, liquid aluminium and liquid steel [40, 53, 137]. The forces were in the range of $10^{-3} - 1$ N.
  - solid bodies $> 10^{6}$ S/m. The knowledge of nondestructive testing via Lorentz force

  eddy current testing (LET) [12, 131, 149] and its simulation and inverse problem to remap the defects [19, 84, 85, 108, 139] were significantly developed.
  - The inverse problem to determine liquid conductivity (i.e. liquid tin) based on force measurement was tested and proved [4].

- Regarding velocity $\boldsymbol{u}$, different geometries were tested such as duct flow [10, 40, 137], open channel flow [49, 53], flow carried by rotating channels [49, 113], flow in a continues casting model [43], flow generated by magnetic obstacle [90, 101]. The time-of-flight force measurement [21] achieved the flowrate by tracking the perturbations on Lorentz force from flow vortices using two LFVs. Additionally the results of electrolytes and liquid metals show that the different velocity profiles under the same flow rate have barely influence on Lorentz force flowrate measurement [123, 142]. Therefore one should consider a smaller permanent magnet for localized measurement.

- Regarding calibration fraction k, the dry test helps to determine it before MHD runs. The studies show agreement of k between simulation, dry calibration and MHD test [72]. When magnetic Reynolds number $Re_m > 4$, the nonlinearity of k with respect to flow velocity was observed [10, 113].

- Regarding magnetic field $\boldsymbol{B}$, the studies show that $\boldsymbol{B}$ has a significant influences on the Lorentz force [124]. Various investigations were done considering a large Halbach array of permanent magnets [17, 137], a small magnet [40, 43] and (numerically) a magnetic dipole [130], respectively. Experimental test using high-temperature superconductors as magnet source for LFV is ongoing as well [132, 138].

- Regarding force measurements:
  - commercial load cells for static force [21, 49] and piezo-electric sensors for dynamic force measurement [113] were carried out. The Lorentz force signals were explored in the range of $10^{-3} - 10$ N as well as frequency band of ~ 100 Hz.
  - The innovative multicomponent force and torque measurement system [43, 70, 92, 106] is able to measure all the 6-components of forces and torques on the permanent magnet, which provides much more information of the flow and vortices.
  - Electromagnetic force compensation system [134] is customized from precision weighting-scale, which is capable of resolution 10^{-8} N with high dead-load of about ~ 10 N. It helps LFV to explore the flow with extremely low conductivity of about $\sim 10^{-6}$ S/m.
  - One ongoing study targets at reaching resolution $\sim 10^{-9}$ N by a torsion balance-based system with closed-loop operational mode [147].
  - The customized Interferometric optical force sensor (IOFS) [34] is of resolution down to 10^{-6} N making precise measurement for local flow structure of liquid metal achievable. It has dynamic capability up to ~ 10 Hz.

There exists however few studies concerning LFV for two-phase flows. Therefore the present work focus on the feasibility test of LFV in liquid metal two-phase flow applications.

2.4 Principle of LFV in liquid metal two-phase flow applications

One can see that there exists various degrees of freedom when we configure LFV experiments. Therefore it is worth to firstly summarize the parameter ranges of LFV concerning different applications in figure 2.1. We may refer to the physical model (in section 2.2.1) and review of previous studies (in section 2.3.3) in the following.

- Lorentz force for electrolyte is generally in the range of $10^{-8} - 10^{-6}$ N, and therefore it is essential to provide high-precision-sensor and large magnetic field. A long responding time of LFV in such cases, usually in the range of $1 - 100$ s, cannot be avoided [134].
- In the applications of liquid metal flow-metering, the resolution of $10^{-3} - 1$ N is enough to reveal the flow rate, because generally the length-scale of the flow L is large [124].
- In the previous study of solid body defect-testing via Lorentz force technique, in order to produce significant target force-signals, the solid body with defects was adjusted at constant high velocity (~ 0.5 m/s) and the distance between LFV and solid body was set to $1 - 2$ mm. Therefore the results from a commercial force sensor of resolution $\sim 10^{-3}$ N under such configuration is sufficient [12].
- However when one considers LFV for liquid metal flows around bubbles or particles, which is the motivation of the present work:
  - The force resolution is more crucial compared to liquid metal flow-metering, since the length-scale of liquid metal flows around bubbles or particles is generally smaller than that of a pipe flow.
  - The force resolution is more demanding compared to solid body defects testing, since the velocity is lower and the distance between LFV and moving media cannot be such small.
  - The demand of LFV for responding time is also more crucial compared to the flow of electrolyte, because the liquid metal flows around bubbles or particles are sometimes unstable and dynamic.

One must therefore push LFV more to the physical limit of measurement technique, which is alway a trade-off between resolution and fast-response. Based on the previous studies, it is reasonable to predict that the practical region of LFV for liquid metal two-phase flow applications is the resolution of $10^{-6} - 10^{-4}$ N and the responding frequency of $1 - 10$ Hz as shown in figure 2.1. The above considerations make IOFS the best sensor for the present work, which is precise and fast-responding at the same time.

Designing the magnet system is another concern. A schematic of the three general scenarios of magnetic fields in LFV is shown in figure 2.2, namely (a) the (almost) homogeneous magnetic field or a localized magnetic field by (b) a magnetic dipole or (c) a small cubic magnet. Although the magnetic fields of (b) and (c) are almost identical from a distance, (b) is easier for analytical and numerical implementations. In the present work we chose scenario (c) of small permanent magnet, because:

- When a small permanent magnet is brought to the vicinity of the liquid, it has the capability to reconstruct even complex flow fields near the wall [41].
- When the magnet is smaller, the dynamic response of measurement system is faster, which helps to capture more instantaneous information comparing to such using a heavy system.
- The global magnetic field is robust in the case of flow rate measurement however not sensitive to velocity profiles [123, 142]. This effect limits its application in liquid metal two-phase flows, where revealing the details of flow structure is of interest.
- The case of magnetic dipole is interesting for theoretical or numerical considerations but cannot be validated by experiments. Therefore magnetic dipole is not considered in the present work.

2.5 Principle of the Interferometric-Optic-Force-Sensor

The customized Interferometric-Optic-Force-Sensor (IOFS) is used in the present work, which is derived from a joint work of our colleagues in "Institute of Process Measurement and Sensor Technology" (TU Ilmenau) and engineers in "SIOS Meßtechnik GmbH" (Ilmenau).

The principle of IOFS is shown in figure 2.3 (courtesy by I. Rahneberg). The base body is made of quartz glass, which has excellent mechanical properties like a low delayed elasticity, and low thermal expansion [92]. The couple 2 is fixed. When there is reaction force on the permanent magnet attached to the couple 1, the deflection occurs on the leaf springs as well as the deflecting prisms, which is represented by the displacement between the deflecting prisms and the reference triple prism. Such displacement is recorded by the interferometric sensor with coupled fiber. The resolution of deformation is within 0.1 nm. The maximum load should be < 0.15 N and an overload protection is included in the sensor. The static calibration factor k_0 of the sensor in unit of [N/m] is gained by the precise weight measurements. Therefore, the re-action force on magnet can be calculated via the calibration factor and deformation length.

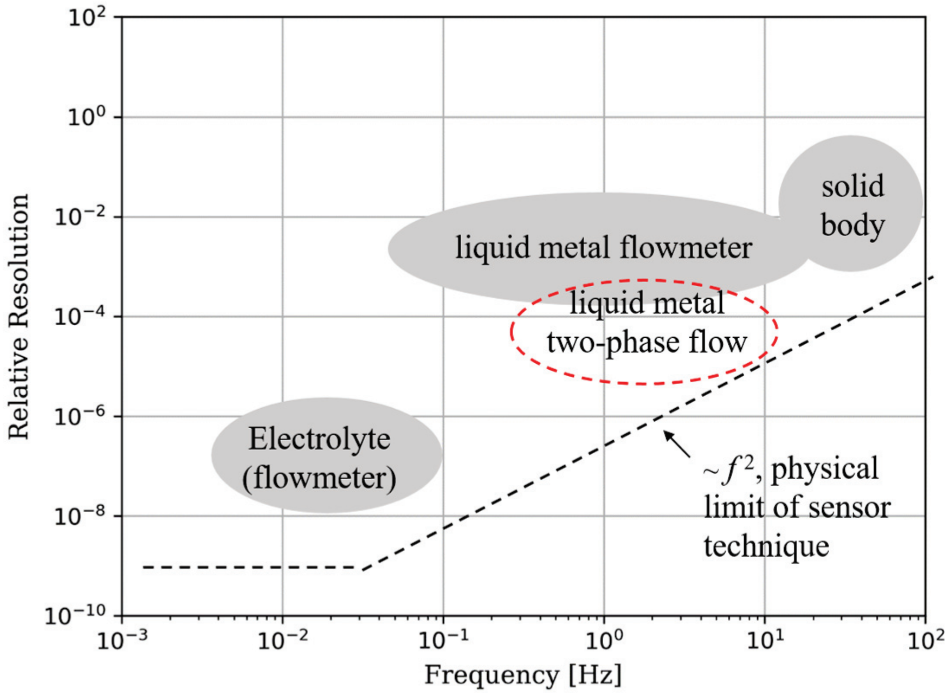

Figure 2.1: Concept of the parameter space of relative force-resolution and responding frequency of LFV. (The relative force-resolution is defined as the ratio of resolution over maximum load.)

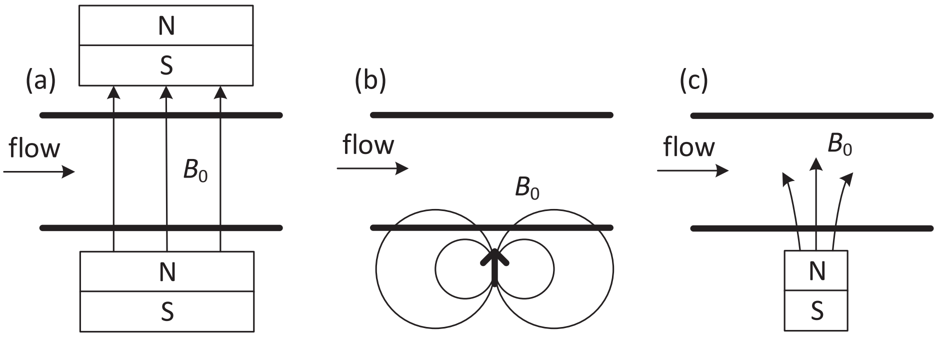

Figure 2.2: Concept of scenarios of magnetic fields in LFV. (a) homogeneous magnetic field (b) magnetic dipole (c) small permanent magnet.

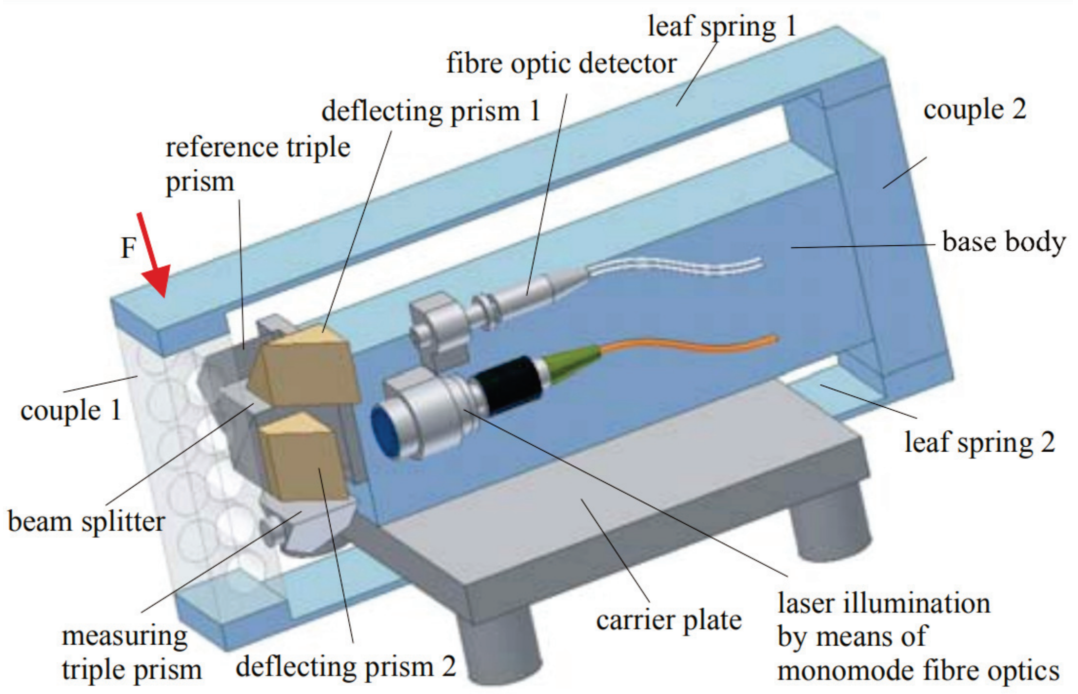

Figure 2.3: Principle of the Interferometric-Optic-Force-Sensor (© I. Rahneberg).

2.5.1 Operation modes

It should be noted that the sensor has very different sampling modes with its embedded data processing units:

- **Continuous mode**, which is the default. It contains the following data processing automatically. After original sampling rate of 8192 Hz, the data is cutting-averaged by each 128 samples. Afterwards a carefully designed low-pass filter is applied to de-noise the signal. Then the output to PC is a continues time-series of the deformation at $6.3 - 6.4$ samples per second.
- **Manual mode**. Another option is calling the device manually via Function Library. The scripts on PC extract samples from IOFS continuously by each calling and the maximum sampling rate depends on the communication bandwidth. The maximum sampling rate in the test by USB cable is $80 - 90$ Hz.
- **Super-fast mode**. We use the so-called "Super-fast mode" if we switch-off the default data processing. In this mode, the data is sampled and stored internally, during which there is no communications with PC. The sampling rates in this mode are min. 781.25 Hz and up to 1MHz. However without continuous communication with PC, the embedded RAM can store limited samples at one time. E.g. using the lowest sampling rate of 781.25 Hz we can have a measurement as long as ~ 60 seconds.

The sampling rate is not only a matter of acquiring data, but also a trade-off for different applications. The default sampling rate of $6.3 - 6.4$ Hz is sufficient for LFV in flow rate measurement, however it is too slow for liquid metal two-phase flow applications. On the other hand, setting a very-fast sampling provides us data with more instantaneous information, but they contain much more noise due to the inertia of sensor mechanics. Knowing the resonant frequency of IOFS is 14-17 Hz, the noise must be treated carefully in this case. The super-fast sampling of > 700 Hz seems too much, however this is the lowest we can use due to the embedded data processing units in the super-fast mode. Nevertheless the high samples rate helps to reduce measurement error. Please refer to section 2.5.2 for details of data processing and section 2.5.3 for error analysis.

2.5.2 Data processing

In the present work, data from the continuous mode are used in the preliminary experiments in sections 3.2 and 4.1, while super-fast sampling is conducted in the extended experiments in sections 3.3 and 4.2. A customized de-noising is coupled with the data from super-fast sampling. With raw data from the super-fast mode, we observe that the signal-to-noise ratio is about $\frac{1\ \mu\text{N}}{500\ \mu\text{N}} = -54$ dB. Therefore a careful data processing is mandatory in such crucial cases. The data processing is performed afterwards in MATLAB.

Dynamic compensation of LFV signals

The static calibration is generally sufficient for static or quasi-static force measurement. In the present work however, when approaching the resonance frequency of the IOFS, which is 14-17 Hz, the measurement deviation caused by using static calibration coefficients increases and must be considered. The behavior of IOFS is very similar to the frequency response of the second order transfer function $G(s)$ [107]:

$$G(s) = \frac{k_0 \omega_0^2}{s^2 + 2\varepsilon\omega_0 s + \omega_0^2},$$

where s is the frequency, $k_0 = 3.0653 \times 10^{-4}$ N/m is the static calibration factor, ε is the damping coefficient and ω_0 is the resonant frequency of the system. Its responses to various known sinusoidal periodic inputs were recorded to identify the coefficient ε and ω_0. The details of the method can be found in Schleichert et al. [107].

In the present work, IOFS is one-directional sensor. Therefore the vertical (z-) and horizontal (x-) directional alignments were tested respectively. The identified parameters of the model $G(s)$ are summarized in table 2.1. It should be noted that the characterization parameters can only be used for the processing of the identical configuration. An individual dynamic test is

Table 2.1: Dynamic characterization of the IOFS force sensor.

distance between	vertical measurement			horizontal measurement		
LFV and liquid	∞	10 mm	5 mm	∞	10 mm	5 mm
ω_0 (Hz)	16.18	16.17	16.17	14.46	14.46	14.44
ε	0.0132	0.0149	0.0176	0.0022	0.0053	0.0122

mandatory for any changes in the setup. We observe that by decreasing the distance between IOFS and liquid metal, the damping coefficient ε increases significantly, because the magnetic flux density increases very fast approaching the magnet. Such influence on the LFV signal is not interesting for static measurement (e.g. for flowrate), however it must be considered in dynamic applications such as liquid metal two-phase flows, because two-phase flow is generally dynamic and involves fast-fluctuating signals and thus, magnetic damping here must play a role in Lorentz force signals.

Knowing the characterization of LFV, the dynamic compensation of Lorentz force signals can be done via $G(s)^{-1}$ to exclude the effects of sensor resonance on the signals. The amplitude-frequency character is illustrated in figure 2.4. The dashed red curve denotes the transfer function $G(s)$ obtained by dynamic test, which is considered to fully represent the sensor dynamics. The inverse of transfer function $G(s)^{-1}$ is then applied to exclude the effects of sensor mechanics on signals. As $G(s)^{-1}$ approaches infinitely high amplitude above 100 Hz, a low-pass filter (dashed blue curve) is applied to suppress such arbitrary noise in the high-frequency regime, which is far beyond the frequency regime of interest ($1-10$ Hz) and should not be concerned. The solid black curve represents the combined effects, by which the signals are tuned. For example at 10 Hz, from the combined effects, the amplitude is suppressed by the factor of 0.55, while at resonant frequency of 16 Hz, the signal should be suppressed by the factor of 0.025. The procedure increases the accuracy of IOFS in dynamic measurements significantly, which is applied to all the following data.

Wavelet filtering

To further de-noise the LFV signal, the wavelet filtering is applied after the dynamic compensation. The de-noising concerns the signal in the frequency domain. The widely-used Fast Fourier Transform (FFT) is a powerful tool to analyze signals in the frequency domain [81]. However it does not work well if the frequencies vary in time [113]. An intuitive solution is to make the window-function for frequency analysis time-dependent, so that the localized information of time and frequency is not lost, from which the idea of wavelet comes [68]. There are many works on the theory and features of wavelet method, and they are therefore not described in the present thesis. In a nutshell, I use the orthogonal 10-tap Daubechies wavelet [68], and the signals are reconstructed down to level 6 by discrete wavelet transform,

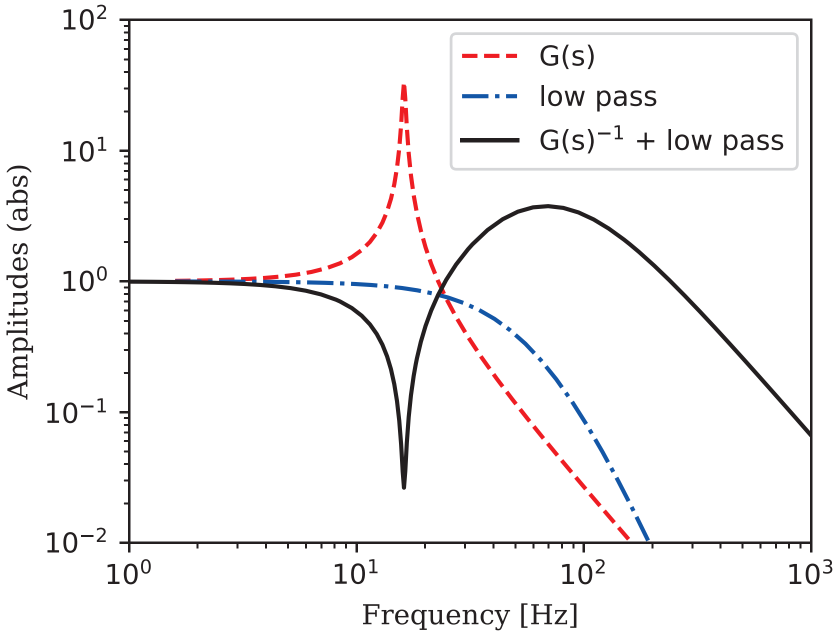

Figure 2.4: Schematic of the transfer function for dynamic compensation of LFV signals.

which meets the best approximation in the present work. The re-constructed signal contains the Lorentz force informations in the frequency range of $0-12$ Hz, which can well represents the raw data for particle and bubble rising in the present work.

The wavelet filter is validated by a known fluctuating force on LFV, which is applied by a coil excited by a square wave. The force on LFV should be of frequency 1 Hz and amplitude 10 μN. The measurement results are shown in figure 2.5. The upper subfigures shows the raw data from super-fast mode and the corresponding FFT. We observe the noise of $\pm$ 500 μN. The subfigures in the middle row shows the results after dynamic compensations, by which the noise is suppressed significantly. In the last row, after wavelet filtering, the square wave is observed, which agrees well with the input. Concerning FFT results in the right column, the raw data contains much noise, especially at the resonant frequency of 16 Hz and above. After dynamic compensation the resonance is suppressed. After the step of wavelet filtering, the noise above 12 Hz is excluded while the information below is kept effectively. This test shows that the wavelet filtering is effective and it will be applied on all signals from fast-mode of IOFS in the following.

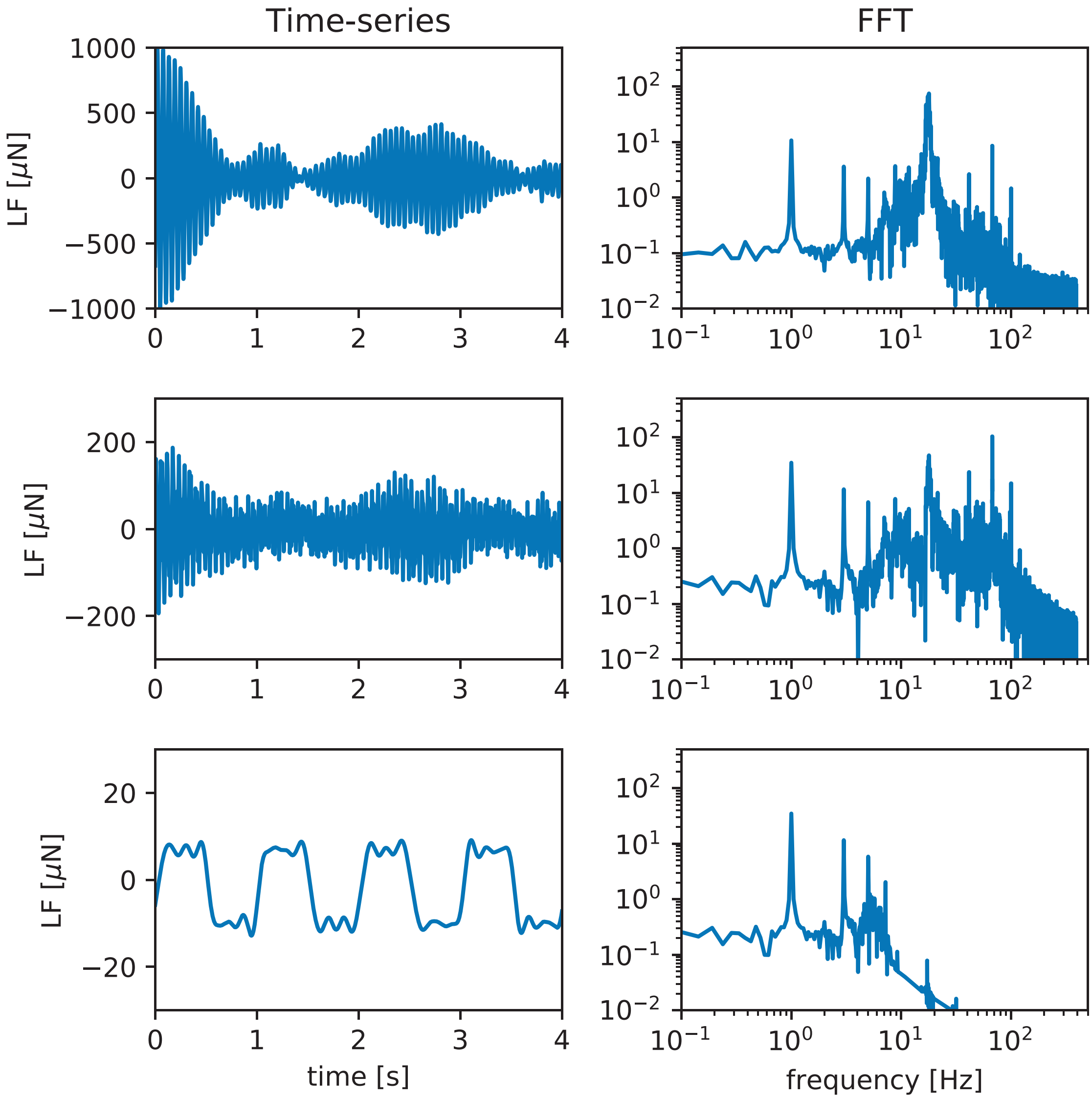

Figure 2.5: Example of data processing for a 1 Hz square wave input.

2.5.3 Error analysis

As Lorentz force F is a function of n variables x_i and each brings the error independently, the total absolute measurements error $Sa(F)$ is [121]:

$$Sa(F) = \sqrt{\sum_{i=1}^{n} (\frac{\partial F}{\partial x_i} S(x_i))^2}. \tag{2.19}$$

The measurements uncertainties consist of random and statistical uncertainties, and thus:

$$Sa(F) = \sqrt{Sa(F_{ran})^2 + Sa(F_{sys})^2} \tag{2.20}$$

The absolute random errors $Sa(F_{ran})$ are statistical fluctuations (in either directions) in the measured data due to the limitations of the measurement device, which usually result from the experimenter's inability to take the same measurement in exactly the same way to get exact the same number. The random errors can be evaluated through statistical analysis and can be reduced by averaging over a large number of repeated observations. The standard deviation of the mean is the general estimation of random error [121]:

$$Sa(F_{ran}) = \sqrt{\frac{1}{N} \sum_{i=1}^{N} (F_i - \overline{F})^2}, \qquad \overline{F} = \frac{1}{N} \sum_{i=1}^{N} F_i \tag{2.21}$$

where F_i represents each sample and N is the number of samples. It means that if the values F_i are normally distributed, one more sample of F_{i+1} will be within the interval $\overline{F} \pm Sa(F_{ran})$ with the probability of 68 % [121]. The equation (2.21) is used in the present work to evaluate the random error. The random error of Lorentz forces were evaluated at zero particle velocity. From equation (2.21) we obtain the absolute error for the superfast-mode (with post-processing):

$$Sa(F_{ran}) = 0.47\ \mu\text{N}. \tag{2.22}$$

On the other hand, the absolute systematic errors $Sa(F_{sys})$ are reproducible inaccuracies that are consistently in the same direction, which are often due to a problem which persists throughout the entire experiment. In the present study the propagation of the absolute systematic error $Sa(F_{sys})$ are coupled with:

$$Sa(F_{sys})^2 = \left|\frac{\partial F}{\partial k_0}\right|^2 Sa(k_0)^2 + \left|\frac{\partial F}{\partial \sigma}\right|^2 Sa(\sigma)^2 + \left|\frac{\partial F}{\partial u_0}\right|^2 Sa(u_0)^2 + \left|\frac{\partial F}{\partial B_0}\right|^2 Sa(B_0)^2, \tag{2.23}$$

where $Sa(k_0)$, $Sa(\sigma)$, $Sa(u_0)$, $Sa(B_0)$ represent the absolute errors of calibration factor, liquid conductivity, particle velocity and magnet flux density. The errors of calibration factor and liquid conductivity result from the room-temperature change in the lab. For example, the temperature change of GaInSn during one day of continuous measurements did not exceed 2 °C, which leads to the relative error $Sr(\sigma) < 0.3\%$. Such errors are so small that they are neglected. The velocity error $S(u_0)$ comes from the linear driver. The error of magnetic flux density $S(B_0)$ comes from the positioning of the magnet and liquid container. Taking the experiment of particle rising in section 3.3 as example, the errors of the peak values in the cases of Reynolds number $Re = 200,\ 2000$ should cover the regimes of errors in the present work.

Table 2.2: Errors of drag-force measurement.

Re	$F_{z,max}$	u_0	B_0	$Sr(F_{ran})$ [1]	$Sr(F_{sys})$ [2]	$Sr(F)$ [3]
200	$4.5 \pm 0.5\ \mu$N	12.3 ± 2.0 mm/s	21.5 ± 1.25 mT	10.44%	17.24%	20.16%
2000	$17.1 \pm 0.5\ \mu$N	123.2 ± 2.0 mm/s	21.5 ± 1.25 mT	2.75%	6.04%	6.63%

Temporal resolution

Under the slow-mode of IOFS, the sampling rate of 6.3 Hz provides us the temporal resolution of ±0.08 s for Lorentz force. In the super-fast mode, the sampling rate of 781.25 Hz provides us higher temporal resolution, however the inertia of IOFS must be considered. Based on the resonance of the sensor, the static calibration factor k_0 is invalid above 6 Hz, however with a proper dynamic compensation (described in section 2.5.2) we may push the limit of response up to 12 Hz. Ever faster response is possible however it introduces too much error, which is therefore not considered. The trustworthy response of 12 Hz provides us the temporal resolution of ±0.04 s for Lorentz force. As will be shown later in section 3.3, the synchronized UDV system is of sampling rate > 50 Hz, which is much higher comparing to LFV. Another aspect is the delay of the synchronization procedure, which is in the scale of $\sim 10^{-3}$ s, which can be neglected. Above all, the total temporal resolution of LFV experiment is considered as ±0.04 s in the present work.

---

[1] $Sr(F_{ran}) = Sa(F_{ran})/F_{z,max}$ is the relative random error, where $Sa(F_{ran})$ is from equation (2.22).

[2] $Sr(F_{sys})$ is the relative systematic error, where only the components of $Sa(u_0)$, $Sa(B_0)$ in equation (2.23) are considered.

[3] $Sr(F)$ is the total relative error according to equation (2.20).

Chapter 3

Particle motion in liquid metal

In this chapter we focus on the topic of particle rising in liquid metal initially at rest. A first test of particle free-rising in a thin tube is defined in section 3.1, and later the corresponding experiment is described in section 3.2). The constant rising velocity of particle in the setup does not allow us to explore stable flow regimes at low *Re*. It motivates us to perform the extended experiment (section 3.3), where the particle route and velocity are controlled and can be varied in $10 - 200$ mm/s ($Re = 160 - 3260$). The results are promising and the peaks of Lorentz force show the effects of various quantities on Lorentz forces. There is encouraging agreement to numerical models as well, which is described in section 3.4. The hydrodynamic instability (especially at high *Re*) however limits the observed scaling laws to the applications of particle detection. In section 3.5, based on the obtained LFV data, an interesting test of particle-position prediction using neural network is described. This method is proven to be successful and robust to predict particle positions, which relies solely on LFV results. It opens the gate to treating engineering LFV results by machine learning algorithms.

Part of the results in this chapter have appeared in publications Karcher et al. [50], Lyu et al. [60], Lyu and Karcher [61], Lyu et al. [63], and Tran et al. [128].

3.1 Problem definition

The geometry is shown in figure 3.1, which applies in both experiment and simulation. The fluid is characterized by its electrical conductivity σ, density ρ, and kinematic viscosity ν [40]. Unless specified otherwise, the fluid property is taken from the alloy GaInSn, and the magnetic field is characterized by the magnetic flux B_x at the center of the particle from a 12 mm cubic NdFeB-based permanent magnet, when it is at the same height as LFV. The length- and velocity scales of the flow are characterized by the diameter d and velocity u_0 of the particle, respectively. The LFV is installed near the liquid domain and receives the reaction force on the permanent magnet due to the particle-induced fluid motion. The object of investigation is a particle moving vertically in liquid metal initially at rest. The results are the individual reaction forces on the permanent magnet in x- and z- directions excluding the

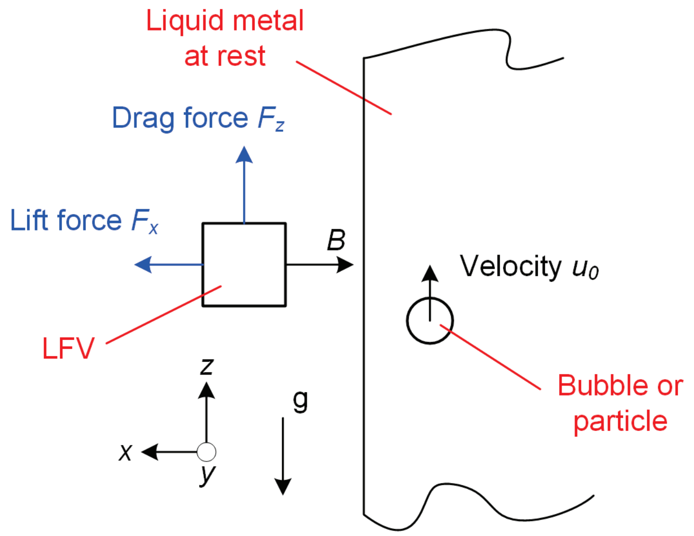

Figure 3.1: Schematic of the problem definition (view on the x-z plane).

weight of the magnet, namely drag and lift forces. As described in section 2.2, the secondary magnetic field $\boldsymbol{b}$ is neglected in the present work. In numerical models, by kinematic and MHD approaches, the Lorentz force braking-effects on the flow are switched off and on manually. The effects of the left wall is the main concern. Unless stated alternatively, the effects of the top- and bottom boundaries and other side walls are neglected.

3.2 Experiment of "free rising" particle in a thin tube

As a first test, a spherical plastic particle rises in a thin tube filled with GaInSn. A fishing line is installed in the tube to prohibit the lateral motion of the particle. The particle rises with uncontrolled velocity but maintains a straight vertical route following the line.

3.2.1 Experimental setup

The photo and schematic of the experimental setup for a sphere rising in liquid GaInSn in a thin tube are shown in figures 3.2 and 3.3. It consists of a cylindrical glass, particle positioning system, LFV and its data acquisition unit. As described in [61], the test section is a glass tube of inner diameter 20 mm, wall thickness 3 mm and length 250 mm. The tube is filled with alloy GaInSn as working fluid. A fishing line is held straight through the tube by springs. The line runs through the central hole of the particle of 6 mm diameter and thus, the particle rising path is restricted by the fixed fishing line. The particle is made of plastic and not conducting, and the effects of magnetic permeability is neglected because the relative magnetic permeability of plastic is finite ($\mu_r \sim 1$), where μ_r represents the relative permeability of plastic. The particle rises freely due to buoyancy. A cubic permanent magnet (NdFeB 48 material) of 12 mm side-length is attached to the LFV sensor. The magnetization points directly into the tube. Its magnetic flux density is measured by a Gauss Meter and shown in figure 3.15. LFV consists of the Interferomatric-Optic-Force-Sensor (IOFS) [34] and the magnet attached to it. The sensor detects the vertical component of the flow-induced Lorentz forces. Its resolution is 1 μN with cut-off frequency 6.3 Hz. Details of the sensor was described in section 2.5. Upward forces are set to be positive in this study. Without the sphere motion, LFV detects only the weight of the permanent magnet. When the sphere rises through the near-magnet region, some local liquid flow and eddy currents occur due to the displacement effect of the sphere, and Lorentz forces are generated. Hence, using this setup, a difference measurement of the Lorentz forces can be made.

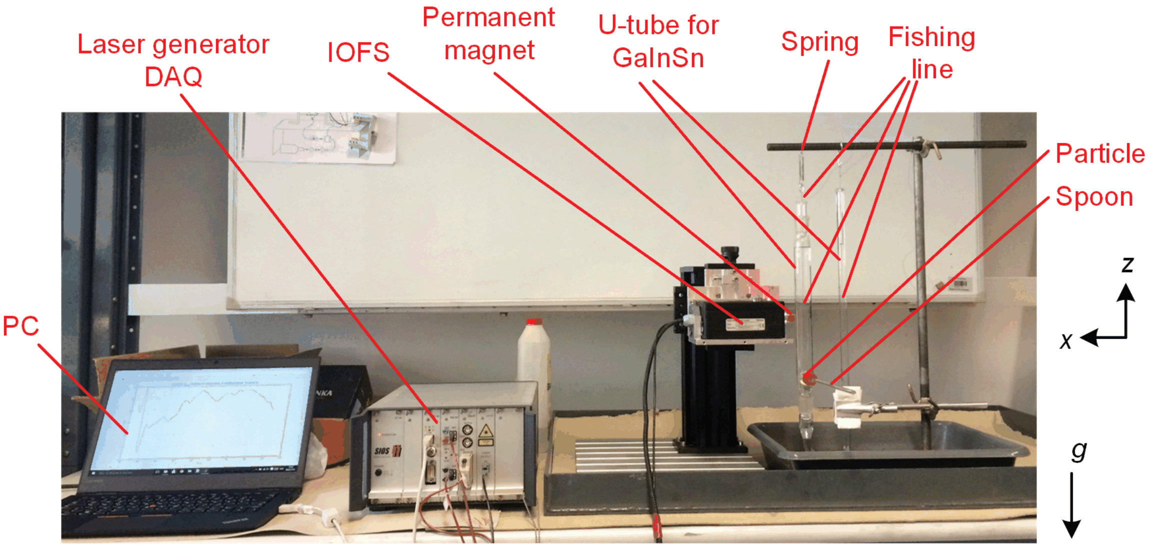

Figure 3.2: Photo of the experimental setup for particle rising in a thin tube.

Regarding dimensionless parameters we assume that the averaged particle velocity is similar to that in [32, 150], which lead us to $u_0 = 0.22$ m/s. The Reynolds number Re is then estimated as follow

$$Re = \frac{u_0 d \rho}{\mu} = 3570.6, \tag{3.1}$$

where $u_0 = 0.22$ m/s is the mean velocity of the particle, $d = 6$ mm is the diameter of the particle, $\rho = 6.492$ g/cm^3 is the density of GaInSn, and $\mu = 0.0024$ Pa $\cdot$ s is the dynamic viscosity of GaInSn, respectively. For the Hartmann number Ha we obtain

$$Ha = B_0 d \sqrt{\frac{\sigma}{\mu}} = 10.7, \tag{3.2}$$

where $B_0 = 47$ mT is the magnetic flux density $\boldsymbol{B_x}$ at the center of particle, and $\sigma =$

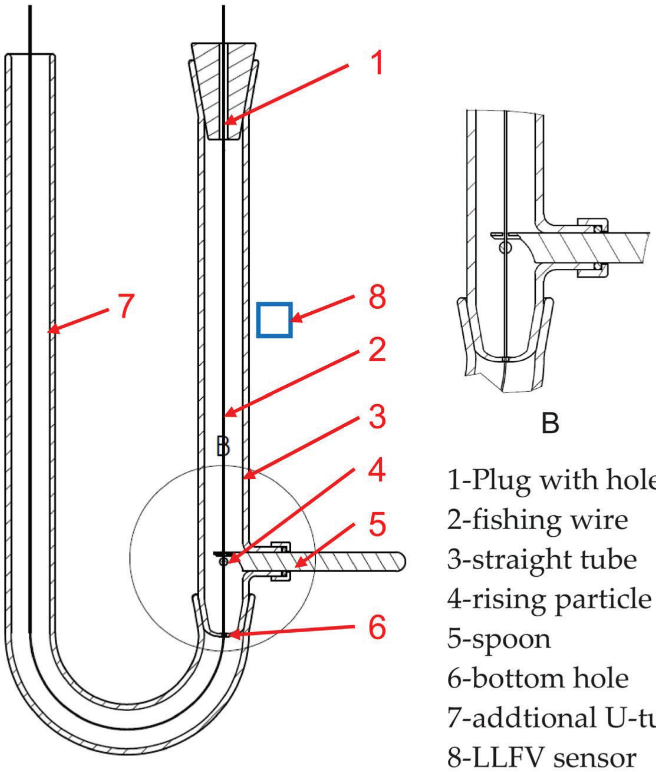

1-Plug with hole
2-fishing wire
3-straight tube
4-rising particle
5-spoon
6-bottom hole
7-addtional U-tube
8-LLFV sensor

Figure 3.3: Schematic of the experimental setup for particle rising in a thin tube.

3.46×10^6 S/m is the conductivity of GaInSn at 20 °C. This value demonstrates that in the present experiment the Lorentz force dominates the friction effects. As expected, the magnetic Reynolds number Re_m is small according to equation (2.11):

$$Re_m = \mu_0 \sigma u_0 d = 0.0057, \tag{3.3}$$

which suggests that the secondary magnetic field can be neglected due to $Re_m \ll 1$. Finally, to describe the ratio of the Lorentz forces to the inertial forces, we have the interaction parameter N:

$$N = \frac{\sigma B_0^2 d}{\rho u_0} = 0.0321, \tag{3.4}$$

which is small in our experiments.

3.2.2 Results

In one measurement, shortly after we start the LFV sensor, the spoon (in figure 3.3) is removed and the particle starts to rise, following the straight fishing line. When the displacement flow by the particle rising affects the region permeated by the magnetic field,

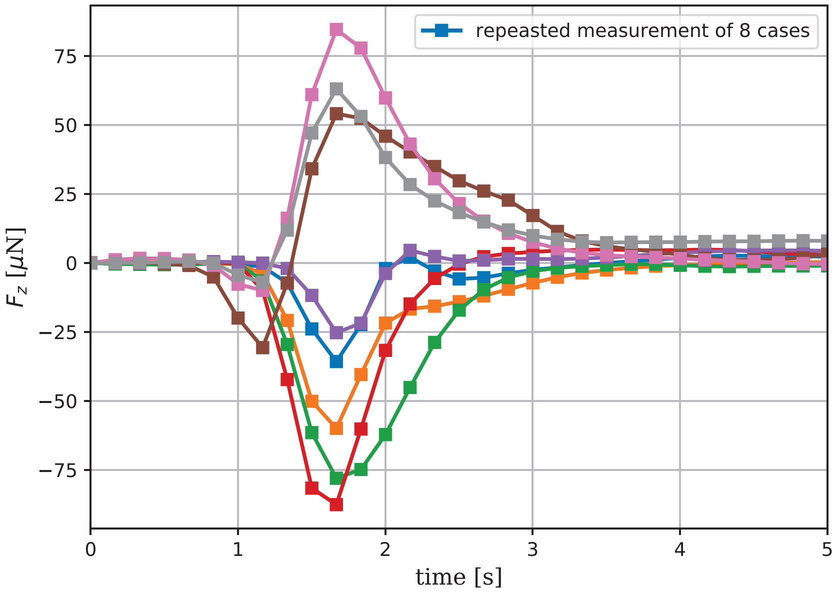

Figure 3.4: LFV measurements of particle rising in a thin tube.

the Lorentz force is generated. In LFV we measure the counter force to this flow-braking Lorentz force. After seeing that the particle reaches the top free surface, we stop LFV measurement. Then the particle is pulled down to the bottom of the tube and we wait till the liquid comes to rest again. We repeat this process. The results of eight repeated measurements as such are shown in figure 3.4. They are coordinated by the time of peak to $t = 1.6$ s. We observe that Lorentz force signals vary significantly when the particle moves through the test region. Three cases are upwards the other five downwards. The peak values vary from -80 μN to +80 μN. A prolonged tail occurs at $t = 2 - 4$ s.

We cannot observe good reproducibility, because of the limitations of the experimental configuration:

- Particle rising velocity following the fishing line may differ a bit for each case, due to hydrodynamic instability at $Re \sim 3000$.
- LFV is very sensitive to lateral position of particle, which may differ a bit because of the elasticity of the fishing line.
- The tube is too thin for the displacement flow to develop, i.e. the wall effect is so strong that it introduces perturbations
- The signal frequency may approach the resonance of LFV, which leads to significant variations after the default embedded data processing.

3.2.3 Summary

The response of LFV to a simple arrangement of particle rising in liquid GaInSn in a thin tube was investigated. It proves that particle rising in liquid metal can be detected by LFV. However, the Lorentz force signals vary significantly when the particle moves through the test region, possibly caused by strong wall-effect, the uncertainty of particle velocity, particle lateral position or default embedded data processing. Therefore, an extended experiment to overcome these limitations is conducted and will be described in the following section 3.3.

3.3 Experiment of controllable particle motion in a large vessel

The extended experiment of controllable particle is designed to overcome the limitations of the previous test in section 3.2. Here a larger cuboid vessel is used to exclude the wall effects. The particle rises not "freely" anymore but under controllable velocity driven by the fishing line, therefore a broader range of the Reynolds number *Re* can be explored. A UDV probe operates synchronously with LFV and is installed at the same height of LFV, which detects when the particle moves through and provides the reference "zero time" for LFV signals. The extended configuration consists a robust aluminium profile linked with a stone table, thus the system noise is restrained dramatically. There has been much effort to tackle the signal-processing of LFV as described in section 2.5, which turns out to be sufficient for particle detections. One example of LFV measurement in section 3.3.2 shows the functionality of the data-processing.

3.3.1 Experimental setup

As shown in figure 3.5, the experimental setup consists of a plastic vessel filled with liquid metal GaInSn. The new vessel has the inner volume $60 \times 60 \times 400$ mm^3 and the wall thickness of 8 mm. The spherical particle made of plastic (diameter of 6 mm) is electrically non-conducting and fixed on the fishing line, which is pulled through the top and bottom holes of the vessel and moves in 10 mm-distance in parallel to the side-wall. The velocity of the sphere is controlled by an additional linear driver, which provides speeds in the range of $0 - 200$ mm/s. The effect of the moving fishing line is neglected because of its small size (0.1 mm in diameter). To prevent the leakage of liquid through the hole for fishing line on the bottom plate, an additional tube is installed vertically on the side and it is linked to the bottom hole via silicon soft tube. Such configuration forms as the "U-tube" system, through which the fishing line is pulled straight by a constant load outside. As in the previous test, LFV consists of a $12 \times 12 \times 12$ mm^3 permanent magnet, which is installed in 1 mm distance to the side wall. Thus the distance between the magnet surface and the liquid is 9 mm, and the distance between the magnet surface and particle center is 19 mm. LFV measures the $z-$ or $x-$ component of Lorentz forces under two arrangements, respectively. It should be noted that changing the orientation of IOFS does not influence the static character of LFV, however such effect on its dynamic characterizations must be considered, which was described in section 2.5.2. A photo of the arrangement for horizontal measurement (F_x) is shown in figure 3.6. The "arm alike" aluminium adapter is manufactured to assist lift-force measurement. The definition of parameters of the configuration is shown in figure 3.7 briefly.

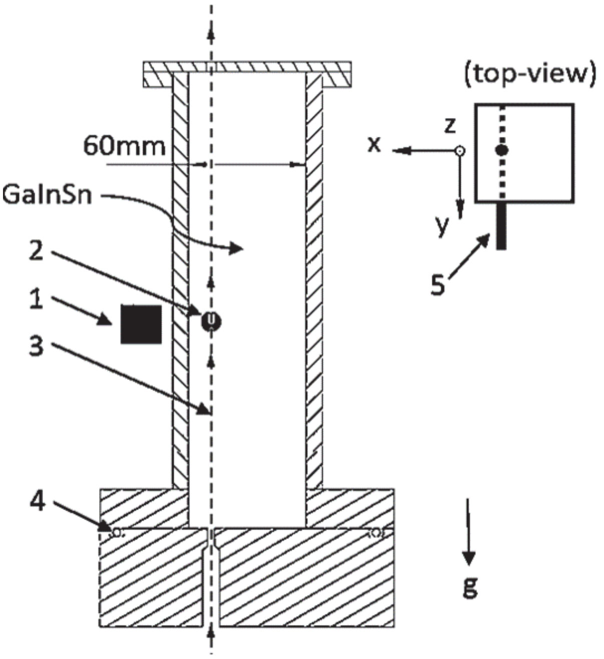

Figure 3.5: Schematic of the experiment of controllable particle motion in liquid metal.
(1 LFV; 2 Spherical particle; 3 Fishing line; 4 O-ring; 5 UDV.)

As shown in figure 3.5 (top-view) as well, an UDV measurement in installed to assist the time-coordination of LFV signals. A trigger is applied in the present experiment by a DC coil near the magnet, which is linked with the starting triggers of the UDV measurement.The UDV records the echo level through liquid on the same height of LFV. The linear driver for the particle motion is activated by the trigger as well. Thus the reference time t_0 for the particle going through is provided, and a synchronized system across LFV, UDV and particle motion is realized. A schematic of the measurement procedure is shown in figure 3.8.

It should be noted that there are different modes of the LFV measurements (described in section 2.5). Here two modes are applied respectively, i.e. the slow mode with default data-processing and the super-fast mode with manual post-processing. The manual post-processing of data proceeds by the following steps:

Step i the dynamic compensation aims to exclude the effects of the resonance of LFV,

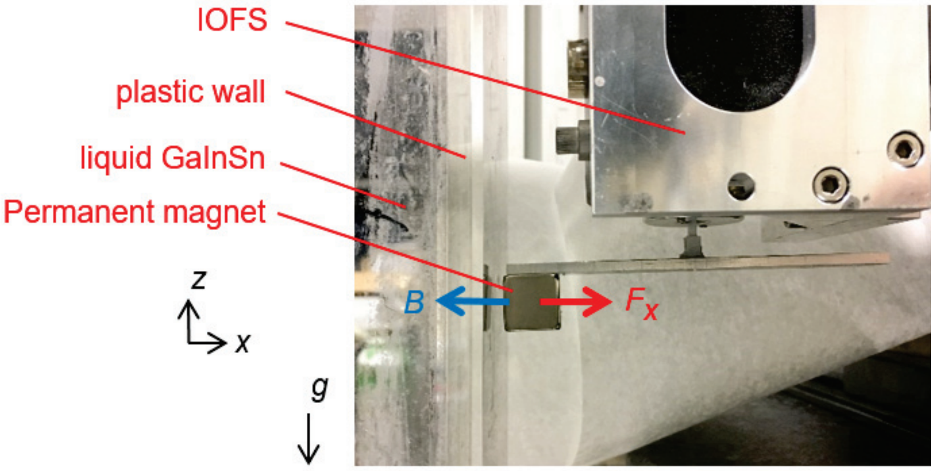

Figure 3.6: Photo of the experimental setup for controllable particle motion in liquid metal (in the arrangement for lift force F_x measurement).

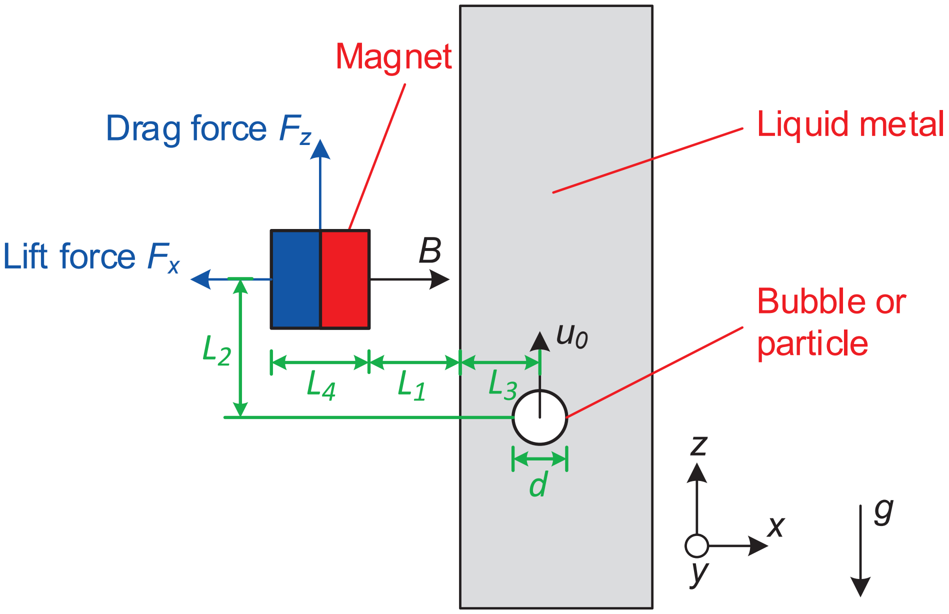

Figure 3.7: Schematic of the parameter definition for the problem of particle motion.

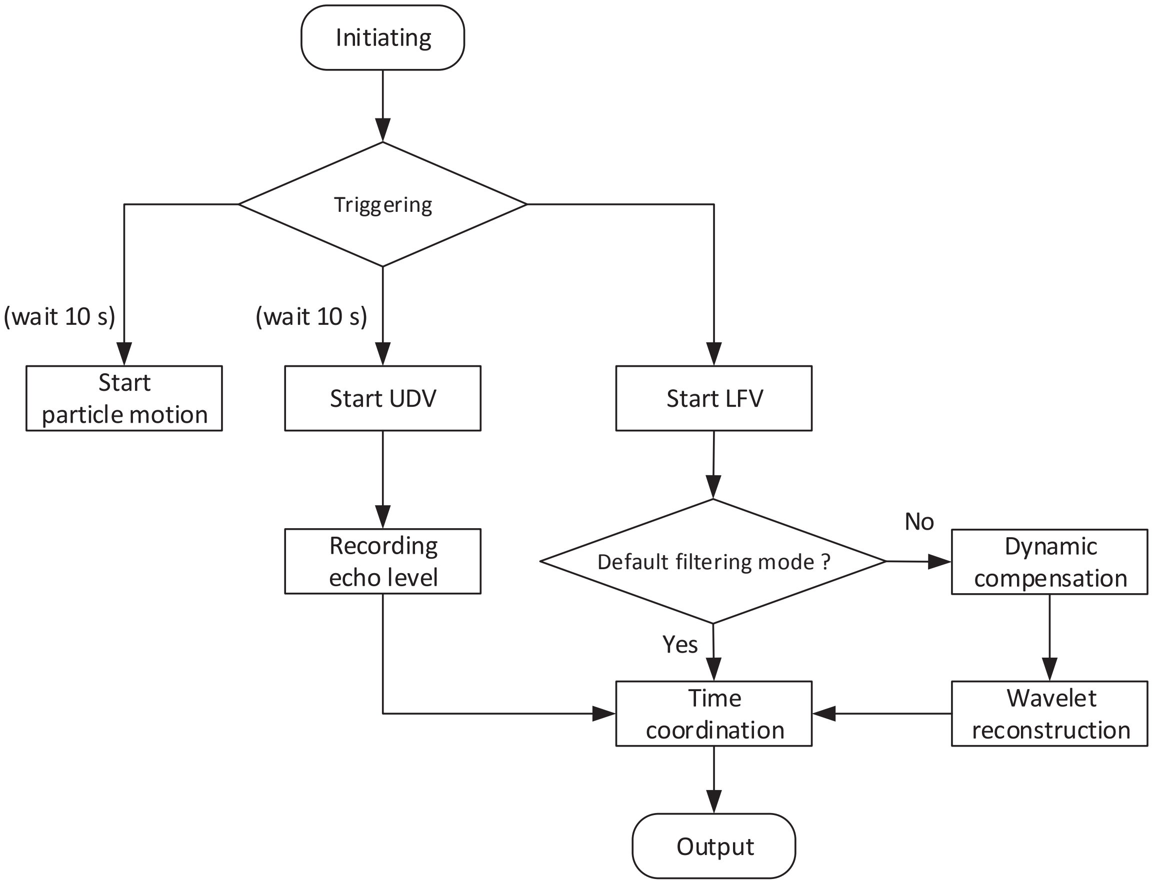

Figure 3.8: Schematic of the measurement procedure for particle experiment.

Step ii the wavelet filter is used to de-noise the signal,

Step iii the reference time t_0 is determined by the synchronized UDV measurements.

One example of the data-processing will follow next in section 3.3.2

3.3.2 Data processing

In the present experiment, we switch off the default filter and collect the raw data of LFV at the sampling rate of 781.25 Hz. Details of the operation modes and data-processing of IOFS were described in section 2.5. The data-processing is evaluated by signals of particle motion in liquid metal. Figure 3.9 shows an example of measurement at $Re = 1000$ to validate the method. The raw data of LFV is plotted as light grey color in figure 3.9a, while the blue curve represents the signal after the dynamic compensation. We see that the noise is removed significantly. Afterwards, the wavelet filter is used to further de-noise the signal, and the result is shown in figure 3.9b. The square wave (manual input as trigger) on LFV at $t = 0 - 2$ s is well observed, of which the rising slope is the trigger and it starts automatically the particle motion and UDV measurement 10 seconds afterwards. The triggering program sets the particle to start at $t = 10$ s from the bottom of the liquid. Seen from the synchronized UDV echo results in figure 3.9c, a pulse occurs at $t = 12.8$ s, which indicates that this is the reference time t_0 when the particle come through the same height of LFV. The reference time t_0 is reflected to the LFV signals in figure 3.9b. The particle stops at the top of vessel at about $t = 15.6$ s. A long tail of LFV signal is observed after particle stops, because the vortices still exist in the vessel and take some time to dissipate by viscosity and Lorentz force braking.

From the tests of 1 Hz input force (in section 2.5.2) and particle signals here, the method of signal-processing is proved to be accurate, which will be continued again by the numerical and experimental results later on. Unless specifically stated, the following results are obtained by this approach.

3.3.3 Results

Result of particle motion near the wall

The LFV measurement results of ten repeated cases of particle motion near the wall (10 mm parallel to the wall) are shown in figure 3.10. It should be noted that signals are close to the resolution of LFV (1 μN), therefore some perturbations in signals as noise cannot be avoided. With the particle velocity $u_0 = 10$ mm/s ($Re = 160$) and the particle traveling distance 283 mm, the traveling time of the particle is 28.3 seconds, during which we observe the "double

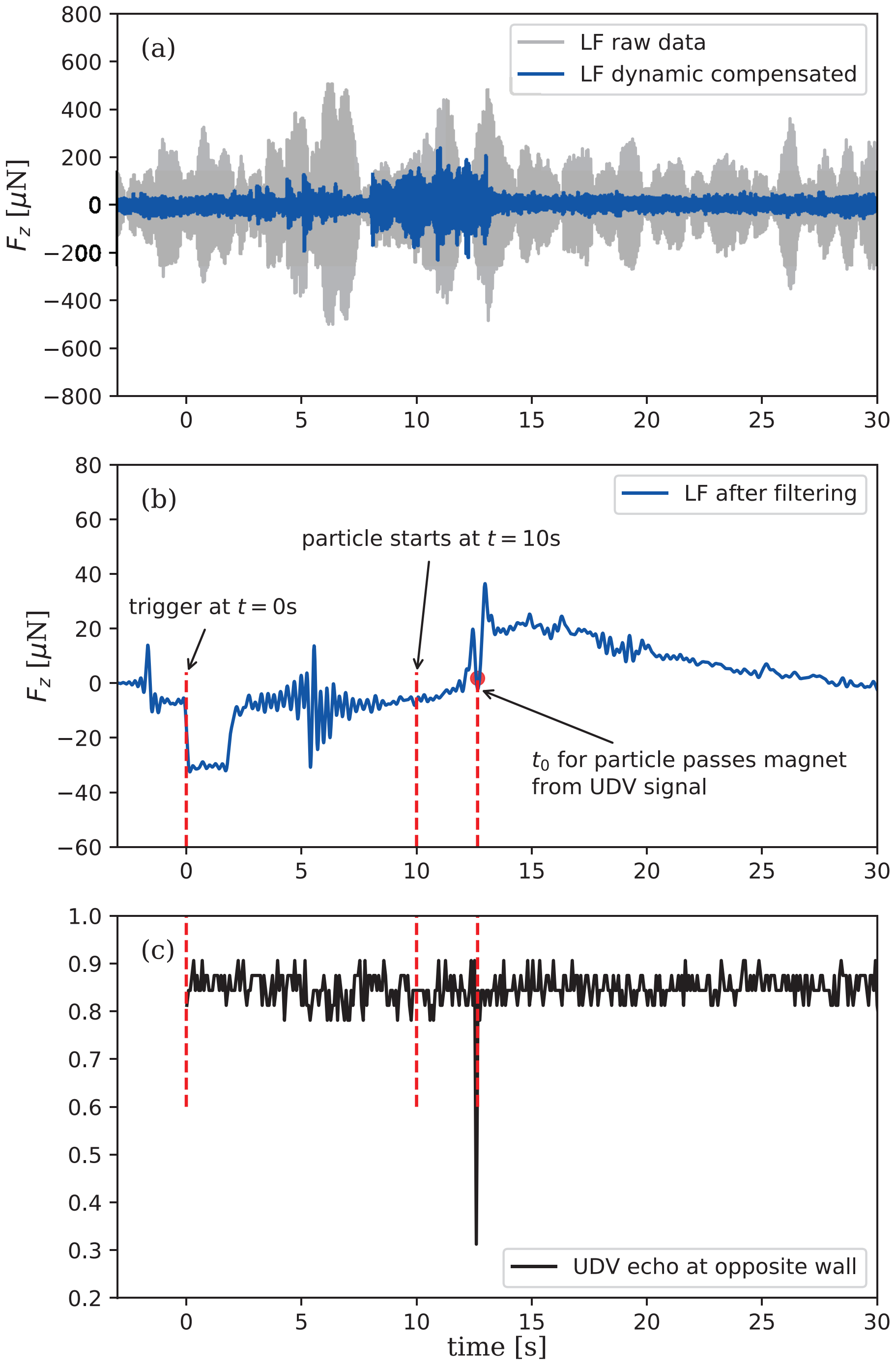

Figure 3.9: Example of data processing for particle moving (at $Re = 1000$).

peaks" of Lorentz forces. In between these two peaks, the trough occurs at 14.15 s, when the particle is right at same height of LFV (reference time t_0). Additionally, the first peaks are $2.3 - 3$ μN and occur shortly before the zero position, while the second peaks are $4 - 4.8$ μN and after the zero position. After 28.3 seconds the particle stops its motion, but there are still Lorentz force signals lasting about 20 seconds due to the remaining liquid motions in the vessel. In such cases we observe the good reproducibility of the force signals, which can hardly been seen in the previous experiment in section 3.2. This is because the Reynolds number now ($\sim$ 160) is much lower than that in the previous study ($\sim$ 3000), and here the wake behind the sphere is still a "Stable Vortex Region". According to Taneda [120], the vortex-ring in the wake of a sphere starts to oscillate at about $Re = 220$.

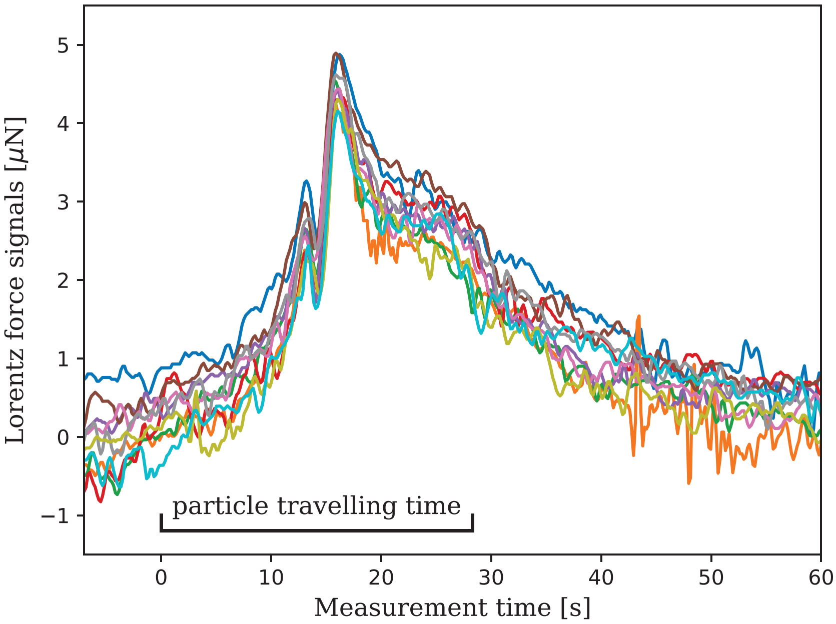

Figure 3.10: Ten cases of LFV measurements for particle motion near to the wall at $u_0 = 10$ mm/s.

To better illustrate the time-series of LFV data, the time-scheme is transformed to the relative length scale, namely

$$(t_m - t_0) \cdot u_0 / d,$$

where t_m, t_0 is the measurement time. Using such scheme, two cases of drag (F_z) and lift (F_x) force measurements at $Re = 200$ are shown in figure 3.11bc, respectively. The results are very similar to that in $Re = 160$. The particle motion in z- direction is illustrated in figure 3.11a. Concerning drag force, we observe the first peak of 2 μN occurs at position -1.6, and afterwards the trough of 1 μN at zero position. The trough occurs because the particle is electrically non-conductive. At zero position, where the particle is nearest to the magnet,

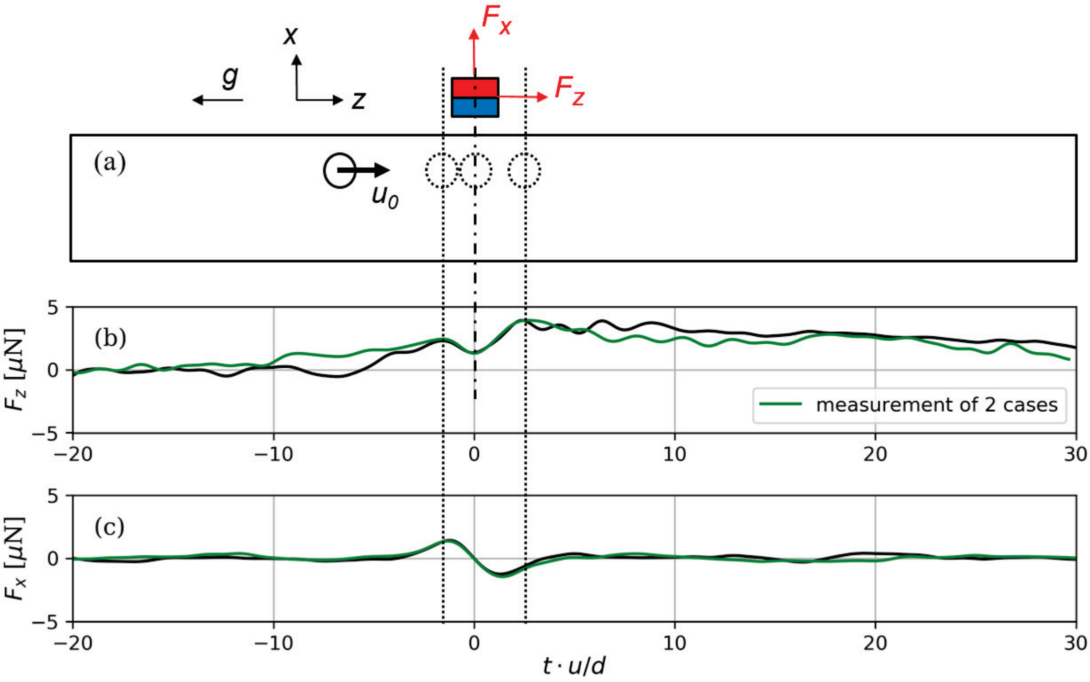

Figure 3.11: LFV measurements for particle motion near to the wall at $Re = 200$.

although the local velocity is bit higher than that at position -1.6, the conductive volume near the magnet contributing to overall Lorentz force decreases significantly, which leads to the decease of overall F_z. The second peak is of 3 μN at position 2.5, which is surely in the wake. The "double peak" effect of F_z will be shown and discussed again in numerical modeling in section 3.4.2. The lift force F_x is shown in figure 3.11c, which has the shape of “zero-crossing-pulse". The peaks and troughs are ± 1.4 μN at position ± 1.2, and the “crossing-zero" occurs precisely at zero position. This can be obviously explained by the velocity field around particle. Before zero position, the liquid are forced to flow around particle. Therefore the velocity near the magnet region points to the wall, resulting a positive F_x on LFV, and vice versa at the position downstream.

Higher Re is investigated as well. The results of four repeated measurements at $Re = 2000$ are shown in figure 3.12. We observe that the increased Re leads to more variations between repeated cases (due to hydrodynamic instability) and longer "tail region". Lorentz force does return zero after about one minute, which is not illustrated in figure 3.12a.

It should be noted that the fluid is at rest during the measurement. However in the case of particle motion in a pipe flow (typical in industrial applications), where the turbulence is present with particle, the drag force should consist of an additional component of fluctuated background force, and it may be more difficult to analyze the LFV data. In figures 3.11c and 3.12b we observe very good reproducibility of lift forces in experiments even at high Re, because lift force is perpendicular to the direction of particle velocity and therefore less

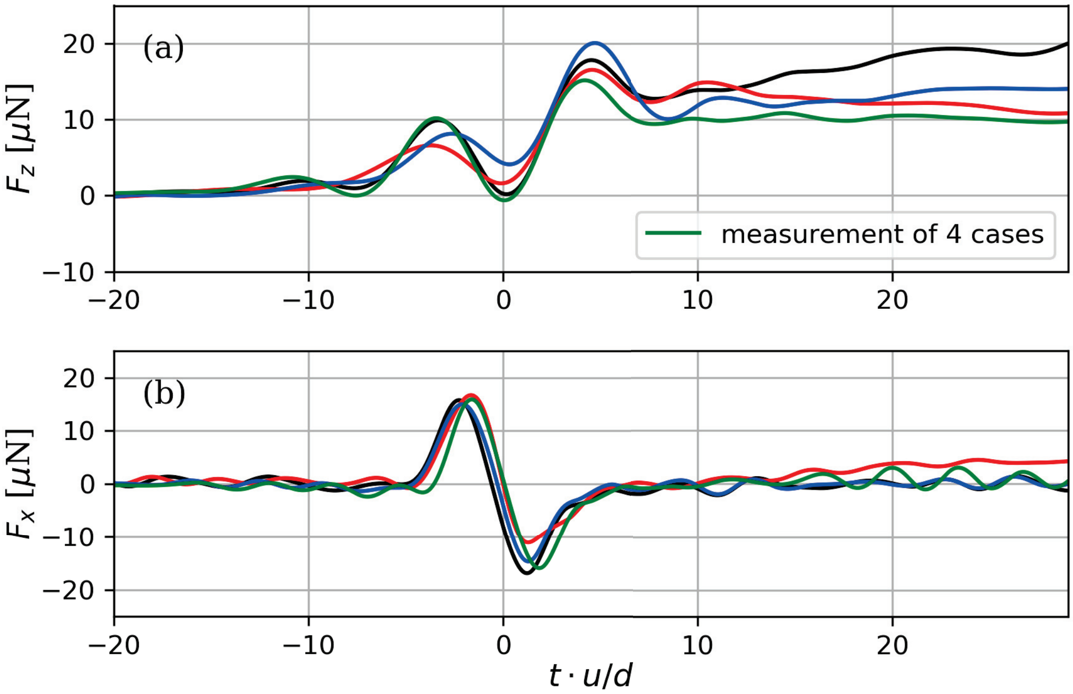

Figure 3.12: LFV measurements for particle motion near to the wall at $Re = 2000$.

sensitive to unsteady turbulent wakes comparing to drag force. We may consider the lift force more “robust” for applications comparing to drag force, especially for complex flows.

It is also interesting to validate the dependence of LFV on *Re* (particle velocity). As Lorentz force signals have complex shapes, it is not advantageous to select solely the values of first peak, trough, or others. Here a straightforward approach is used, which simply selects the maximum value of time-series. The results are shown in figure 3.13. A linear dependence of max. lift force over *Re* is observed. It is unclear whether this linear scaling breaks at even higher *Re* (> 2000), as it is above the capability of the present experimental configuration.

Result of particle motion far from the wall

All the patterns of LFV signal change if the particle moving further (although still parallelly) to the wall. Nine repeated measurements of drag force F_z of particle motion at 30 mm parallel to the wall are shown in figure 3.14. The velocity in such cases are $u_0 = 100$ mm/s ($Re = 1630$). Even lower velocity cannot be measured due to sensor resolution, as the magnetic flux B_x decrease significantly with the distance. The zero positions are set at $t_0 = 0.3$ s manually. The "double peak" pattern (regarding the near-wall case) disappears and merges into a single negative pulse at t_0. The tails last longer. Such differences compared to the near-wall cases are caused by:

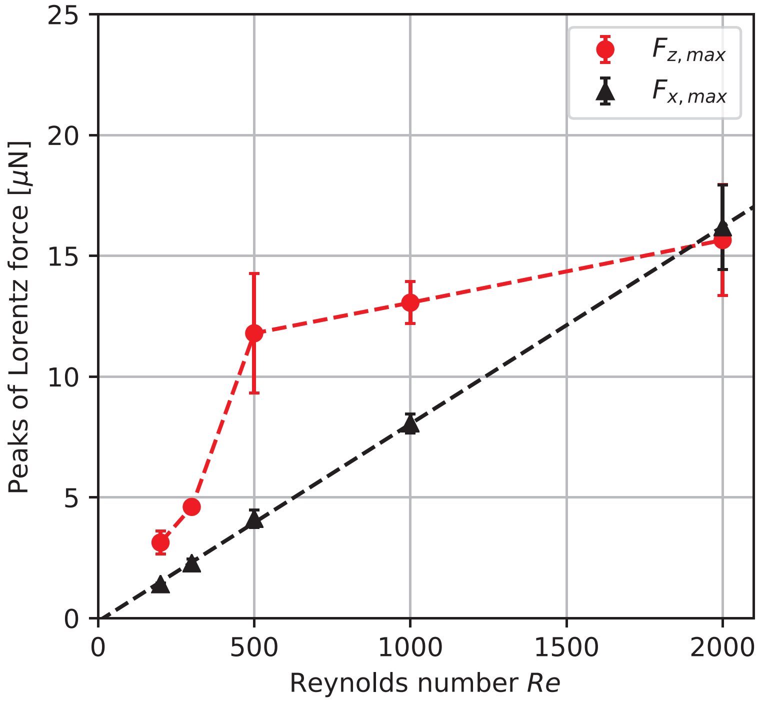

Figure 3.13: Effects of velocity (Reynolds number *Re*) on drag and lift forces.

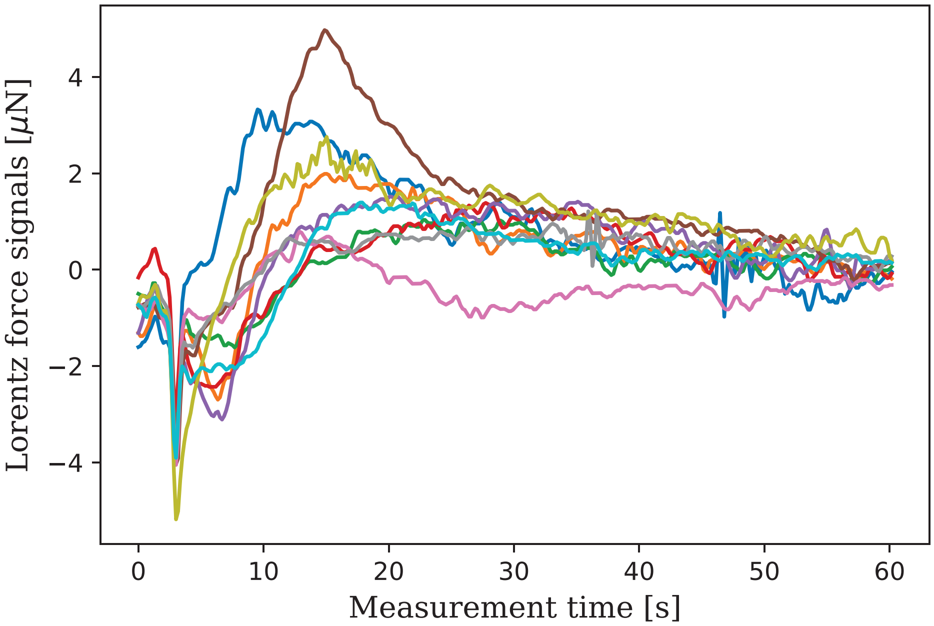

Figure 3.14: LFV measurement for particle motion far from the wall at $Re = 1630$.

- The "sensitive region" for LFV become broader when the particle is further away. The trough between the "double peaks" on drag force F_z becomes insignificant, because the negative contribution of "non-conductive volume of particle" to LFV becomes weaker.
- There are less wall effects when the particle is further away. There is more space for the local flow to develop, which leads to more chaotic wakes of fluid motion and longer tails in LFV signals.

3.3.4 Summary

The extended experimental setup was successfully used to perform LFV measurements of controllable particle motion in liquid metal. A very good reproducibility is achieved. The data-processing is described and verified. The dependence of maximum Lorentz forces on the Reynolds number Re is discussed.

3.4 Comparison with numerical models

Two approaches of numerical modeling for the particle moving problem are described in the present section, namely "kinematic modeling using analytical velocity field" by commercial software COMSOL Multiphysics and "MHD modeling" by commercial software ANSYS Fluent. The geometries in the modelings are identical to the previous experiment in section 3.3. We will show a promising agreement between measurement and simulations.

3.4.1 Kinematic modeling using analytical velocity field

Since the interaction parameter $N \ll 1$, we may firstly use the so-called "kinematic approach" for our numerical simulation for a quick validation, as mentioned in section 2.2.3. To be more straight forward, the velocity u_{hydro} in equation (2.17) is firstly prescribed by the analytical solutions of the flow around a moving sphere at low Re.

The geometry of the simulation is identical to the experiment in section 3.3 (figure 3.7). In modeling the z-axial distance between the magnet and the sphere $L_2 \in [-90, 90]$ mm. As described in section 2.2.3, we compute the electromagnetic induction of a pre-defined velocity field and the localized magnetic field from a cubic permanent magnet. To describe the velocity field using the analytical solutions, a spherical coordinate system is introduced and fixed on the center of the sphere:

$$z = r\cos\theta, \quad x = r\sin\theta\cos\phi, \quad y = r\sin\theta\sin\phi. \tag{3.5}$$

We use the analytical solutions of the flow generated by a sphere moving in the negative z-direction, which was originally found by Oseen [82]. Usually it is represented as a Stokes stream function. The radial and angular components of velocity are

$$\begin{aligned} u_r &= -u_0 \frac{3ra^2 \exp(Re(\cos\theta - 1)r/(2a))(Re(1+\cos\theta)r/a + 2) - 2a^3(3r/a + Re\cos\theta)}{4r^3 Re}, \\ u_\theta &= u_0 \frac{\sin\theta\left(3ar^2 \exp(rRe(\cos\theta - 1)/(2a)) + a^3\right)}{4r^3}, \\ u_\phi &= 0, \end{aligned} \tag{3.6}$$

where r is the radial coordinate, $a = d/2$ is the sphere radius, and Re is one half of the particle Reynolds number, respectively. Then we implement equation (3.6) into our geometry as

$$\begin{aligned} u_z &= u_r \cos\theta - u_\theta \sin\theta, \\ u_x &= u_r \sin\theta\cos\phi + u_\theta \cos\theta\cos\phi, \\ u_y &= u_r \sin\theta\sin\phi + u_\theta \cos\theta\sin\phi. \end{aligned} \tag{3.7}$$

The imposed magnetic field of the permanent magnet is calculated from the analytical solution presented by Furlani [33], which is determined by the integration of

$$\boldsymbol{B_0}(x,y,z) = \frac{\mu_0 M_s}{4\pi} \sum_{k=1}^{2} (-1)^k \int_{z_1}^{z_2} \int_{y_1}^{y_2} \frac{[(x-x')\boldsymbol{e_x} + (y-y')\boldsymbol{e_y} + (z-z_k)\boldsymbol{e_z}]}{[(x-x')^2 + (y-y')^2 + (z-z_k)^2]^{3/2}} dy'dz', \tag{3.8}$$

where M_s is the surface magnetization of the magnet along the x-axis, (x_1, x_2), (y_1, y_2), (z_1, z_2) are the coordinates of the magnet's corners, $\boldsymbol{e_x}$, $\boldsymbol{e_y}$, $\boldsymbol{e_z}$ are the unit vector in the x, y, z directions and the edges of the magnet are parallel to either $\boldsymbol{e_x}$, $\boldsymbol{e_y}$, $\boldsymbol{e_z}$, respectively.

The measurement and modeling of B_x based on equation (3.8) are compared in figure 3.15, which shows very good agreement. The finite Element Method (FEM) is used to determine the forces acting in the fluid. The solution domain is a rectangular cuboid with a sphere cut out. For this model we use the hybrid tetrahedral mesh. In the computational domain, the elements are uniformly distributed over the x-axis. Smaller elements are applied in the region where the gradient of velocity field is large. The influence of discretization was examined by using meshes with different numbers of elements. The mesh used in subsequent computations is shown in figure 3.16, where the surface mesh of the sphere can be seen as well. The effect of mesh quality on the Lorentz forces is checked by validating the max. drag force $F_{z,max}$ and shown in figure 3.17, by which we show the deviation of force amplitude of $\frac{F_i - F_0}{F_0}$, where F_0 is the Lorentz force ($L_2 = 0$, $u_0 = 10$ mm/s, $Re = 0.01$) in the case of maximum number of mesh elements. The influence of mesh quality on Lorentz forces $F_{z,max}$ is below 10^{-3}.

In the following results, we set $u_0 = 10$ mm/s in the negative z- direction and investigate the velocity profile depending on the Reynolds number. Although Re should depend on u_0, one may still be able to check the influence of Reynolds number on the asymmetry of the flow

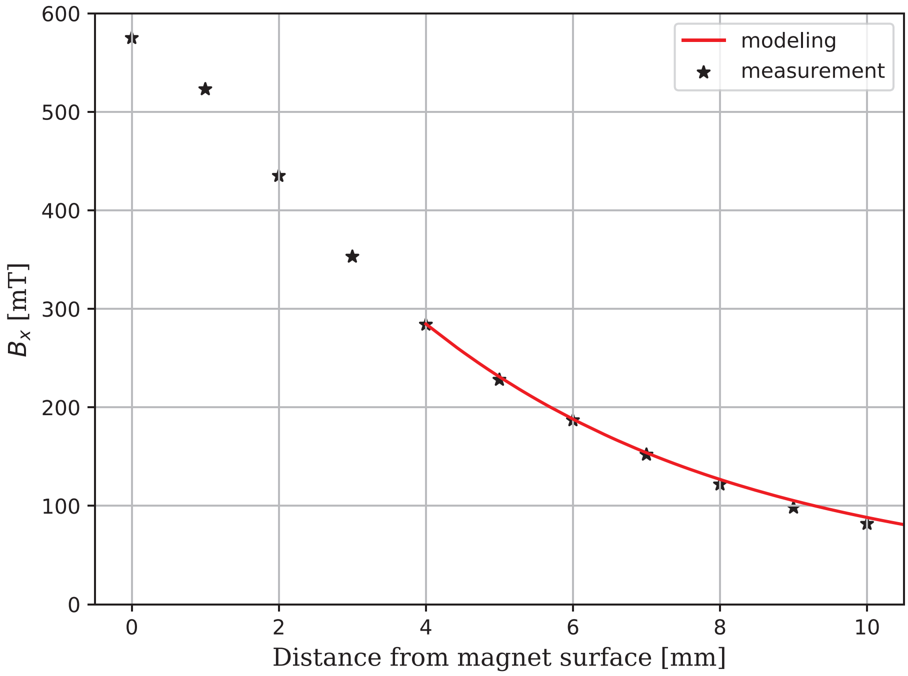

Figure 3.15: Comparison of magnetic flux density B_x in experiment and modeling.

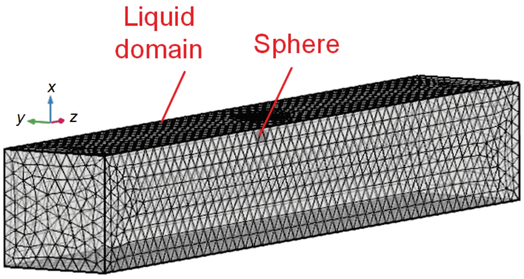

Figure 3.16: Mesh used in kinematic modeling with 6.8×10^4 elements.

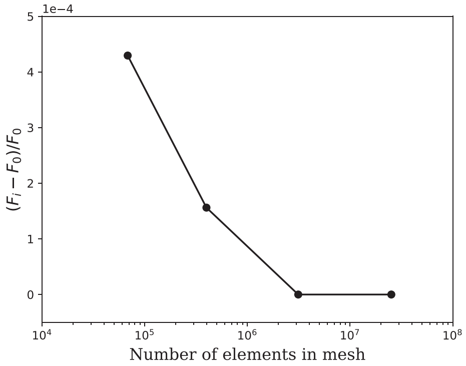

Figure 3.17: Mesh study with $Re = 0.01$, $u_0 = 10$ mm/s, at $L_2 = 0$ mm.

by assuming a constant velocity and an adjustable viscosity. The velocity fields on the x-z plane with $Re = 0.1, 1, 2, 5$ are shown in figure 3.18, respectively. We observe that the velocity field around the sphere becomes more asymmetrical as Re increases. However, when $Re > 1$, the velocity fields of the Oseen's solution are significantly suppressed in the near-sphere region and becomes unphysical. Therefore we are only interested in the cases of $Re \leq 1$. It should be noted that Oseen's solution is derived for an unbounded flow around the sphere. Since the distance to the wall here is not very large, the velocity is non-zero on walls in the present case, which may cause errors in modeling. We do not expect the analytical flow to correspond closely to the actual flows in the experiment. Nevertheless, it may be presumed that the relatively slowly decaying viscous velocity distributions provide an indication of the maximal force signals.

To reproduce the measurement cases, in the numerical model we set the permanent magnet to different locations (e.g. $L_2 = -10, -4, 0, 4, 10$ mm) and observe the development of the eddy current density distributions and the Lorentz force density distributions, which are shown on the x-z symmetry plane ($z \in [-50, 50]$ mm, $x \in [-20, 10]$ mm) in figures 3.19 and 3.20, respectively. Figure 3.19 shows that the eddy currents are mainly induced in the near-magnet region and the near-particle region, because the velocity and $\boldsymbol{B_0}$ are more significant there. We observe the asymmetry of the eddy current density distributions. A more significant induction of eddy current occurs downstream the "zero" position instead of that at the "zero" position. This is obviously caused by the asymmetrical velocity field at $Re = 1$. The Lorentz force density distributions in figure 3.20 shows the asymmetry with respect to the "zero" position as well. Additionally we observe more contribution of the Lorentz force density to the total force in the near-magnet region than that in the case of eddy current density distribution because of the large gradient of $\boldsymbol{B_0}$ in the x-direction.

From simulation we receive total Lorentz forces that depend on the axial distance L_2 between the magnet and the sphere. The result of drag force F_z is shown in figure 3.21. It shows that $F_{z,max}$ decrease as Re increases. Additionally we observe the trend of asymmetry of velocity field depending on Re. The higher the Re is, the further the Lorentz force peak-position is shifted away from "zero" position $L_2 = 0$. It should be noticed that the results are physical only at low Reynolds number cases ($Re \leq 1$). One measurement of $Re = 160$ is illustrated in figure 3.21 as well. Unfortunately the Reynolds number in measurement is beyond the capability of our velocity solution, and thus we cannot do a one-to-one comparison. However the measurement and the simulations together show a reasonable trend. Our model can provide the upper-limit of the Lorentz force for the experiment.

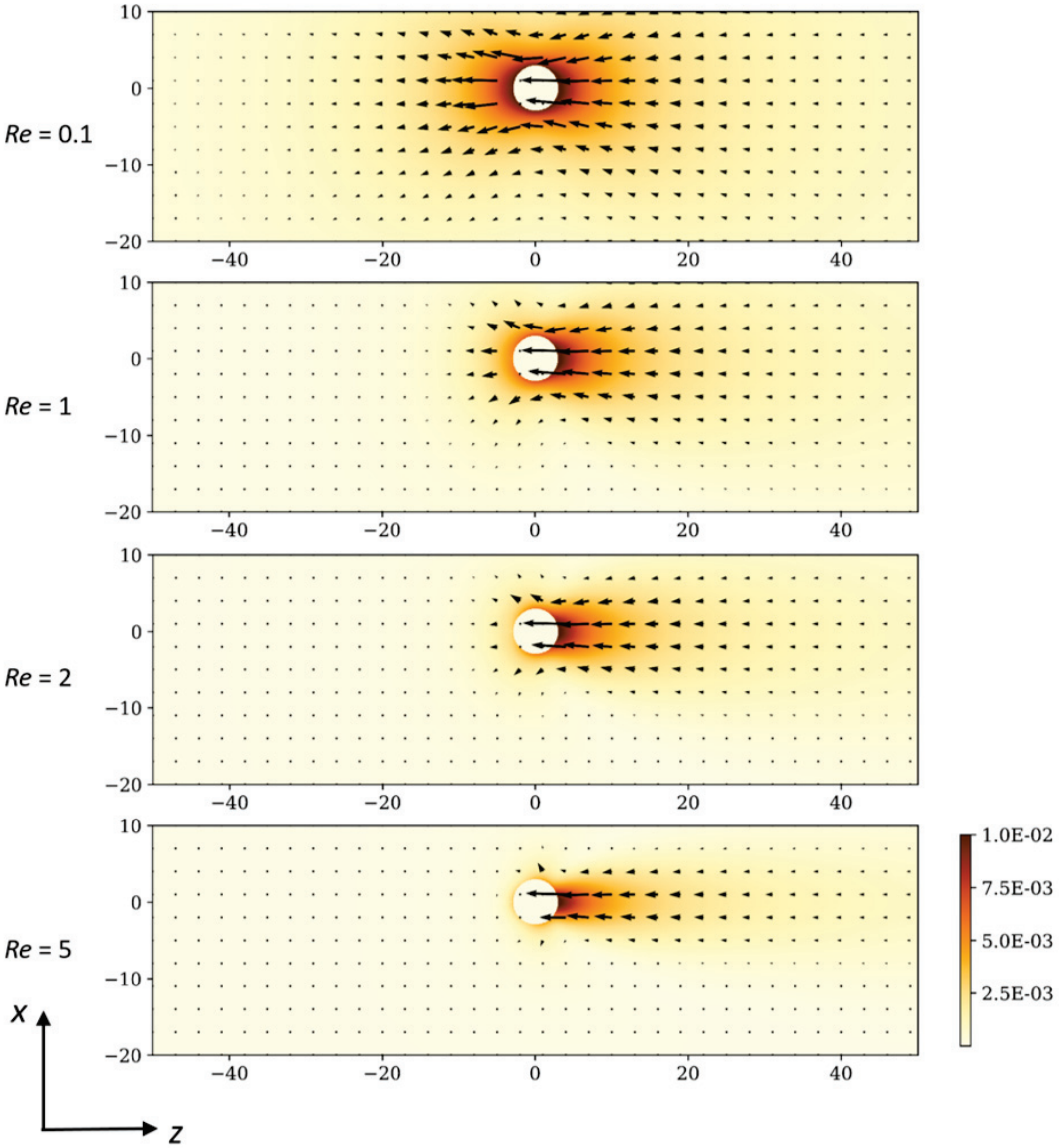

Figure 3.18: The vector and contour of the velocity field in kinematic modeling on the x-z plane ($u_0 = 10$ mm/s, vector of $\boldsymbol{u_x}, \boldsymbol{u_z}$, contour of $\sqrt{u_x^2 + u_z^2}$ [m/s], length unit in mm).

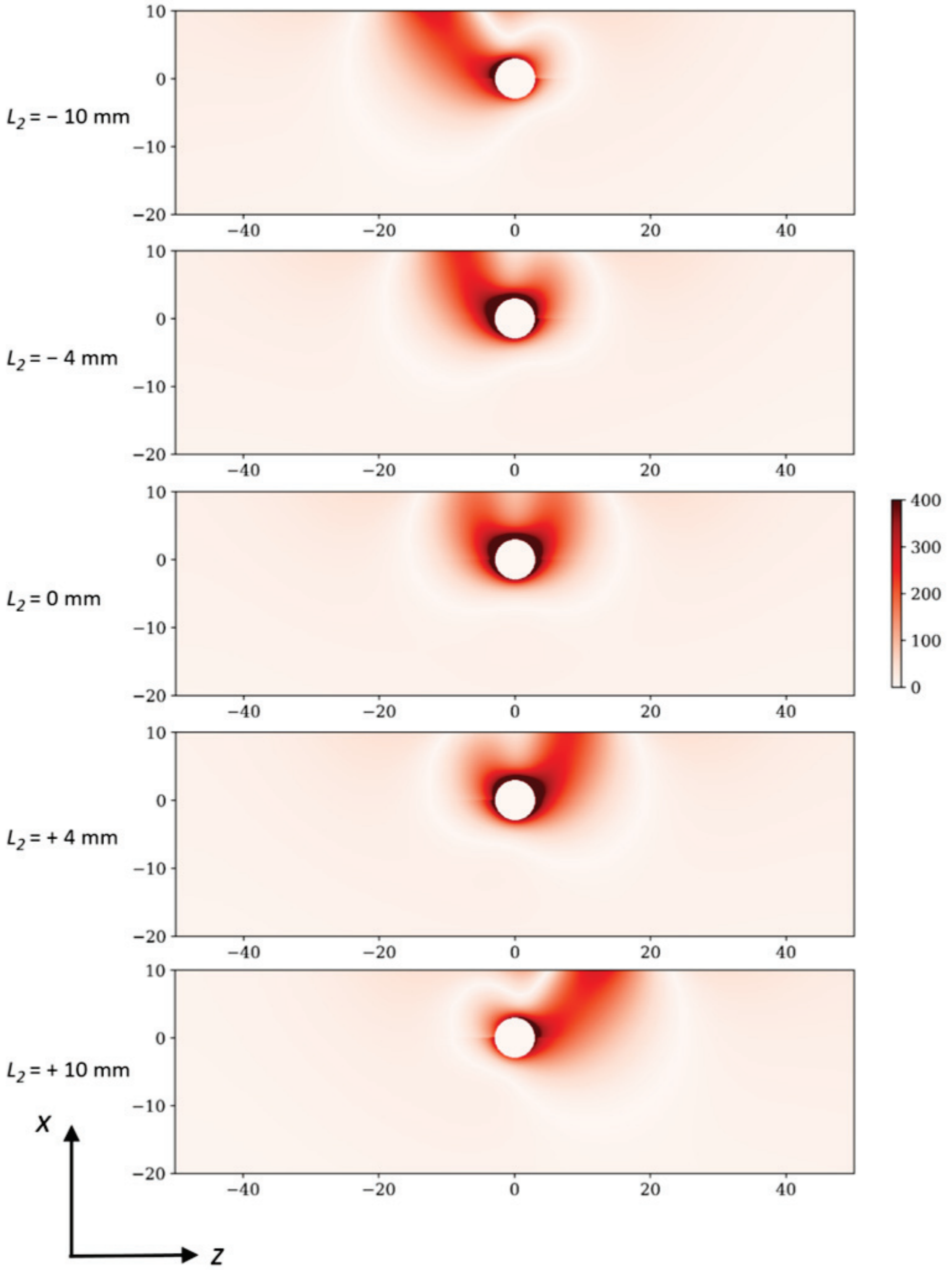

Figure 3.19: The contour of eddy current density distributions in kinematic modeling on the x-z plane ($Re = 1$, contour of $\sqrt{j_x^2 + j_y^2 + j_z^2}$ [A/m]^3, length unit in mm).

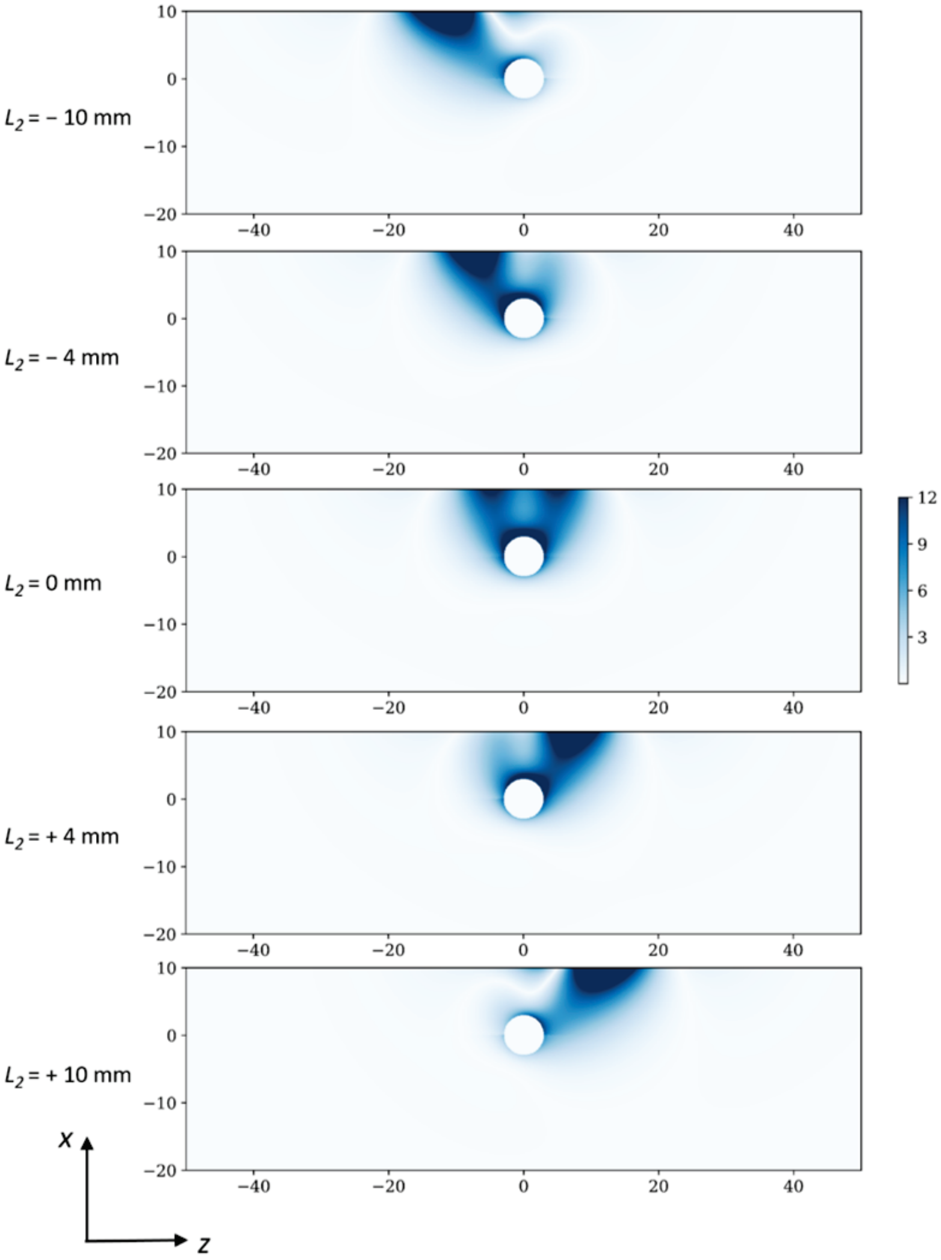

Figure 3.20: The contour of Lorentz force density distributions in kinematic modeling on the x-z plane ($Re = 1$, contour of $\sqrt{f_x^2 + f_y^2 + f_z^2}$ [N/m]^3, length unit in mm).

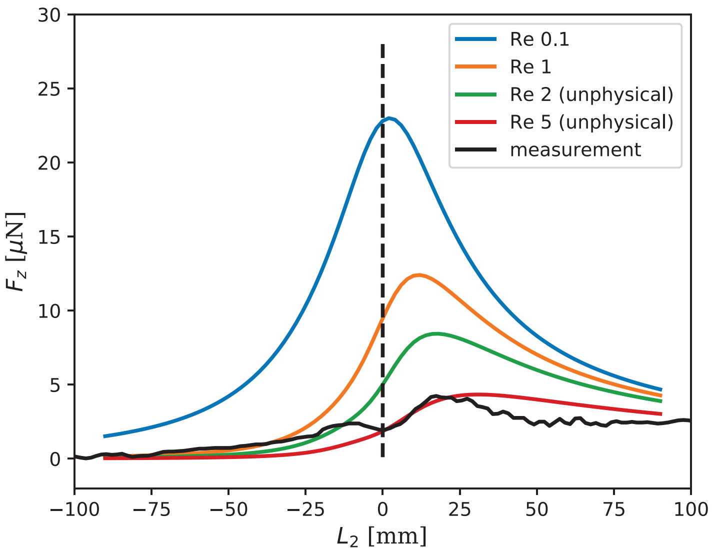

Figure 3.21: Lorentz forces in the experiment and kinematic modeling.

3.4.2 MHD modeling

The coupled MHD simulation were done by my colleague N. Tran using commercial software ANSYS Fluent. The Lorentz force term in the Navier-Stokes equations in the model can be switched off so that the kinematic approach can be validated as well. The results of $Re = 200,\ 2000$ are shown in figures 3.22 and 3.23, respectively. We observe promising agreement between the measurement and the modeling at both low and high Re. The difference between the kinematic- and MHD approaches are shown in figure 3.22bd. There is significant difference between the two approaches for drag force F_z, while such for lift force F_x is negligible. It should be noted that the effect of hydrodynamic instabilities at high Re is validated as well. Four simulations containing identical settings except that the initial velocity fields were taken from four snapshots of instantaneous velocities of a hydrodynamic flow past a sphere. The tiny difference among the initial velocity conditions should let the flow develop differently, however we observe no significant difference in the resulting Lorentz forces and therefore such comparison is not included. Please refer to Tran et al. [128] for details of the modeling.

A larger parameter space is explored using the numerical tools. We may consider the dependence of max. Lorentz force $F_{z,max}$ and $F_{x,max}$ over particle diameter d in figure 3.24. In the region of $Re = 200 - 1000$, Lorentz force peaks increase to approximately $d^{2.5}$.

The measurement system is limited in the size of the magnet, because the magnet should not be too heavy for IOFS to carry nor too light that target signal is too weak to capture. Such effects are explored thanks to the numerical tools. The effect of magnet-size L_4 on peaks of Lorentz force is shown in figure 3.25. We see that when the magnet side-length $L_4 < 20$ mm , the Lorentz force increases roughly to $\sim L_4^4$. A transition of scaling occurs at

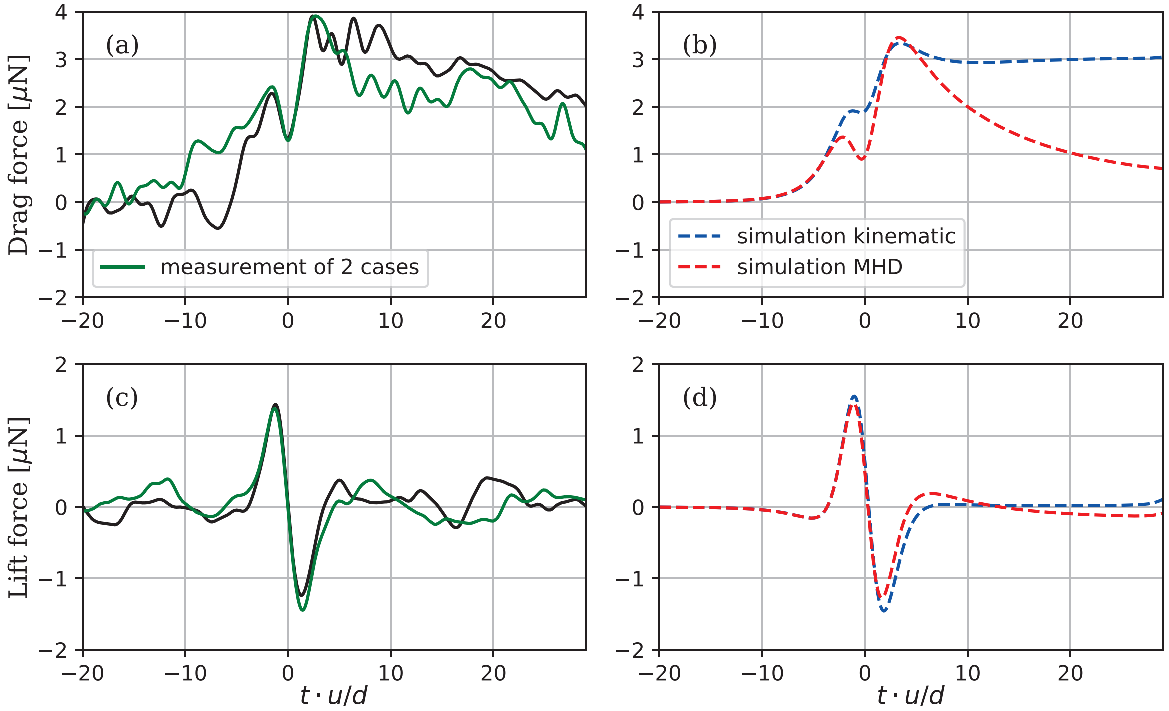

Figure 3.22: Lorentz forces in the experiment and MHD modeling at $Re = 200$.

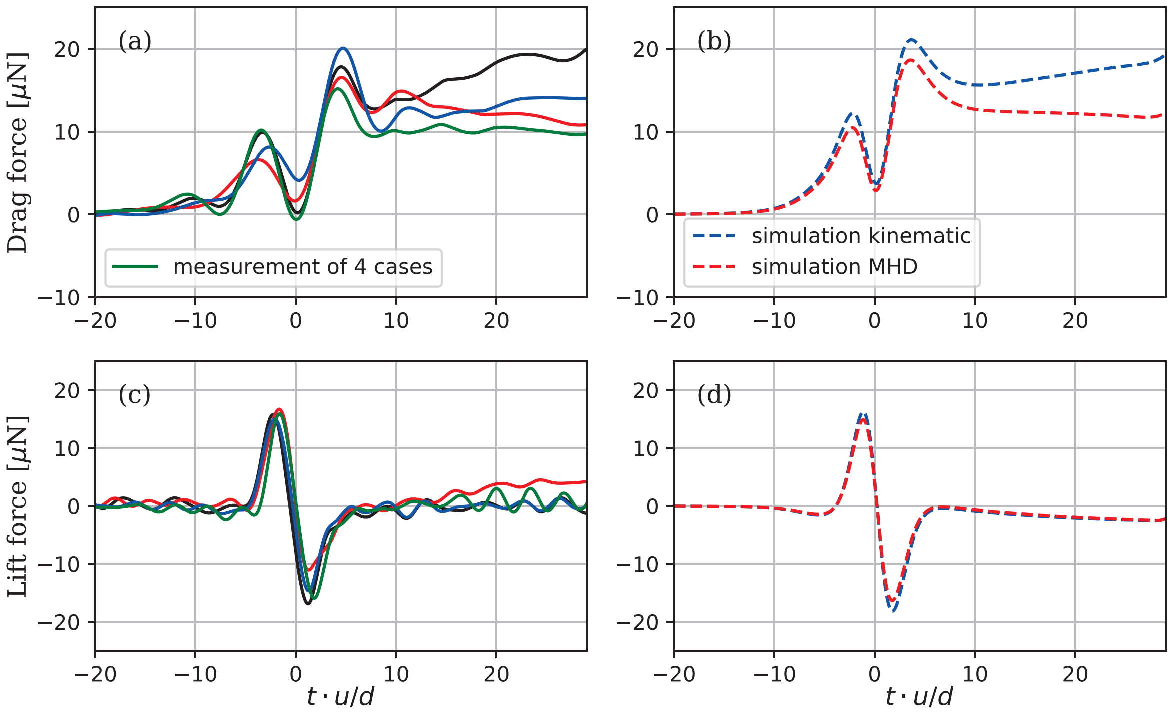

Figure 3.23: Lorentz forces in the experiment and MHD modeling at $Re = 2000$.

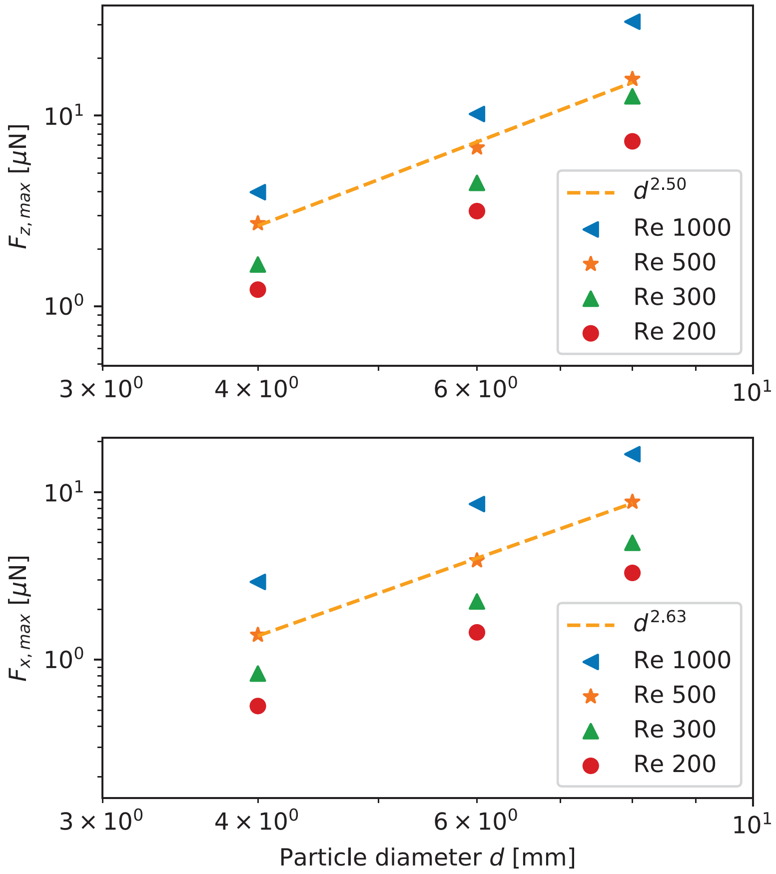

Figure 3.24: Effects of particle diameter d on drag and lift forces. (Other parameters are fixed at $L_1 = 9; L_3 = 10; L_4 = 12$ mm.)

about $L_4 \sim 18$mm. Considering the volume ratio

$$\frac{V_{magnet}}{V_{particle}} = \frac{L_4^3}{\pi d^3/6} = 51.6,$$

the observation agrees with the results of solid body defects test by Weise et al. [140], in which they report that the efficient point to maximize the defect-response lies within $\frac{V_{magnet}}{V_{particle}} \in [33.7, 56]$. This optimal region is useful for future designs of LFV for particle detecting in liquid metal flows.

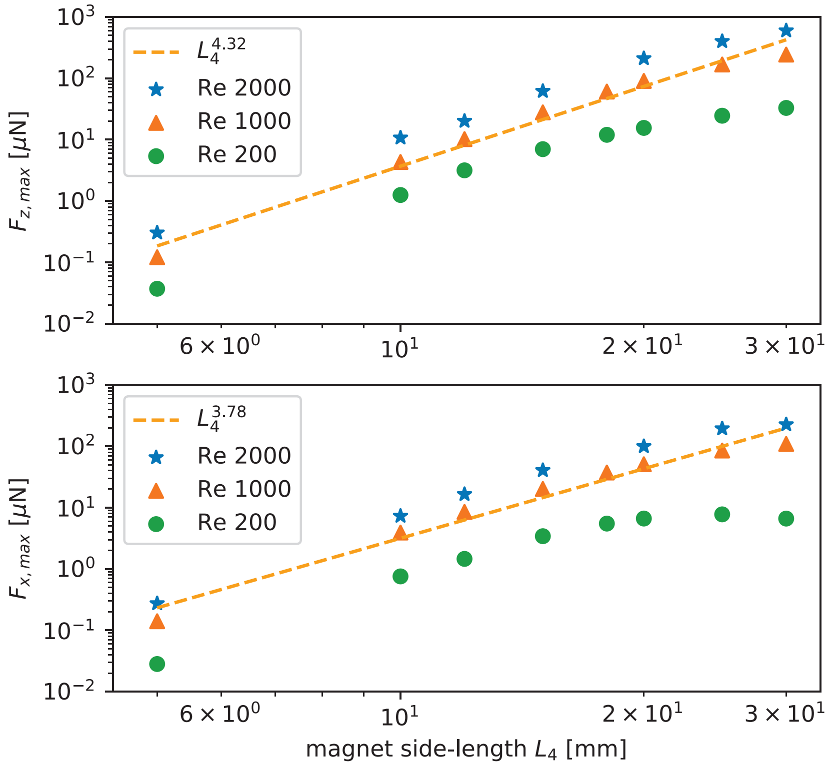

Figure 3.25: Effects of magnet size L_4 on drag and lift forces.
(Other parameters are fixed at $L_1 = 9; L_3 = 10; d = 6$ mm.)

The dependence of peaks of Lorentz forces on distance between the center of particle and wall L_3 is shown in figure 3.26. The peaks of drag force decrease with L_3 at about power of $L_3^{-3.86}$, while the lift force at about power of $L_3^{-1.14}$.

3.4.3 Summary

To shortly summarize, the kinematic modeling using analytical velocity field is valid only at $Re \leq 1$, however it is a straight-forward tool to estimate an upper-limit of Lorentz forces. The modeling reveals the mechanism of "double-peaks" and illustrates the distributions of

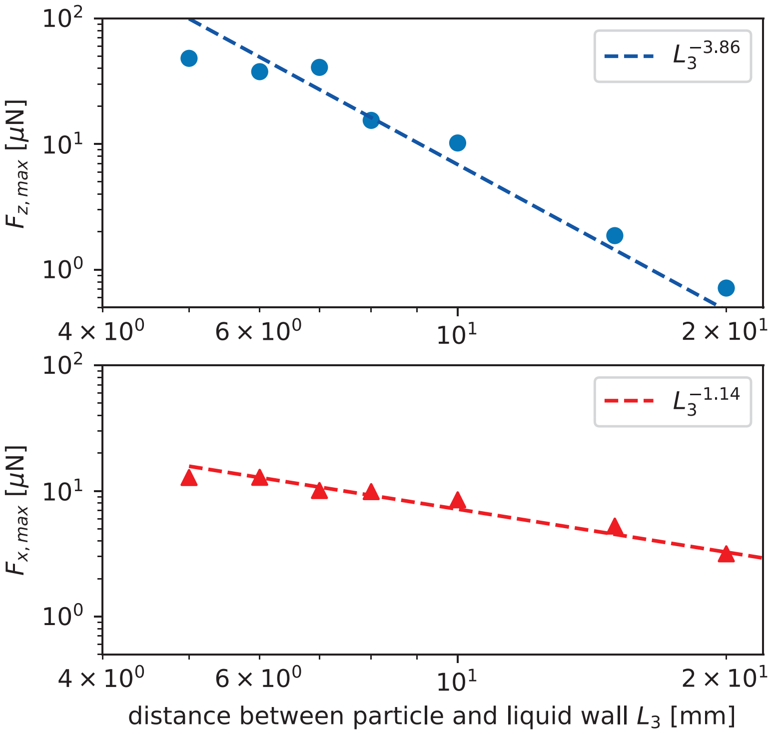

Figure 3.26: Effects of distance between particle and wall L_3 on drag and lift forces. (Other parameters are fixed at $L_1 = 9; d = 6; L_4 = 12$ mm.)

eddy currents density and Lorentz force density quantitatively. The MHD modeling shows promising agreement with measurements, which is used to investigate larger parameter spaces efficiently.

3.5 Predicting particle positions using neural network

The above results of various parameter influences open the broad applications for the inverse problem of using LFV to detect particle position, size and velocity. However using only the scaling may be insufficient, because the hydrodynamic perturbations are alway an uncertainty. One alternative option is applying machine-learning approach to treat the measurement results. In the present section we focus on the first test of predicting particle positions using so-called "Neural-network pattern recognition" (NPR) tool in commercial software MATLAB.

3.5.1 Training process

The procedure is shown in figures 3.27. The measurements from the velocity range of $Re > 1000$ are chosen, since the hydrodynamic instability is contained in the signals and thus, the performance of the network can be validated against it. As shown in figures 3.27, there are two options of the input for the training process, namely

- Raw data: LFV measurements of particle motions (diameter of 6 mm) in positions 1, 2, 3, 4 of the velocity $100, 150, 200$ mm/s from the measurements in section 3.3.
- Features of the data: some representing quantities calculated from the raw data. This approach is helpful to reduce training-computing-costs. Some examples of the feature of LFV signals in the time-domain are shown in table 3.1.

It should be noted that the raw data here are derived from the "continuous slow-mode" of IOFS as described in section 2.5 for convenience, because large data-set are needed for training the neural network. We use altogether raw data of 116 LFV measurements of particle moving in liquid metal. Each is a time-series of 60 seconds containing the Lorentz forces and a label of particle position.

As shown in figure 3.28, in the training-process 70% from the input are randomly chosen to train the net and the rest 30% are used to test it. One training itself takes $5 - 10$ iterations until the validation by selected cases are satisfied. It should be noted that here the amount of input measurement is not sufficiently huge. The results rely significantly on which 70% of the input are chosen to train, although randomly. Therefore an additional loop for repeating the training multiple times is used to test the effects of the choice of training input. We performed 1000 individual trainings, by which the choices of input are random and independent.

Table 3.1: Features of Lorentz force signals in the time-domain for training NPR.

Feature	Symbol	Definition	Range within 116 cases
mean	MV	$(\Sigma x_n)/N$	-5.9e-4 ~ 4.0e-4 [μN]
max	MAX	$max(data)$	-0.18 ~ 71.35 [μN]
variance	VAR	$\sqrt{[\Sigma(x_n - \text{MV})^2]/N}$	0.2 ~ 149.1 [μN]
peak-to-peak	PPV	$max(data) - min(data)$	3.7~ 73.5 [μN]
absolute amplitude	AA	$(\Sigma\|x_n\|)/N$	0.3 ~ 6.4 [μN]
root amplitude	RA	$[(\Sigma\|x_n\|)/N]^2$	0.1 ~ 41.1 [μN^2]
skewness	SKEW	$(\Sigma x_n^3)/N$	-15 ~ 8706 [μN^3]
	...	...	

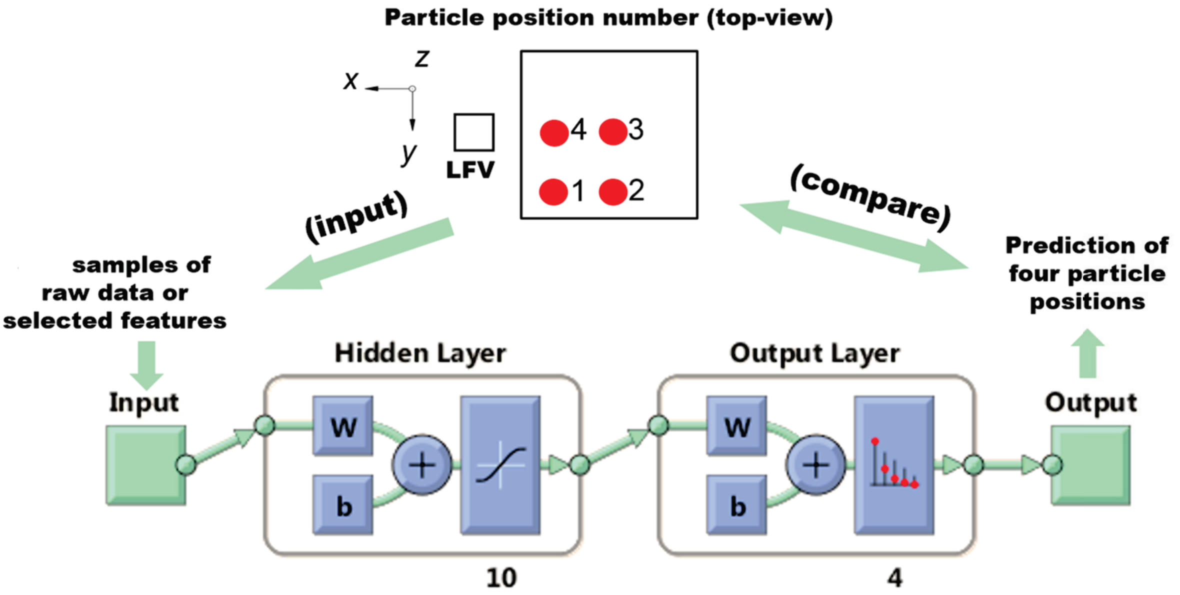

Figure 3.27: Schematic of the NPR training.

3.5.2 Result of one training

Regardless of solver performance, one of the most important aspects to quantify the net is the so-called "confusion matrix". One example of a training result is shown in figure 3.29. Within the four subfigures, the horizontal axis is the "correct" position as target, which is labeled manually for each sample. The vertical axis is the "output" of net as prediction. The upper two subfigures shows 100% correct predictions for all four positions in the training and validation phases. Then the left 30% of the input are used to test the net and there is 88.2% correct predictions as shown in the lower-left subfigure. In the test phase we observe that two samples of position 1 ("corner") and 2 ("side") are wrongly predicted as 3 ("middle"). They are more challenging for NPR possibly because the particle experiences strong wall-effects in such cases and is further to the LFV, by which the signal is weaker and more chaotic.

3.5.3 Statistics of multiple trainings

As described before, the prediction performance rely on which 70% of input are chosen to train the network. Therefore another test of 1000 individual trainings is performed, where each run has individual choice of random 70% of input data. We observe that over 950 runs have $>$ 90% successful prediction rate, which indicates that the NPR is robust on the choice of input in the current data space.

We tested another NPR training using the abstracted features of signals (e.g. in table 3.1) as input instead of the raw data. As shown in figure 3.30 upper, the successful prediction

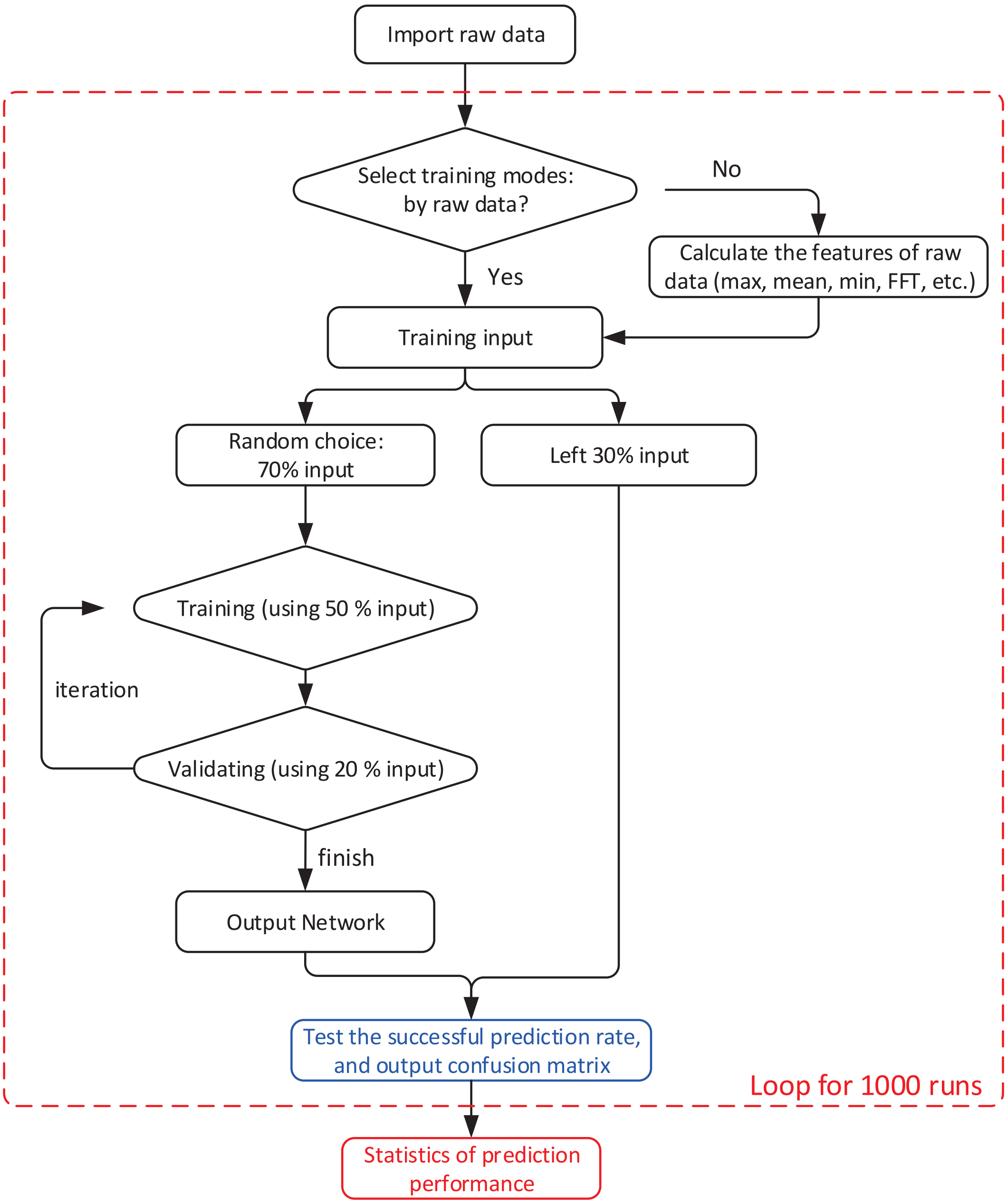

Figure 3.28: The procedure for NPR trainings (multiple trainings).

Training Confusion Matrix

Output Class

	1	2	3	4	
1	**23** 28.0%	**0** 0.0%	**0** 0.0%	**0** 0.0%	100% 0.0%
2	**0** 0.0%	**18** 22.0%	**0** 0.0%	**0** 0.0%	100% 0.0%
3	**0** 0.0%	**0** 0.0%	**22** 26.8%	**0** 0.0%	100% 0.0%
4	**0** 0.0%	**0** 0.0%	**0** 0.0%	**19** 23.2%	100% 0.0%
	100% 0.0%	100% 0.0%	100% 0.0%	100% 0.0%	**100%** **0.0%**

Target Class

Validation Confusion Matrix

Output Class

	1	2	3	4	
1	**4** 23.5%	**0** 0.0%	**0** 0.0%	**0** 0.0%	100% 0.0%
2	**0** 0.0%	**5** 29.4%	**0** 0.0%	**0** 0.0%	100% 0.0%
3	**0** 0.0%	**0** 0.0%	**5** 29.4%	**0** 0.0%	100% 0.0%
4	**0** 0.0%	**0** 0.0%	**0** 0.0%	**3** 17.6%	100% 0.0%
	100% 0.0%	100% 0.0%	100% 0.0%	100% 0.0%	**100%** **0.0%**

Target Class

Test Confusion Matrix

Output Class

	1	2	3	4	
1	**0** 0.0%	**0** 0.0%	**0** 0.0%	**0** 0.0%	NaN% NaN%
2	**0** 0.0%	**6** 35.3%	**0** 0.0%	**0** 0.0%	100% 0.0%
3	**1** 5.9%	**1** 5.9%	**3** 17.6%	**0** 0.0%	60.0% 40.0%
4	**0** 0.0%	**0** 0.0%	**0** 0.0%	**6** 35.3%	100% 0.0%
	0.0% 100%	85.7% 14.3%	100% 0.0%	100% 0.0%	**88.2%** **11.8%**

Target Class

All Confusion Matrix

Output Class

	1	2	3	4	
1	**27** 23.3%	**0** 0.0%	**0** 0.0%	**0** 0.0%	100% 0.0%
2	**0** 0.0%	**29** 25.0%	**0** 0.0%	**0** 0.0%	100% 0.0%
3	**1** 0.9%	**1** 0.9%	**30** 25.9%	**0** 0.0%	93.8% 6.3%
4	**0** 0.0%	**0** 0.0%	**0** 0.0%	**28** 24.1%	100% 0.0%
	96.4% 3.6%	96.7% 3.3%	100% 0.0%	100% 0.0%	**98.3%** **1.7%**

Target Class

Figure 3.29: Example of the confusion matrix for one trained network.
(The target class represent the correct four positions of particles; the output class is the predicted one from network).

rate of 1000 runs using selected features of data are also good, generally $> 80\%$, however lower than that of the raw data. The decrease compared to the case of raw data is reasonable, because the network "loses" some information of the signals using only features in stead of raw data, which leads to poorer performance to predict the particle positions. The results reflect the advantage of NPR model in terms of "getting the most info from data".

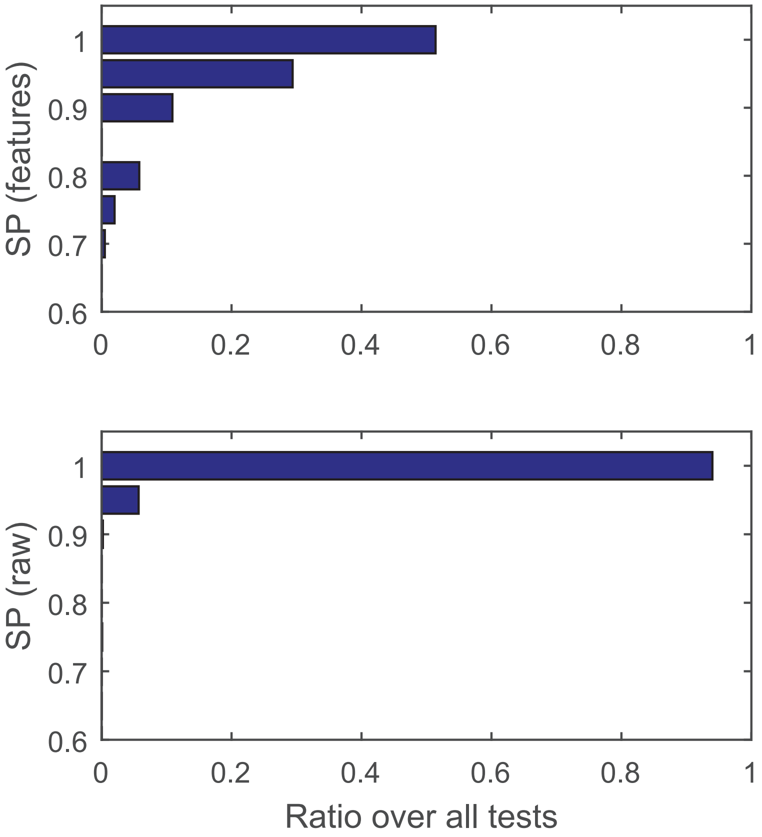

Figure 3.30: The statistics of prediction performance over 1000 trained networks. ($SP(features)$ represents the successful prediction rates of particle positions from trainings by selected features of signals; $SP(raw)$ represents that by raw data.)

3.5.4 Summary

To shortly summarize, the present section shows the first test of predicting particle positions using NPR based on LFV signals. The method is robust and its prediction performance is promising. It opens the gate to various applications of treating engineering LFV results with machine-learning algorithms. More work and tests in this direction are motivated.

3.6 Conclusion

In this chapter two experiments of detecting particle motions in liquid metal using LFV are presented. In the first test of particle "free-rising" in a thin tube, the transient response of Lorentz force for particle passing through are successfully recorded despite the simple configuration. It proves the concept of LFV for the application of particle detection. The Lorentz force signals vary significantly, possibly caused by the strong wall effects or the limitation of default data-processing of IOFS.

The extended experiment of controllable particle motion in liquid metal is therefore motivated and conducted. Here the liquid-container is larger to exclude the wall-effects, and the particle velocity is controlled to evaluate different flow regimes. A customized data-processing is introduced to de-noise the LFV signals. The results are promising and show good reproducibility. When the particle moves near the wall, the "double peak" pattern is observed in all flow regimes.

The corresponding numerical modelings show good agreement with the measurements. We investigate the dependence of the peak value of Lorentz force on the particle diameter, magnet size, or distance between particle and wall, respectively. Such effects form the basis of LFV for the application of particle detection.

The hydrodynamic instabilities in the experiment are always an issue, which introduces uncertainties to the scalings of LFV for the applications of liquid metal two-phase flow. Therefore a machine-learning approach is tested to support the data analysis. The Neural-network Pattern Recognition is the algorithm of choice, which is trained to distinguish the Lorentz forces from four different particle positions. Over multiple trainings, the NPR shows the robust successful prediction of particle positions.

Chapter 4

Bubble rising in liquid metal

In this chapter we focus on the problem of bubble rising in liquid metal initially at rest. The results of particle problem in the previous chapter 3 provide a basis for the analysis. Here one difference compared to the particle case is that the bubble is deformable, and the shape of bubble may be influenced by the localized magnetic field and thus introduces additional perturbations on LFV. Another difference is that the bubble follows a "zig-zag" route, therefore the distance between the bubble and LFV may differ for each signal. We start with the experiment of bubble rising in a thin tube of liquid metal initially at rest (section 4.1), where the geometry is identical to the previous particle measurement in a thin tube (section 3.2). Motivated by the test of particle motion in a large vessel (in section 3.3) to exclude the wall effects, a corresponding experiment of bubble rising in the large vessel is performed and described in section 4.2. The qualitative agreement with the numerical modeling is presented in section 4.3. Two additional experiments of LFV for bubble rising at high temperature and under ambient magnetic field are described in sections 4.4 and 4.5, respectively.

Part of the results are taken from publications Karcher et al. [50], Lyu et al. [60], Lyu and Karcher [61], Lyu et al. [63], Tran et al. [127], and Tran et al. [128] with some modifications.

4.1 Experiment of bubble rising in a thin tube

In a first test we investigated the transient response of drag force F_z to a simple arrangement of argon bubbles injected into liquid GaInSn in a thin tube initially at rest. Single bubbles are generated one after another, where time gaps between each injection is kept long ($>$ 30 s) and there is no influence between individual bubbles. Thus we exclude the effects of a turbulent liquid metal basic flow and bubble interactions. The recorded Lorentz force is only due to the melt flow induced by the displacement effect of a rising bubble.

4.1.1 Experimental setup

The experimental setup is shown in figure 4.1, which consists of four parts, i.e. the argon injecting system, the vertical fluid tube, LFV, and an additional measuring vessel for gas volume. The experiments were performed in a cylindrical glass tube with an inner diameter of 20 mm and wall thickness of 3 mm. The tube was filled up to the height of 300 mm with alloy GaInSn as working fluid. Pressurized argon is injected into the bottom of the tube via a glass nozzle with outer-diameter 1 mm. Bubbles are generated one after another, and time gaps between each bubble are 20 − 30 seconds. This is the so-called "single bubble condition”. We can assume the liquid is at rest before the injection of the next bubble and thus, the initial conditions for each bubble are the same. On the top of the tube, a plug with silicon tube inside serves to capture argon in the additional measuring vessel filled with water. By that, the total volume of argon gas injected during one measurement can be measured.

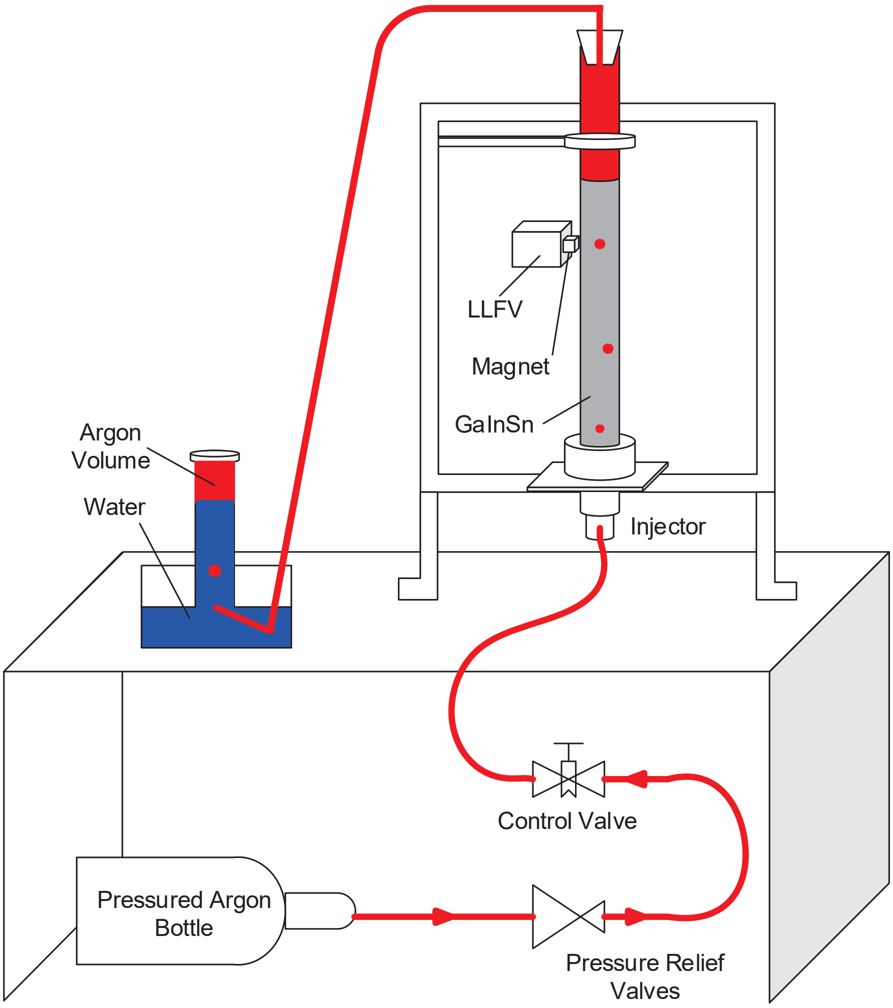

Figure 4.1: Schematic of the experiment of bubble rising in a thin tube.

4.1.2 Results

The bubble rising process is illustrated in figure 4.2. Firstly, a small bubble appears on the nozzle top, whose volume starts to grow. Correspondingly, the top-surface of liquid rises. When the buoyancy force on the bubble becomes larger than other resistant forces (surface tension force), the bubble detaches from the nozzle (see figure 4.2a). Bubble diameters are influenced by the nozzle diameter, the argon pressure, the wetting properties of the liquid to the nozzle material, the surface tension between the gas and liquid, and the density difference [150]. Bubbles rise in "zig-zag" route in the tube because of nonlinearity of the hydrodynamic equations and wall effects [32, 153]. Fluctuating forces are detected by LFV when bubbles rise through the near-magnet region (see figure 4.2b). The distances between bubble and magnet vary randomly. When the bubbles reach the top the liquid top-surface drops down again.

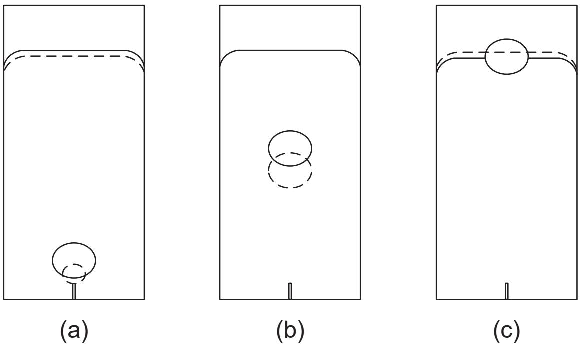

Figure 4.2: Schematic of the bubble-rising-process.

The travelling time for bubbles from bottom to top is recorded by high-speed-camera above the free surface. The starting time is defined when the free-surface rises, and the finishing time is defined as when the bubble appears on the top. The averaged travelling time of bubbles through GaInSn is about 1.39 seconds so that the average vertical velocity of bubbles is $u_0 = 0.22$ m/s, which agrees well with Fröhlich et al. [32] and J. Zhang et al. [155], by which they investigated bubbles rising in a liquid metal domain by direct numerical simulation. Therefore, the Reynolds number Re can be calculated as follows

$$Re = \frac{u_0 d \rho}{\mu} = 4463, \tag{4.1}$$

where $u_0 = 0.22$ m/s - mean velocity of bubble; $d = 7.5$ mm - diameter of bubble. A turbulent flow occurs during bubble rising process because $Re > 4000$. Liquid flows are unsteady and maybe different for each bubble [32]. For Hartmann number Ha we obtain

$$Ha = B_0 D_i \sqrt{\frac{\sigma}{\mu}} = 36, \tag{4.2}$$

where $B_0 = 47$ mT - magnetic flux density at middle of tube; $D_i = 20$ mm - inner diameter of tube. This value demonstrates that in the present study Lorentz forces dominate friction effects. As expected, the magnetic Reynolds number Re_m is small,

$$Re_m = \mu_0 \sigma u_0 D_i = 0.019. \tag{4.3}$$

This result shows that the induced magnetic field remains small. Finally, for interaction parameter N we obtain

$$N = \frac{\sigma B_0^2 D_i}{\rho u_0} = Ha^2/Re = 0.29. \tag{4.4}$$

In the following we focus on the transient response of LFV to bubble rising in liquid metal. The LFV sensor detects fluid motion in the region close to the magnet. The Lorentz force signals fluctuate strongly when bubbles move through the test region, which are shown in figure 4.3. The small peaks before each main signal result from the stage of bubble growth before detachment from nozzle. Therefore global up-shift of liquid volume is observed. These small peaks correspond to a constant Lorentz force of about $+10\mu$N, because the volume of each bubble is similar under single bubble condition. Additionally, these small peaks indicate the bubble detachment-time. As can be seen, the peaks of Lorentz force signals are quite different, varying from -120 μN to +80 μN. We see that the downward F_z occur more often than upward forces.

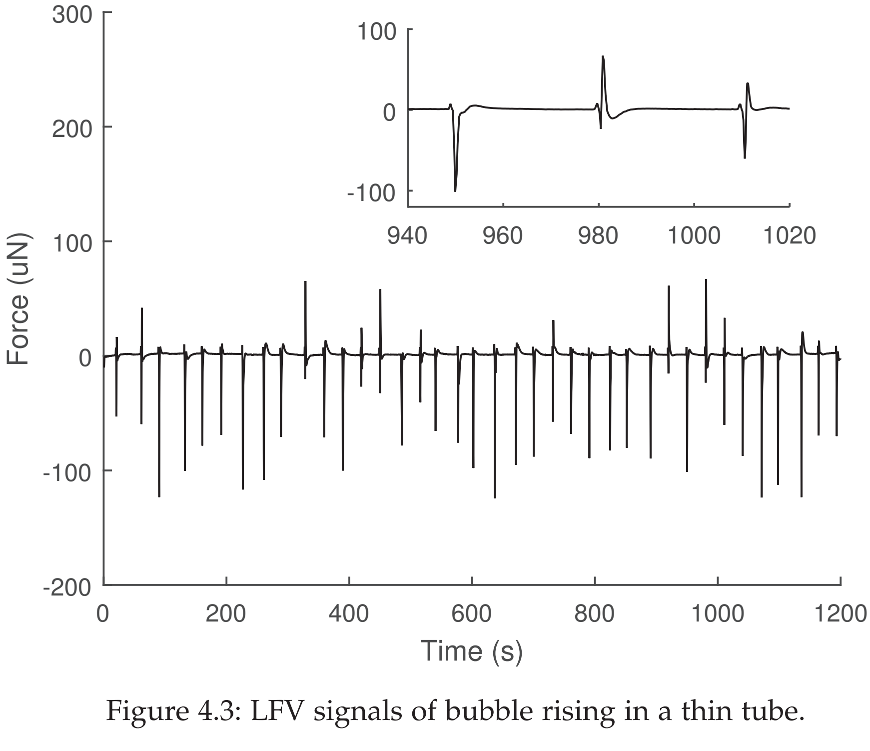

Figure 4.3: LFV signals of bubble rising in a thin tube.

To better describe three representative cases are plotted together in figure 4.4, where the time of detachment of bubbles are all set to $t = 2.3$ s. In the beginning of main peak zones, signals all start with flow-induced downward forces. In a later stage, bubble A mainly triggers upward force, and bubble C mainly downward forces, while bubble B triggers both upward and downward forces. The difference between bubble A, B and C in figure 4.4 can be mainly attributed to effects of local liquid flow. For that a schematic of liquid flow is shown in figure 4.5 based on other studies [32, 150, 155]. The magnetic flux densities decrease significantly when we move further away from the permanent magnet, therefore zone 4 has only a small influence on the measured Lorentz force and Lorentz forces are mainly influenced by liquid flow in zone 1, 2 and 3. Liquid flow in zone 1 move up and that in zone 2 move down due to the displacement induced by rising bubble. Unsteady bubble wake structures and vortices occur in zone 3. As discussed before, bubbles rise in a "zig-zag" route and therefore bubble positions are different for each signal. When bubble is close to the left wall, zone 2 is suppressed and zone 1 and 3 dominate Lorentz force signal (probably bubble A). When the bubble is far away from the left wall, zone 2 is most effective (probably bubble C). When the bubble in near the middle of the tube, zone 1, 2 and 3 are all important, and it leads to complex combinations of all these effects (probably bubble B). Moreover, the rising bubbles generate a tail zone before the signal eventually decays back to zero.

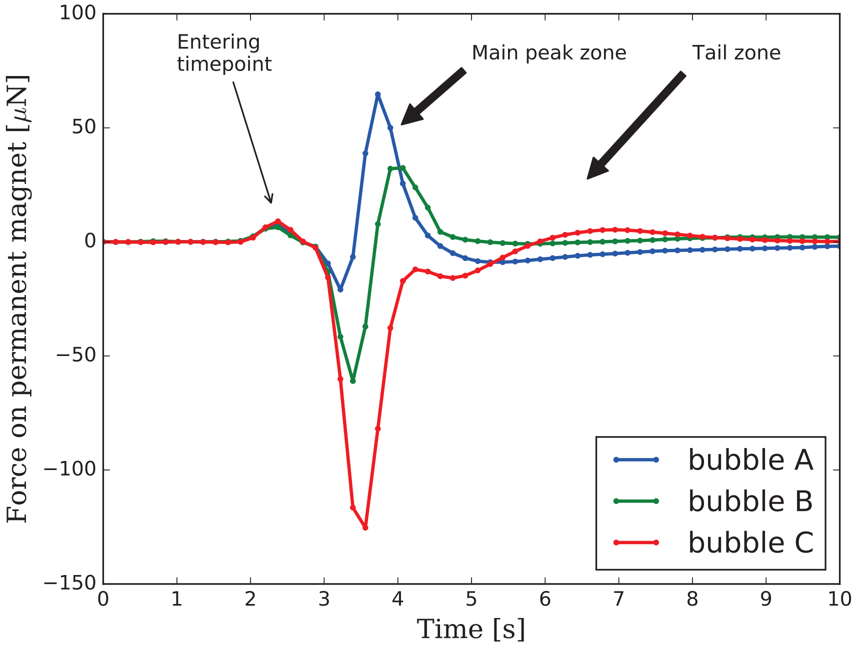

Figure 4.4: Example of three LFV signals of bubble rising in a thin tube.

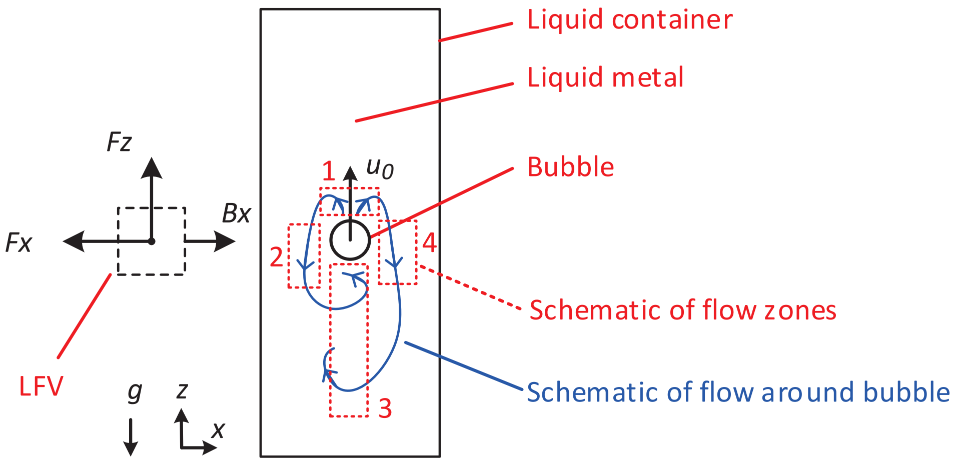

Figure 4.5: Schematic of the flow around bubbles.

4.1.3 Summary

Lorentz force signals for bubbles rising in liquid metal are measurable. They fluctuate strongly when bubbles move through the test region. Different shapes of Lorentz force signals were observed. This is caused by local fluid flow effects. The routes of bubbles rising determine the bubble positions in test region, which are important for evaluating Lorentz force. However they are different for each bubble. The wall-effect plays an important role since the tube is thin.

4.2 Experiment of bubble rising in a large vessel

In the previous experiment in section 4.1, there is very limited space for the displacement flow to develop and therefore strong wall effects on the bubble behavior. The present experiment aims to exclude the wall effects by introducing a larger liquid-container. The vessel is identical to that of the extended particle experiment in section 3.3, except that the wall thickness is less. Thus the LFV can be installed nearer to the fluid and higher LFV signals are obtained.

4.2.1 Experimental setup

A schematic and two photos of the bubble rising setup are shown in figures 4.6 and 4.7, respectively. The dimensions of the experimental setup for bubble rising in a large vessel are identical to that of the controllable particle motion described in section 3.3 (see also figure 3.5 for reference). The plastic vessel (wall-thickness 4 mm) has the inner volume of $60 \times 60 \times 350$ mm^3, which is filled with liquid alloy GaInSn as working fluids. A syringe pump is introducing argon into the liquid via the silicon tube through the top of vessel and nozzle installed at the bottom of liquid domain. The silicon tube is far from test region and attached on the other side wall, therefore its effect can be neglected. The nozzle is made of stainless steel and installed on the bottom by the adapter made of paper. Its outer-diameter is 1 mm and points vertically up. The adapter can set the distance between the nozzle and wall at 10 or 30 mm. The averaged bubble volume is calculated by the flowrate of syringe pump and counts of bubbles. Assuming the bubble are spherical and have constant volume, we receive the bubble diameter of $d = 7.1$ mm, which is very similar to case of bubbles rising in a thin tube described in section 4.1.2.

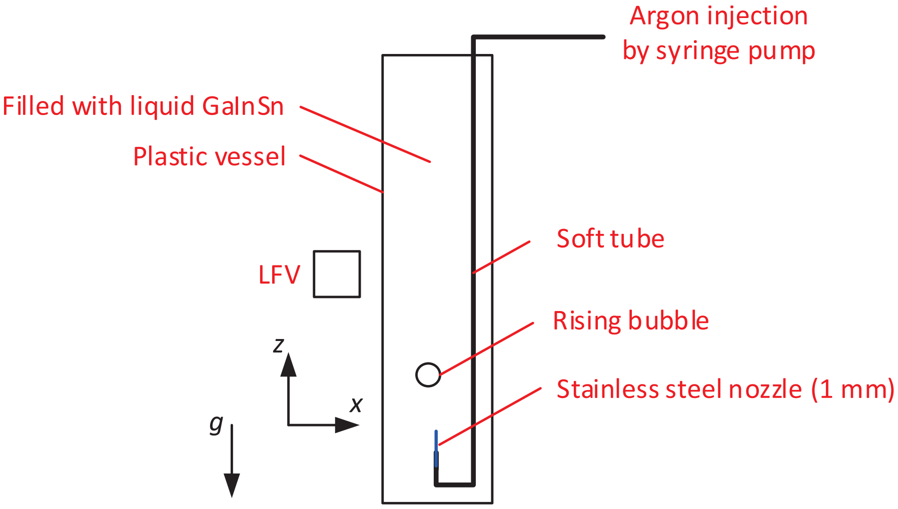

Figure 4.6: Schematic of the experiment of bubble rising in GaInSn.

4.2.2 Results

Firstly the nozzle is set at 10 mm to the wall. The distance between the magnet surface and the liquid wall is 9 mm. Four repeated measurements of drag forces are shown in figure 4.8. As bubbles rise on a "zig-zag" route, the zero position is unknown. Therefore the signals are coordinated manually by setting the rising edge of signals at 1 s. We observe that the drag forces are all upward however vary in amplitudes. The "double-peaks" in the drag force are obtained sometimes, which is probably caused by the "zig-zag" of bubbles. When one bubble is a bit further away, the effects of "double-peaks" becomes weaker as described in section 3.3.3 and may eventually disappear. Comparing to the bubbles in a thin tube, the small upward peaks before the main signals are not obtained, because the vessel is much larger and the global shift due to one bubble volume is negligible. Comparing to the particle

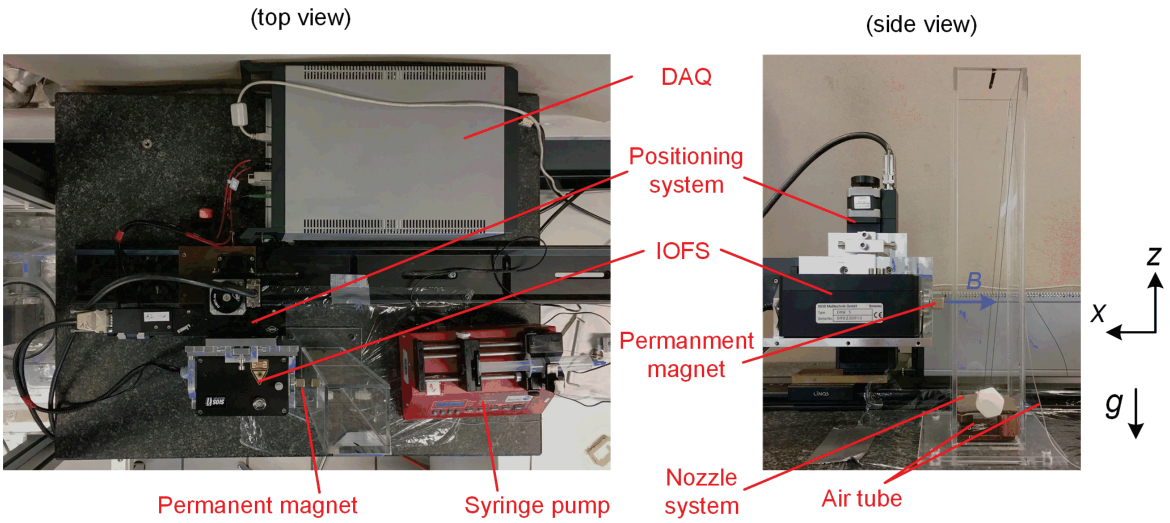

Figure 4.7: Photo of the experiment of bubble rising in GaInSn.

cases described in 3.3.3,the bubble signals have more variations.

Four repeated cases of lift force measurement are shown in figure 4.9. Comparing to the previous particle case, the lift force has several zeros as well. However it fluctuates much more and is not reproducible. Additionally signals have longer tails than in the particle case, which indicates that the local displacement flow is stronger.

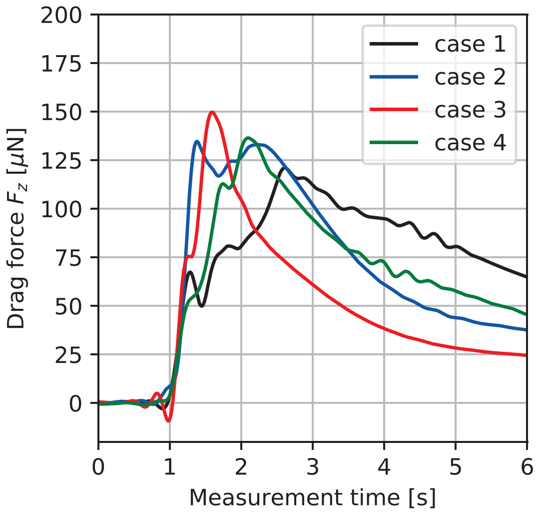

Figure 4.8: Drag forces for bubble released near to wall of 10mm.

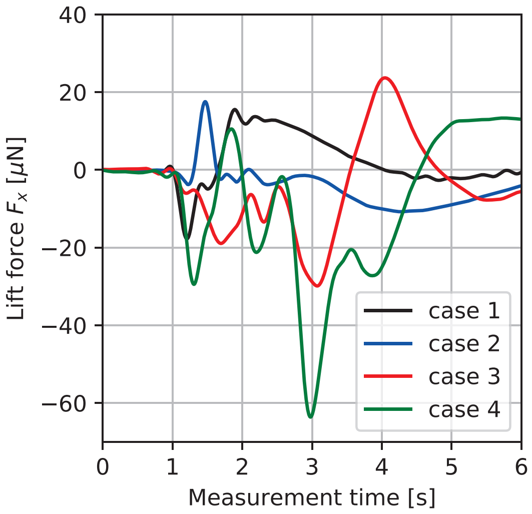

Figure 4.9: Lift forces for bubble released near to wall of 10mm.

The second test is the nozzle at 30 mm in parallel to the wall. Eight repeated measurements of drag- and lift force are shown in figures 4.10 and 4.11, respectively. They are very similar to that of particle case described in section 3.3.3. It indicates that when the bubble is far from the wall, its effects of deformation and "zig-zag" on LFV becomes insignificant and is more similar to the particle cases.

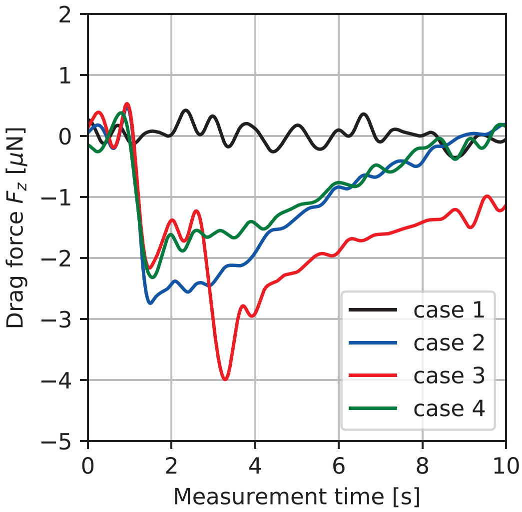

Figure 4.10: Drag forces for bubble released far from the wall of 30mm.

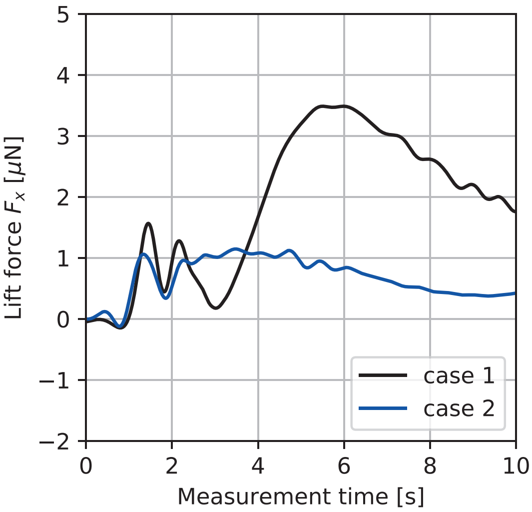

Figure 4.11: Lift forces for bubble released far from the wall of 30mm.

The third test is again bubble near the wall (nozzle 10 mm parallel to the wall), however LFV is at 5 mm to the wall. The interaction between LFV and bubble becomes much stronger and the results are shown in figures 4.12 and 4.13, respectively. The high peaks of drag forces in the range of $200 - 500$ μN are observed. The lift force has much more fluctuations comparing to the case of LFV at 9 mm. In such cases of LFV close to the wall and bubble near the wall, it is expected that the patterns of LFV signals differ from particle case. As the interaction parameter here is high $(N > 1)$, the interaction between bubble and LFV is strong and the bubble deformation could be large.

4.2.3 Summary

The LFV signals in the experiments of bubble rising in liquid metal in large vessel have poor reproducibility. They have similar patterns to the previous particle problem (e.g. double-peaks, zero-crossing-pulses) however more fluctuations. When LFV is installed very close to the wall, the MHD effect becomes so strong that the effects of bubble deformations may become significant. The patterns of signals are rather different from the particle case.

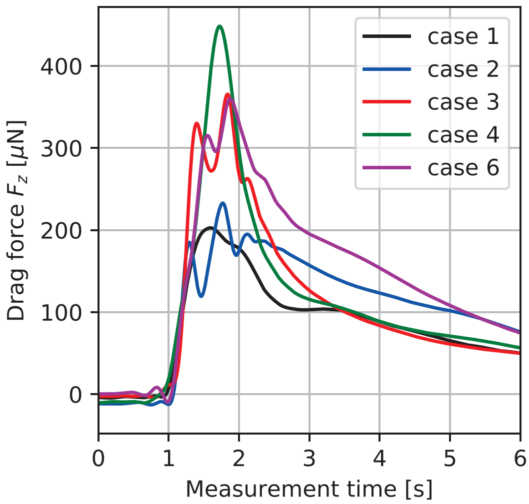

Figure 4.12: Drag forces for LFV close to the liquid of 5 mm (bubble released at 10 mm to the wall).

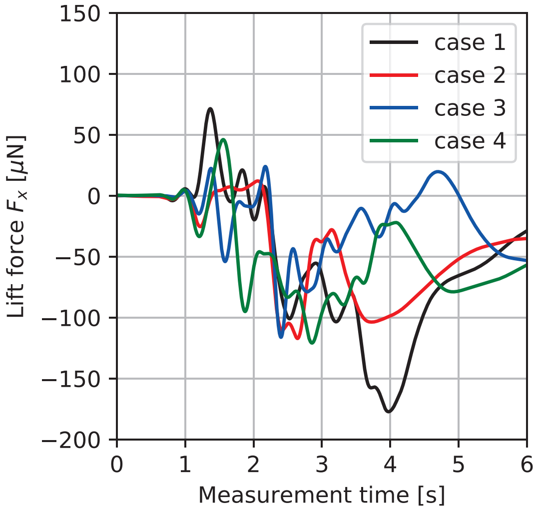

Figure 4.13: Lift forces for LFV close to the liquid of 5 mm (bubble released at 10 mm to the wall).

4.3 Comparison with numerical model

The following analysis is from the numerical modeling done by my colleague N. Tran using ANSYS Fluent. The aim is to develop a numerical tool to simulate the bubble rising process and compare the Lorentz force to measurements. The liquid domain in the extended experiment of $60 \times 60 \times 400$ mm^3 (described in section 4.2) is unfortunately too expensive to compute. Therefore for convenience we focus on modeling the case of bubble rising in a small cuboid of $27.6 \times 27.6 \times 220$ mm^3 filled with alloy GaInSn. The geometry of the model is shown in figure 4.14. The liquid is initially at rest and the bubble of diameter 4.6 mm is imposed at the bottom at different locations, respectively. The resulting bubble terminal velocity is shown in figure 4.15, which agrees well with the study by C. Zhang et al. [150].

The resulting Lorentz forces are shown in figure 4.16. We see the Lorentz force fluctuates from -80 μN to $+80$ μN, which agrees qualitatively well with the measurement results in section 4.1.2 (see e.g. figure 4.3). For simulation details please refer to Tran et al. [127].

4.4 Experiment of bubble rising in liquid tin at high temperature

The motivation of the present experiment of bubble rising in liquid tin is to validate the capability of LFV for bubble detection at high temperature, which is important for industrial applications. A schematic of the experimental setup is shown in figure 4.17. The test section

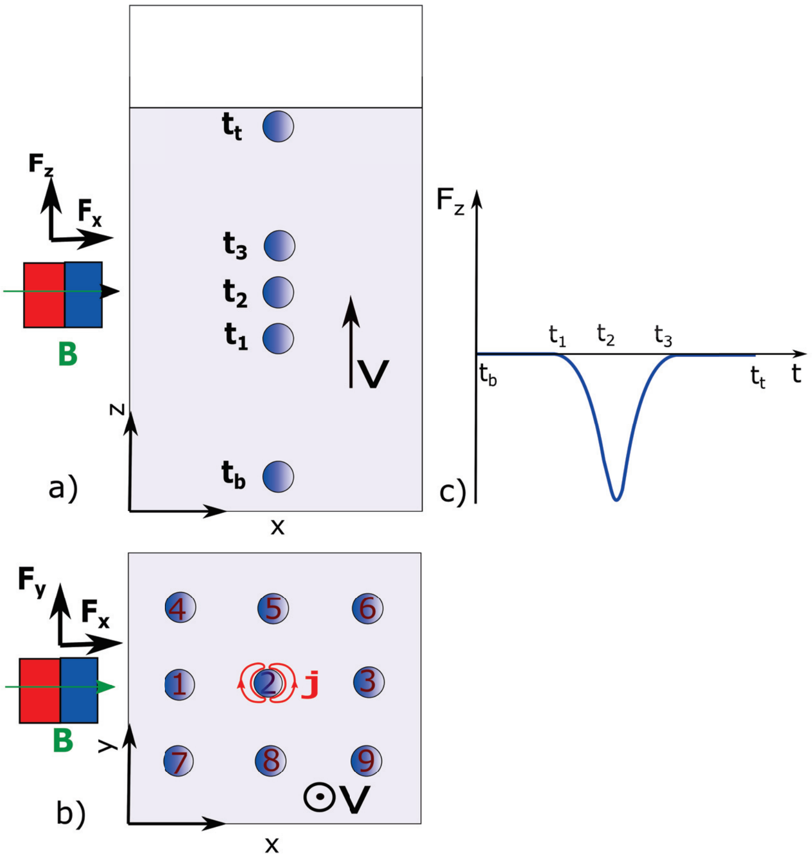

Figure 4.14: Schematic of MHD modeling for bubble rising. (a) the side view. (b) the top view. (c) drag force (© N. Tran).

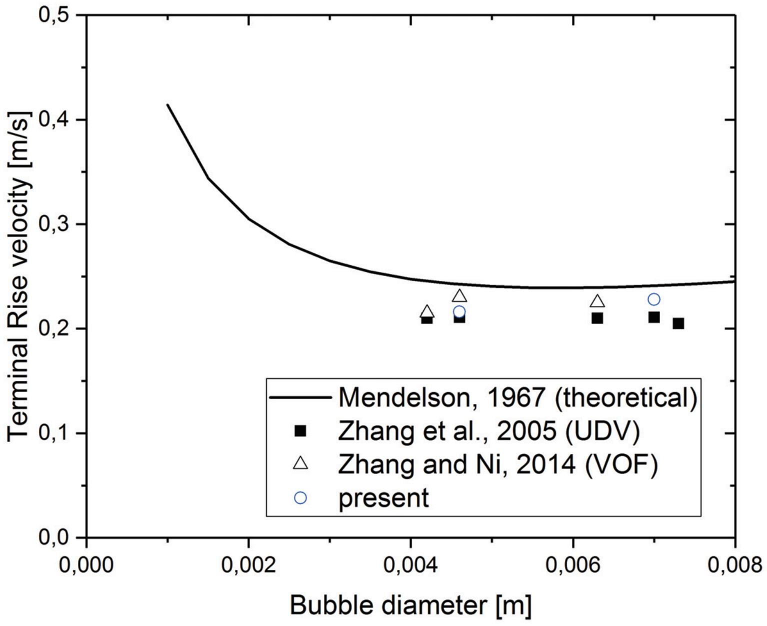

Figure 4.15: Comparison of bubble terminal velocity versus diameter in experiment and modelings (© N. Tran).

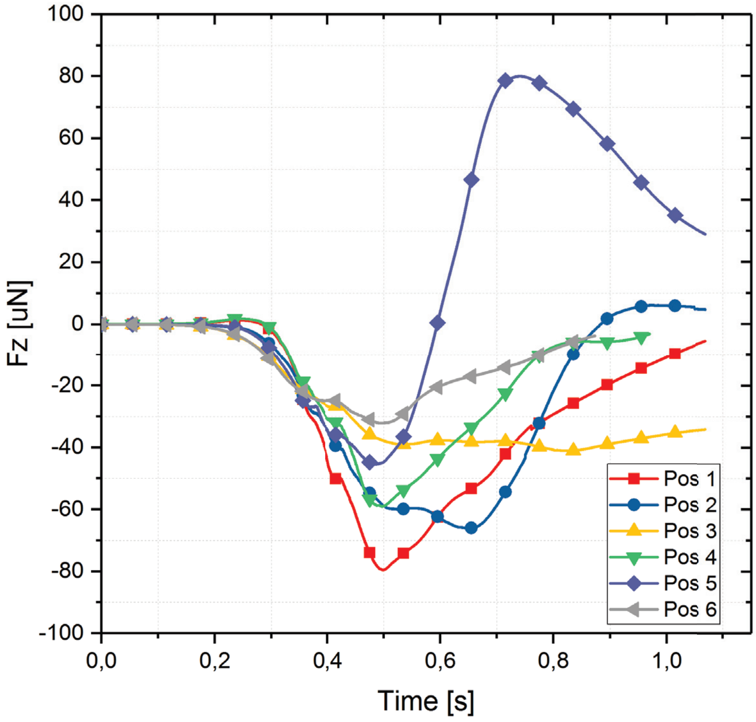

Figure 4.16: Lorentz forces in MHD modeling for bubble rising in a thin tube (© N.Tran).

is a stainless steel tube of the inner volume of 20 × 20 × 350 mm^3, and the wall thickness is 2 mm. Similar as before, the LFV consists of the IOFS and a cubic magnet of 12 mm side-length. The distance between the magnet surface and the liquid wall is set at 50 mm to protect IOFS from the heat. The argon is injected through a nozzle of 1 mm diameter from the bottom of the liquid domain. The bubbles are 2 mm in diameter approximately.

The tube is initially filled with solid tin. The first test is shown in figure 4.18 left, by which the tin is heated by a customized heater of max. 2 kW. The heater is controlled by electronics and maintains the temperature at 300 °C. After all the tin is melted, we observe nice "single-bubbles" by visualization on the top surface, however the inducting heater generates strong noise and the LFV signals are not valid. If we switch-off the heater, the noise disappears. However LFV in this case was too far from the liquid due to the thickness of the heater and no signals were observed. Another test was that we switch-off the heater, removed it quickly and installed the LFV near the liquid. The heat-loss was so strong that the tin solidifies in seconds and no bubbles could be generated.

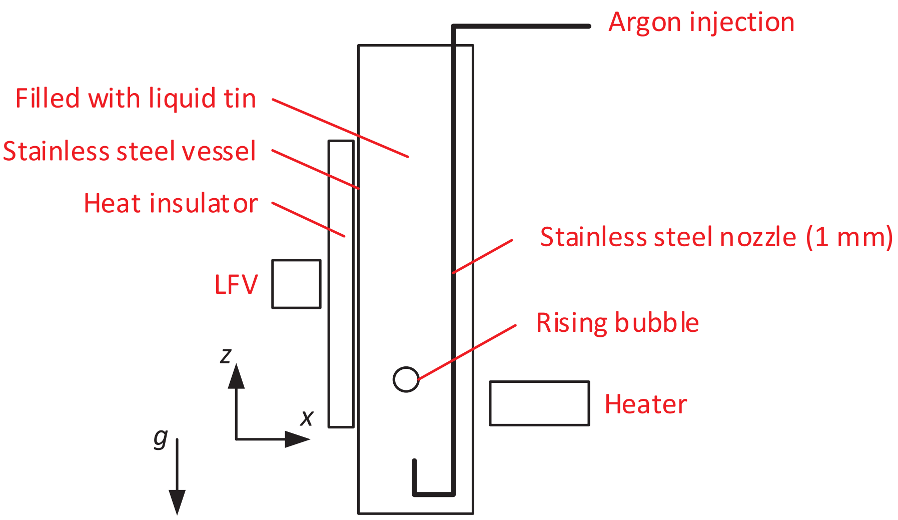

Figure 4.17: Schematic of the experiment of bubble rising in liquid tin.

The alternative test is heating tin by flames directly (see figure 4.18 right). The tin below the height of heating solidifies due to natural air cooling, and the tin at the heating-height and above remains liquid. The signals are still low and contain strong noise because:

- The distance between liquid tin and LFV are larger comparing to GaInSn case, however this is neccesary to protect LFV.
- The size of the bubble are much smaller comparing to the GaInSn case even with the same nozzle, due to the change of temperature and surface tension.
- The electrical conductivity of liquid tin is lower that that of GaInSn.

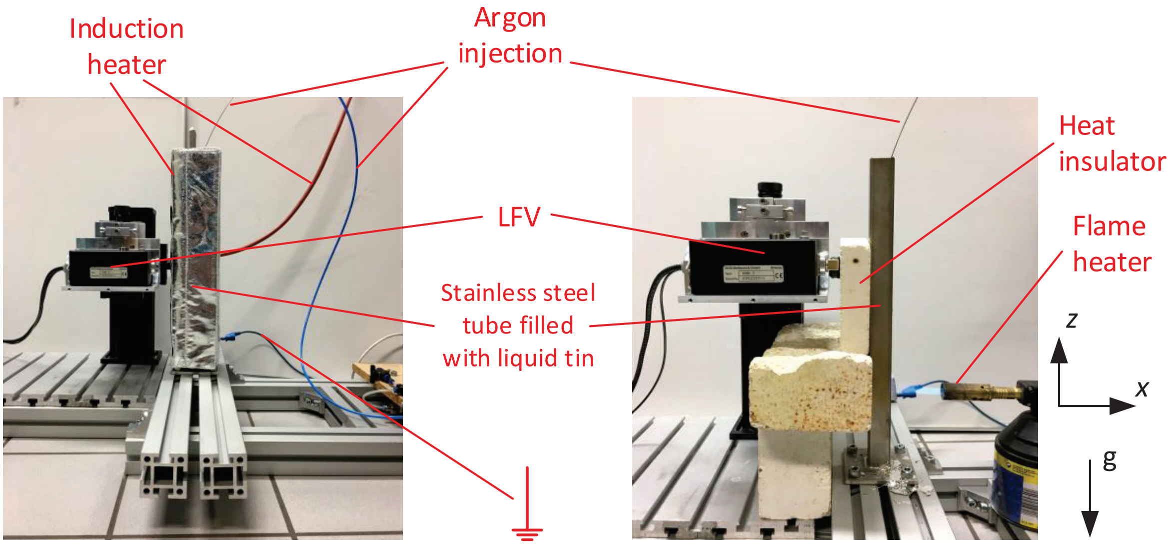

Figure 4.18: Photo of the experiment of bubble rising in liquid tin.

- The heating of flame is not homogeneous although it melts the tin, which introduces temperature noise to the system.

Nevertheless some of the bubbles are successfully captured by LFV. Three selected Lorentz force signals are shown in figure 4.19 as example. We observe the drag forces F_z in the range of ± 10 μN. The forces fluctuates significantly and the patterns of them are various simply because there are too many degrees of freedom in the experiment, namely the temperature uncertainty and bubble positions.

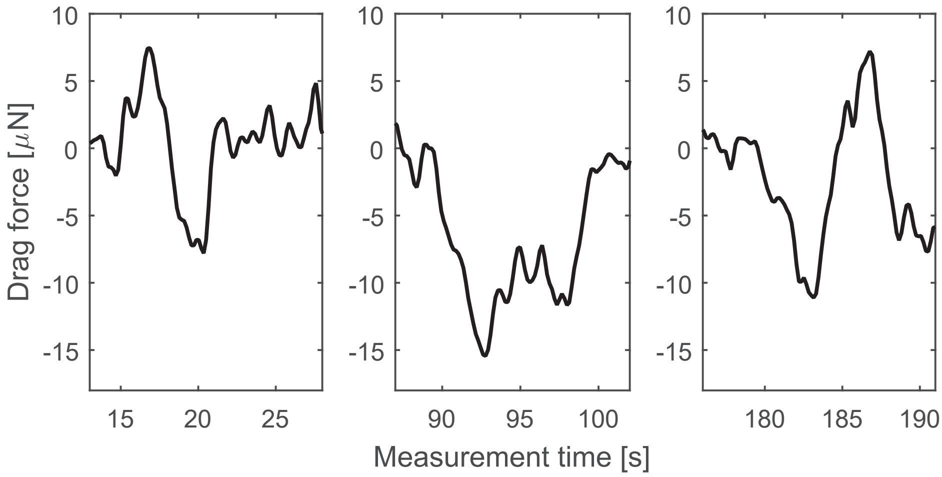

Figure 4.19: Three examples of LFV measurements for bubble rising in liquid tin.

To shortly summarize, although there is uncertainty of the experiment, they show the possibility that LFV might be applicable for liquid metal two-phase flow at high temperature. The present work serves as preliminary test of LFV in high-temperature two-phase flow applications, and it shows that the signals have more complex patterns comparing to the case of GaInSn at room temperature. There is huge potential to improve the experimental configuration, however they are not included in the present work due to limited time.

4.5 Experiment of LFV for bubble rising under ambient magnetic field

The idea of LFV for bubble rising in GaInSn under horizontal ambient magnetic field is motivated by the discussion with Prof. Xiaodong Wang from University of Chinese Academy of Sciences (UCAS), Beijing, China. It aims to test the capability of LFV in the applications of liquid metal two-phase flow under ambient magnetic field. The experimental test was supported by Prof. Wang and performed during my stay at UCAS. The facility of a horizontal electromagnet in his group was used.

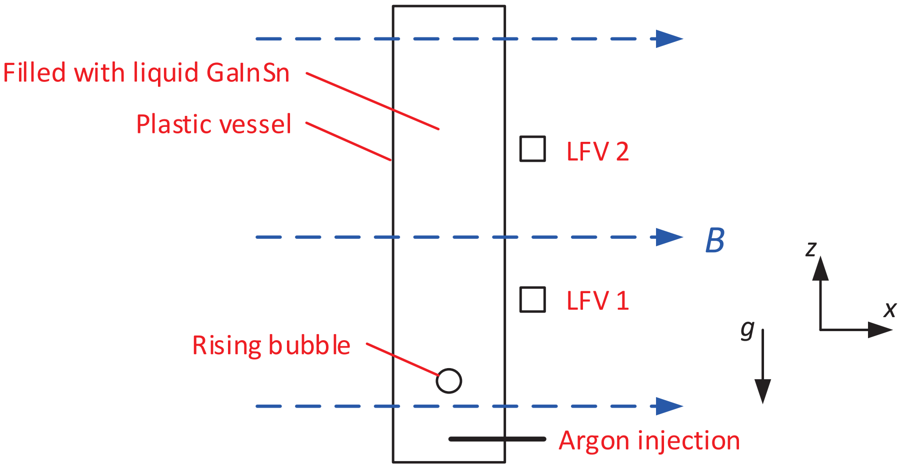

Figure 4.20: Schematic of the experiment of bubble rising under ambient magnetic field.

The schematic and photo of bubble rising setup is shown in figures 4.20 and 4.21 left. The argon gas is injected into a thin tube (inner diameter 20 mm, height 400 mm, wall-thickness 5 mm) of GaInSn by syringe pump via a plastic nozzle (outer-diameter 1 mm). The averaged bubble diameter is 7 mm, which is derived from the flowrate and bubble counts. Two commercial force sensors are configured as LFVs to check the capability of different measurement ranges, and also to validate their behavior under ambient magnetic field:

- LFV 1, max 1 N, with 10 mm cubic magnet.
  (test at $B = 1$ T, 6 mm to liquid, noise ~ 0.5 mN, $F_{z,max} \sim 3$ mN)
- LFV 2, max 0.1 N, with 5 mm cubic magnet.
  (test at $B = 1$ T, 6 mm to liquid, noise ~ 0.1 mN, $F_{z,max} \sim 0.4$ mN)

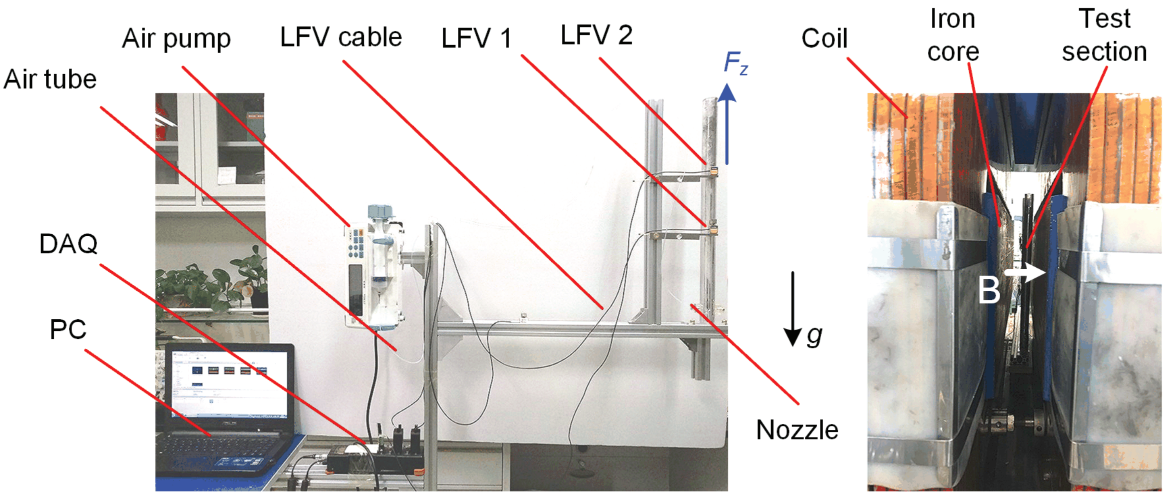

Figure 4.21: Photo of the experiment of bubble rising under ambient magnetic field.

The height from bottom to LFV 1, from LFV 1 to LFV 2 and from LFV 2 to liquid top are 100, 150, 100 mm, respectively. Part of the electromagnet is shown in figure 4.21 right. The test gap is 80 mm and with iron core it may reach max. 2 T in the horizontal direction. However in the present study the LFV might be damaged due to the static force by ambient $\boldsymbol{B}$, therefore the tests are only up to 1 T.

The examples of three bubbles rising under $B = 1$ T is shown in figure 4.22. The pulses are generated by bubbles and the time-gap between them is 8.5 s. Both the raw data and filtered one are plotted. For each bubble a small peak before main signal is observed (e.g. black dashed line at $t = 1.2$). As described in section 4.1.2, it is caused by the global shift of liquid metal due to the growing bubble at the bottom of liquid domain. It represents the bubble detachment-time. Such signals are enlarged, because the ambient magnetic field induces much higher eddy currents in the flow. The integral of Lorentz force over the liquid domain becomes larger. Considering the filtered signals of LFV 1, the second peak (e.g. red dashed line at $t = 2.5$ s) represents the bubble at same height of LFV 1. Afterwards another peak at LFV 2 (e.g. green dashed line at $t = 3.8$ s) represents the bubble at same height of LFV 2.

We observe that both LFVs can detect bubbles passing by, however without details of the force curve, because the signals for bubbles are in the scale of 1 μN based on our previous experiments, which are far below the resolution of LFV used in the present experiment. However the time-shift between two channels can be calculated and therefore the averaged bubble rising velocity is obtained (so called "time-of-flight" method). It should be noted that the noise of LFV decreases with increasing ambient $\boldsymbol{B}$, because $\boldsymbol{B}$ holds LFV and damps flow fluctuation. When $B < 0.3$ T, the noise is so strong that the peaks cannot be distinguished. We tested the range of $B = 0.3 - 1$ T and recorded the Lorentz force signals for about 100 bubbles. Although sometimes the peaks cannot be observed on one or two channels due to the problem of sensor resolution, there does exist some sufficient signals on both LFVs ($\sim$ 50

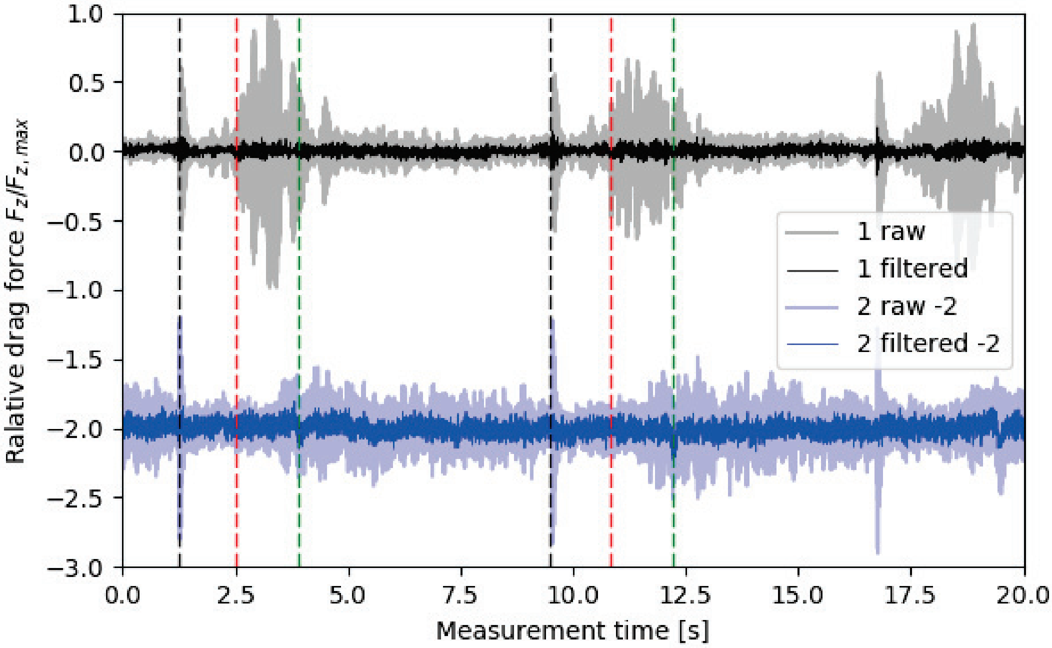

Figure 4.22: Examples of LFV for bubble rising under horizontal ambient magnetic field (obtained by LFV1 (1) and LFV2 (2)).

bubbles). Based on the time-shift of peaks within these selected signals, the effects of ambient ***B*** on bubble velocity is investigated. As shown in figure 4.23, a linear dependence of averaged bubble velocity on ambient magnetic field is observed, which agrees with investigations by Richter et al. [96] and J. Zhang et al. [155]. They investigated the bubble rising velocity in liquid metal by experiment and numerical simulation, respectively. The present experiment shows the functionality of LFV for bubble detection under ambient magnetic field (up to 1 T).

4.6 Conclusion

This chapter presents the experimental and numerical investigations of LFV for bubbles rising in liquid metal initially at rest. With a continuous slow injection of gas at the bottom of liquid domain, the bubbles are generated one after another automatically. The so-called "single bubble regime" is maintained so that each bubble rising has the same initial condition. The Lorentz force signals have some similarities compared with the particle case in chapter 3. The "double peak" pattern occurs in the drag force when the bubble is released near the wall. The lift force has a shape of "zero-crossing-pulse". However, as the bubble deforms and follows a "zig-zag" route during rising, the Lorentz force signals have more fluctuations

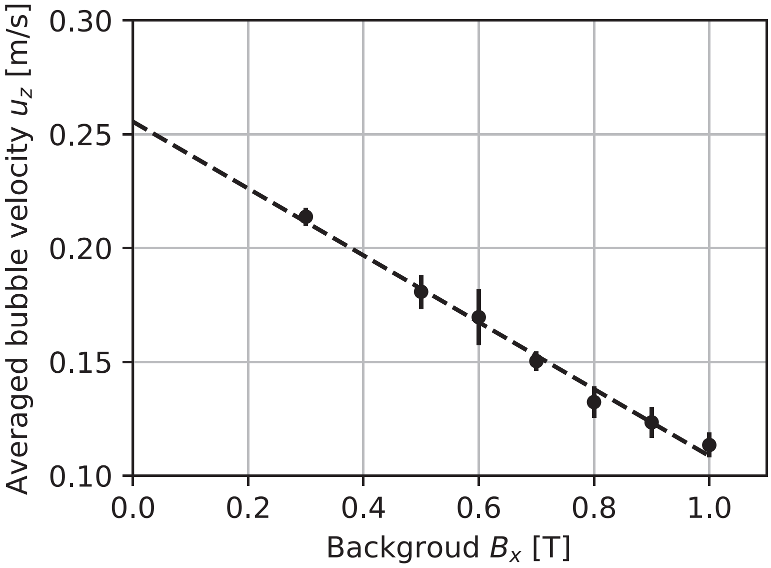

Figure 4.23: Effects of the horizontal ambient magnetic field on bubble rising velocities.

compared to particles. It is difficult to obtain clear dependencies on parameters. The numerical modeling shows qualitative agreement with measurements. One-to-one agreement is challenging since there are many degrees of freedom in the bubble cases (e.g. deformation, rising route). Two additional experiments of LFV for bubble rising at high temperature and under ambient magnetic field are accomplished, respectively. They show the possibility of LFV for applications of liquid metal two-phase flows under harsh environments.

Chapter 5

Summary and outlook

The present work tackles the problem of the interaction of LFV with particle and bubble motion in liquid metals, and the aim is to extend LFV technique for liquid metal two-phase flow applications. The road-map of the present work is shown in figure 5.1.

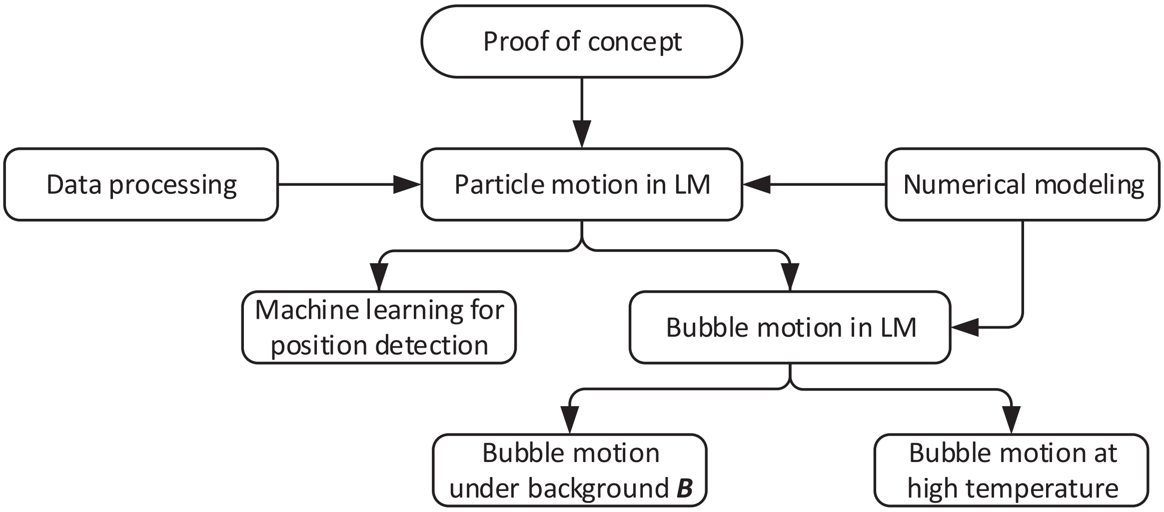

Figure 5.1: Roadmap of the present work.

Firstly the preliminary experiment, which conducts particles rising in a thin tube of liquid metal initially at rest, shows the applicability of LFV to detect moving particles in liquid metals. The significant variation of Lorentz forces in such case results from the wall effects and the hydrodynamic instabilities. To overcome this limit of experimental configuration, the extended experiment of controllable particle motion was then designed and performed. The good reproducibility of Lorentz forces for particle detection is achieved in this setup, and an sufficient data-processing is applied. The "double peak" feature of drag forces and the "zero-crossing-pulse" behavior of lift forces are observed in different *Re* regimes. The corresponding numerical modeling shows promising agreement with measurements. The numerical models are used to explore the parameter space, and the dependence of the peak value of Lorentz force on the particle diameter, magnet size, or distance between particle and wall are investigated, respectively.

Based on the results of LFV for particles detection, the experiments of LFV for bubbles detection are performed. The experimental configurations are identical to the particle case, and the resulting Lorentz forces show some similarities. The "double peak" pattern occurs in the drag force when the bubble is released near the wall. The lift force has "zero-crossing-pulse" behavior as well. However, as the bubble deforms and follows a "zig-zag" route during rising, the Lorentz force signals have more fluctuations compared to particle cases. Therefore it is difficult to identify the parameter influence. The corresponding numerical modeling, which is based the VOF method in commercial software ANSYS Fluent, shows qualitative agreement with measurements. One-to-one agreement between measurement and numerical modeling of bubble rising is challenging, because there are many degrees of freedom in the bubble cases (e.g. deformation, rising route). Additionally, two experiments of LFV for bubbles rising at high temperature and under ambient magnetic field are performed, respectively. They show the functionality of LFV in applications for liquid metal two-phase flows under harsh environments.

Aimed at the feasibility study of LFV for liquid metal two-phase flow applications, we raised five general questions in the beginning for the present work.

• What is the reaction on the permanent magnet in the vicinity of electrically conducting flow around particle or bubble, and conversely what is its influence on the flow?

The "double peak" occurs in the drag force, i.e. the streamwise component of Lorentz force. The trough in between represents the "zero position", because the particle or bubble is non-conductive and there is less conductive volume contributing to the overall Lorentz force at the zero position. The "crossing-zero" pattern is observed in the lift force, i.e. the spanwise component of Lorentz force. We observe very good reproducibility of lift forces in experiments even at high *Re*, because lift force is perpendicular to the particle moving direction and therefore less sensitive to unsteady turbulent wakes comparing to drag force. We may consider the lift force more “robust” for applications compared to drag force, especially for complex flows. In bubble experiments, the patterns of Lorentz forces are similar. However when LFV is very close to the liquid, the patterns changes and we observe much more fluctuations. We assume in this case the rising bubble is significantly influenced by LFV as the interaction parameter is large. The bubble may deform rapidly approaching LFV and change route accordingly. The Lorentz force signal provides us a glance on the process, however such effects are challenging to study and therefore left for further investigations.

• Is it feasible to detect particle or bubble in liquid metal flow using LFV? If so, how much information of the flow features can we reconstruct from the Lorentz force measurement?

It is shown by the present work that LFV is able to detect bubble and particle in liquid metals. The results depends significantly on the experimental configuration. Four aspects must be evaluated carefully for each application of this kind, namely 1) the magnet-size comparing to bubble or particle. The magnet-size reflects how "local" the information is. 2) the distance between the magnet and liquid domain, which surely changes the magnetic flux density in the test sections. 3) the distance between the particle or bubble to the liquid wall, as the nearer the wall is, the stronger its effects on the flow. 4) the particle or bubble velocity comparing to the response time of LFV, which will be described in the next question. The effects of particle velocity, particle diameter, magnet size, distance between particle and the wall on the maximum Lorentz forces are investigated respectively. They form the basis of LFV for the application of bubble or particle detections.

- Which algorithm or method suits best for the processing of Lorentz force signals?

LFV for Liquid metal two-phase flows is generally a fast process. When the frequency of the signals approach the resonance of LFV, huge errors occur in the force measurement. The dynamic compensation method is introduced and validated to exclude this effect. Another issue is the de-noising method. As the Lorentz force for two-phase flows contains information in a broad frequency regime, a straight-forward low-pass filtering in not sufficient. The method with multi-frequency-time-domain, i.e. wavelet in the present work, is tested and proved to be effective. On the other hand, the hydrodynamic instability at high Re (> 1000) introduces uncertainty to the established scaling of LFV to two-phase flow applications. A machine-learning approach, i.e. Neural-network Pattern Recognition in the present work, is tested and validated to predict the particle positions based on LFV measurements.

- Is LFV also suitable for such flow in harsh environment, so that it can be further developed for industrial applications?

The measurements of LFV for bubbles rising at high temperature and under ambient magnetic field are achieved in the present work.

- What are the advantages and limitations of LFV for such applications?

Non-contact is the main advantage of LFV comparing to other methods. Local LFV can measure velocities close to the wall. Local LFV is able to detect the components of the vorticity as well by introducing an innovative torque sensor. Additionally, it seems the strong localized magnetic field influences the flow or bubble rising in the melt near the sensor. The strength of the magnet cannot be reduced because otherwise the forces are too low to measure. Therefore, local LFV is contact-less however also intrusive. Here it is also interesting to compare LFV with another contact-less method with static magnetic field, namely Contact-less inductive flow tomography (CIFT). There is no fundamental difference because both of them reply on the reaction of induced magnetic field. For CIFT the applied magnetic field penetrates the entire liquid domain. CIFT measures the "flow induced magnetic field" at different positions for one applied magnetic field via e.g. hall probes, fluxgate probes. The limitation of LFV comes from its mechanical components. The effects of temperature and inertia of it are challenging in some applications like measurement of hot liquid. Another important aspect is to design array of sensors. It is not difficult to configure CIFT with hundreds of probes, however it is challenging to analyze the interactions between the magnets on multiple LFVs.

Finally, some aspects may be taken into account for further investigations.

- The experimental configuration can be optimized in the design phase. E.g. the magnet should be big enough to record Lorentz force above the resolution of LFV, and not so big that LFV is slow-responding as it must carry the magnet's weight. The distance between LFV and liquid, the length scale of the liquid metal flow, and sizes of the LFV and bubble or particles should be considered together and optimized.
- The data-processing should be improved to reduce noise further.
- Larger parameter space can be explored, e.g. varying the conductivity or magnetic permeability of the particle, investigating LFV for particles of different shapes, multiple particles or liquid droplet rising.
- Using sensors with more components for flow around bubbles or particles, e.g local LFV with complete 6-component of forces and torques.
- Other measurement technique could be applied to reveal the details of local flow as reference, e.g. imaging by high energy radiation. This would allow a detailed comparison with numerical simulations.
- The machine-learning approach could be improved for better prediction performance.
- Using LFV to test the flow with bubbles instead of bubble moving in stagnant liquid, which is more challenging. Then the Lorentz forces consist of strong ambient signals from the flow, which is also fluctuating due to turbulence. The signal-to-noise ratio for bubble becomes even lower. Lorentz force measurement in the spanwise direction of the flow may reduce the noise significantly, in such case LFV may reveal the information of perturbations (induced by bubbles) instead of the main stream.

Nomenclature

Abbreviations

CFD	Computational fluid dynamics
CIFT	Contactless inductive flow tomography
DAQ	Data acquisition unit
FEM	Finite Element Method
FFT	Fast Fourier Tranform
IOFS	Interferometric-Optic-Force-Sensor
LET	Lorentz force eddy current testing
LF	Lorentz force
LFV	Lorentz force velocimetry
LM	Liquid metal
MHD	Magnetohydrodynamics
NPR	Neural-network pattern recognition
UDV	Ultrasonic Doppler Velocimetry
UTTT	Ultrasound Transit-Time Technique
VOF	Volume of fluid method

Constants

μ	dynamic viscosity of GaInSn	$0.0024\,\mathrm{Pa\cdot s}$
μ_0	magnetic permeability of vacuum	$4\pi \times 10^{-7}\,\mathrm{H/m}$
ρ	density of GaInSn	$6492\,\mathrm{kg/m^3}$
σ	electrical conductivity of GaInSn	$3.46 \times 10^{6}\,\mathrm{S/m}$
k_0	static calibration factor of IOFS	$3.0653 \times 10^{-4}\,\mathrm{N/m}$

Variables

$\boldsymbol{B}$	magnetic field	
$\boldsymbol{b}$	induced magnetic field	
$\boldsymbol{B}_0$	magnetic field of the permanent magnet	
$\boldsymbol{E}$	electric field	
ϕ	scalar potential of electric field	
$\boldsymbol{j}$	eddy current density	
$\boldsymbol{f}$	Lorentz force density	
$\boldsymbol{u}$	liquid vecocity	
L	characteristic length of the flow	
p	liquid pressure	
u_0	velocity of bubble or particle	$0.01 - 0.22\,\mathrm{m/s}$
t_m	measurement time	
t_0	reference time of zero position	
F_L	total force on LFV	
F_z	drag force (vertical Lorentz force)	
$F_{z,max}$	maximum drag force	
F_x	lift force (horizontal Lorentz force)	
$F_{x,max}$	maximum lift force	
s	frequency space	
$G(s)$	transfer function of IOFS	
ω_0	resonant frequency of IOFS	
ε	damping coefficient of IOFS	
$Sa(F_{ran}),\ Sr(F_{ran})$	absolute- and relative random error of LFV measurement	
$Sa(F_{sys}),\ Sr(F_{sys})$	absolute- and relative systematic error of LFV measurement	
SP	successful prediction rate of particle positions	

Geometrical parameters

d	diameter of particle or bubble	$4-8\,\mathrm{mm}$
D_i	inner diameter of the thin tube	$20\,\mathrm{mm}$
L_1	distance between magnet surface and liquid	$4-9\,\mathrm{mm}$
L_2	z-axial distance between magnet and particle	$\pm 150\,\mathrm{mm}$
L_3	distance between particle center and wall	$5-30\,\mathrm{mm}$
L_4	side length of the magnet	$5-30\,\mathrm{mm}$

Non-dimensional parameters

$Re = u_0 d \rho / \mu$	Reynolds number	$160-3500$
$Re_m = \mu_0 \sigma u_0 d$	magnetic Reynolds number	
$Ha = B_0 d \sqrt{\frac{\sigma}{\mu}}$	Hartmann number	
$N = \frac{\sigma B_0^2 d}{\rho u_0}$	Interaction parameter number	

List of Figures

List of Publications

1. Z. Lyu, N. Tran, T. Boeck, R. Maragoni, U. Lütdke, and C. Karcher. "Particle motion in a conducting liquid and a localized magnetic field." In: (2018), (in preparation)
2. Z. Lyu and C. Karcher. "Non-contact electromagnetic flow measurement in liquid metal two-phase flow using Lorentz force velocimetry." In: *Magnetohydrodynamics* 53.1 (2017), pp. 67–77
3. Z. Lyu, T. Boeck, C. Karcher, and A. Thess. "Electromagnetic interaction between a permanent magnet and laminar flow of a moving sphere in a conducting liquid." In: *Magnetohydrodynamics* 53.4 (2017), pp. 653–665
4. S. Prinz, Z. Lyu, Y. Kolesnikov, and T. Boeck. "Magnetohydrodynamic flows driven by an oscillating permanent magnet." In: (2018), (in preparation)
5. N. Tran, Z. Lyu, and U. Lüdtke. "Numerical Model for the Detection of Single Particle in Two-Phase Lorentz Force Velocimetry." In: *IEEE Transactions on Magnetics* 55.2 (2019), pp. 1–4
6. N. Tran, T. Boeck, U. Lüdtke, Z. Lyu, and C. Karcher. "Numerical study of the interaction between a bubble rising in a column of conducting liquid and a permanent magnet." In: *Magnetohydrodynamics* 53.4 (2017), pp. 619–631
7. Z. Lyu, N. Tran, T. Boeck, and C. Karcher. "Electromagnetic interaction between a rising spherical particle in a conducting liquid and a localized magnetic field." In: *IOP Conference Series: Materials Science and Engineering*. Vol. 228. 1. IOP Publishing. 2017, p. 012025
8. C. Karcher, Z. Lyu, T. Boeck, N. Tran, and U. Lüdtke. "Experimental and numerical investigation on particle-induced liquid metal flow using Lorentz force velocimetry." In: *IOP Conference Series: Materials Science and Engineering*. Vol. 424. 1. IOP Publishing. 2018, p. 012006
9. Z. Lyu, C. Karcher, Y. Kolesnikov, and T. Boeck. "Electromagnetic flow rate measurement in molten tin circulating in a closed-loop test system." In: *IOP Conference Series: Materials Science and Engineering*. Vol. 424. 1. IOP Publishing. 2018, p. 012084
10. Z. Lyu and C. Karcher. "Lorentz force measurement of particle movement in liquid metal." In: *Proceedings of Workshop Elektroprozesstechnik*. 2017

11. Z. Lyu and C. Karcher. “Flow measurement in liquid metal two-phase flow using Local Lorentz Force Velocimetry.” In: *Pcoceedings of Workshop Elektroprozesstechnik*. 2016

References

[1] B. M. Abbagoni and H. Yeung. “Non-invasive classification of gas–liquid two-phase horizontal flow regimes using an ultrasonic Doppler sensor and a neural network.” In: *Measurement Science and Technology* 27.8 (2016), p. 084002.

[2] A. Alferenok. “Numerical Simulation and Optimization of the Magnet System for Lorentz Force Velocimetry of Low-conducting Materials.” PhD thesis. Technische Universität Ilmenau, 2013.

[3] H. Alfvén. “Existence of electromagnetic-hydrodynamic waves.” In: *Nature* 150.3805 (1942), p. 405.

[4] S. Alkhalil. “Lorentz force sigmometry: a novel technique to measure the electrical conductivity of solid and fluid metals.” PhD thesis. Technische Universität Ilmenau, 2016.

[5] O. Andreew, T. Gundrum, T. Wondrak, S. Eckert, and G. Gerbeth. “Sensitivity of electromagnetic method for gas bubble detection in liquid metal flows.” In: *Proceedings of 8th International Conference on Electromagnetic Processing of Materials*. 2015.

[6] R. Andreini, J. Foster, and R. Callen. “Characterization of gas bubbles injected into molten metals under laminar flow conditions.” In: *Metallurgical Transactions B* 8.4 (1977), pp. 625–631.

[7] A. Andruszkiewicz, K. Eckert, S. Eckert, and S. Odenbach. “Gas bubble detection in liquid metals by means of the ultrasound transit-time-technique.” In: *The European Physical Journal Special Topics* 220.1 (2013), pp. 53–62.

[8] H. Arcos-Gutierrez, J. d. J. Barreto, S. Garcia-Hernandez, and A. Ramos-Banderas. “Mathematical analysis of inclusion removal from liquid steel by gas bubbling in a casting tundish.” In: *Journal of Applied Mathematics* 2012 (2012).

[9] H. Bai and B. G. Thomas. “Turbulent flow of liquid steel and argon bubbles in slide-gate tundish nozzles: Part I. Model development and validation.” In: *Metallurgical and Materials Transactions B* 32.2 (2001), pp. 253–267.

[10] V. Bandaru. “Magnetohydrodynamic duct and channel flows at finite magnetic Reynolds numbers.” PhD thesis. Technische Universität Ilmenau, 2016.

[11] L. Bühler, S. Horanyi, and C. Mistrangelo. “Interpretation of LEVI velocity signals in 3D MHD flows.” In: *Fusion Engineering and Design* 83.10-12 (2008), pp. 1822–1827.

[12] M. Carlstedt. “A contribution to the experimental validation in Lorentz force eddy current testing.” PhD thesis. Technische Universität Ilmenau, 2017.

[13] V. Chevrier and A. Cramb. “X-ray fluoroscopy observations of bubble formation and separation at a metal-slag interface.” In: *Metallurgical and Materials Transactions B* 31.3 (2000), pp. 537–540.

[14] X. Dai, X. Yang, J. Campbell, and J. Wood. “Effects of runner system design on the mechanical strength of Al–7Si–Mg alloy castings.” In: *Materials Science and Engineering: A* 354.1-2 (2003), pp. 315–325.

[15] P. A. Davidson. *An introduction to magnetohydrodynamics*. Vol. 25. Cambridge university press, 2001.

[16] S. Degaleesan, M. Dudukovic, and Y. Pan. “Experimental study of gas-induced liquid-flow structures in bubble columns.” In: *AIChE journal* 47.9 (2001), pp. 1913–1931.

[17] C. Diethold. “Lorentzkraft-Anemometrie von elektrisch schwach leitfähigen Fluiden.” PhD thesis. Technische Universität Ilmenau, 2016.

[18] F. Dobran. “On the consistency conditions of averaging operators in 2-phase flow models and on the formulation of magnetohydrodynamic 2-phase flow.” In: *International Journal of Engineering Science* 19.10 (1981), pp. 1353–1368.

[19] E. Dölker, R. Schmidt, K. Weise, B. Petkovic, M. Ziolkowski, H. Brauer, and J. Haueisen. “Assessment of Two Forward Solution Approaches in Lorentz Force Evaluation.” In: *IEEE Transactions on Magnetics* 54.3 (2018), p. 6200105.

[20] X. Dong, C. Tan, and F. Dong. “Gas–liquid two-phase flow velocity measurement with continuous wave ultrasonic Doppler and conductance sensor.” In: *IEEE Transactions on Instrumentation and Measurement* 66.11 (2017), pp. 3064–3076.

[21] N. Dubovikova. “Non-contact flow rate measurements in turbulent liquid metal duct flow using time-of-flight Lorentz force velocimetry.” PhD thesis. Technische Universität Ilmenau, 2016.

[22] P. F. Dunn. “Single-phase and two-phase magnetohydrodynamic pipe flow.” In: *International Journal of Heat and Mass Transfer* 23.3 (1980), pp. 373–385.

[23] T. Dyakowski, L. F. Jeanmeure, and A. J. Jaworski. “Applications of electrical tomography for gas–solids and liquid–solids flows—a review.” In: *Powder technology* 112.3 (2000), pp. 174–192.

[24] S. Eckert and G. Gerbeth. “Velocity measurements in liquid sodium by means of ultrasound Doppler velocimetry.” In: *Experiments in Fluids* 32.5 (2002), pp. 542–546.

[25] S. Eckert, G. Gerbeth, T. Gundrum, F. Stefani, and W. Witke. “New approaches to determine the velocity field in metallic melts.” In: *Proceedings of the Electromagnetic Processing of Materials International Conference*. 2003.

[26] S. Eckert, G. Gerbeth, and O. Lielausis. "The behaviour of gas bubbles in a turbulent liquid metal magnetohydrodynamic flow: Part I: Dispersion in quasi-two-dimensional magnetohydrodynamic turbulence." In: *International journal of multiphase flow* 26.1 (2000), pp. 45–66.

[27] S. Eckert, G. Gerbeth, and O. Lielausis. "The behaviour of gas bubbles in a turbulent liquid metal magnetohydrodynamic flow: Part II: Magnetic field influence on the slip ratio." In: *International journal of multiphase flow* 26.1 (2000), pp. 67–82.

[28] S. Eckert, G. Gerbeth, and V. Melnikov. "Velocity measurements at high temperatures by ultrasound Doppler velocimetry using an acoustic wave guide." In: *Experiments in fluids* 35.5 (2003), pp. 381–388.

[29] S. Eckert, W. Witke, and G. Gerbeth. "A new mechano-optical technique to measure local velocities in opaque fluids." In: *Flow Measurement and Instrumentation* 11.2 (2000), pp. 71–78.

[30] G. Fabris, P. Dunn, and E. Pierson. *Local measurements in two-phase liquid-metal MHD*. Tech. rep. Argonne National Lab., Ill.(USA), 1978.

[31] B. Farrar, A. Samways, J. Ali, and H. Bruun. "A computer-based hot-film technique for two-phase flow measurements." In: *Measurement Science and Technology* 6.10 (1995), p. 1528.

[32] J. Fröhlich, S. Schwarz, S. Heitkam, C. Santarelli, C. Zhang, T. Vogt, S. Boden, A. Andruszkiewicz, K. Eckert, S. Odenbach, et al. "Influence of magnetic fields on the behavior of bubbles in liquid metals." In: *The European Physical Journal Special Topics* 220.1 (2013), pp. 167–183.

[33] E. P. Furlani. *Permanent magnet and electromechanical devices: materials, analysis, and applications*. Academic Press, London, U.K., 2001.

[34] R. Füßl and G. Jäger. "The influence of the force feed-in system on high-accuracy low force measurement." In: *Proceedings of XIX IMEKO World Congress—Fundamental and Applied Metrology*. 2009.

[35] P. Gherson and P. S. Lykoudis. "Local measurements in two-phase liquid-metal magneto-fluid-mechanic flow." In: *Journal of Fluid Mechanics* 147 (1984), pp. 81–104.

[36] H. Griffiths. "Magnetic induction tomography." In: *Measurement science and technology* 12.8 (2001), p. 1126.

[37] R. Guichou, P. Tordjeman, R. Zamansky, W. Bergez, and K. Paumel. "Experimental study of bubble detection in liquid metal." In: *Magnetohydrodynamics c/c of Magnitnaia Gidrodinamika* 53.4 (2017), pp–667.

[38] T. Gundrum, P. Büttner, B. Dekdouk, A. Peyton, T. Wondrak, V. Galindo, and S. Eckert. "Contact-less inductive bubble detection in a liquid metal flow." In: *Sensors* 16.1 (2016), p. 63.

[39] R. A. Hartunian and W. Sears. “On the instability of small gas bubbles moving uniformly in various liquids.” In: *Journal of Fluid Mechanics* 3.1 (1957), pp. 27–47.

[40] C. Heinicke. “Local Lorentz Force Velocimetry for liquid metal duct flows.” PhD thesis. Technische Universität Ilmenau, 2012.

[41] C. Heinicke and T. Wondrak. “Spatial and temporal resolution of a local Lorentz force flowmeter.” In: *Measurement Science and Technology* 25.5 (2014), p. 055302.

[42] S. Heitkam, W. Drenckhan, and J. Fröhlich. “Packing spheres tightly: influence of mechanical stability on close-packed sphere structures.” In: *Physical review letters* 108.14 (2012), p. 148302.

[43] D. Hernández. “Multicomponent local Lorentz force velocimetry.” PhD thesis. Technische Universität Ilmenau, 2018.

[44] D. Hernández, J. Schleichert, C. Karcher, T. Fröhlich, T. Wondrak, and K. Timmel. “Local Lorentz force flowmeter at a continuous caster model using a new generation multicomponent force and torque sensor.” In: *Measurement Science and Technology* 27.6 (2016), p. 065302.

[45] J. Hunt and R. Moreau. “Liquid-metal magnetohydrodynamics with strong magnetic fields: a report on Euromech 70.” In: *Journal of Fluid Mechanics* 78.02 (1976), pp. 261–288.

[46] M. Iguchi, H. Kawabata, Y. Ito, K. Nakajima, and Z.-i. Morita. “Continuous measurements of bubble characteristics in a molten iron bath with Ar gas injection.” In: *ISIJ International* 34.12 (1994), pp. 980–985.

[47] A. Inoue, M. Aritomi, M. Takahashi, Y. Narita, T. Yano, and M. Matsuzakim. “Studies on MHD pressure drop and heat transfer of Helium-Lithium annular-mist flow in a transverse magnetic field: heat transfer, power, combustion, thermophysical properties.” In: *JSME international journal* 30.269 (1987), pp. 1768–1775.

[48] G. Irons and R. Guthrie. “Bubbling behaviour in molten metals.” In: *Canadian Metallurgical Quarterly* 19.4 (1980), pp. 381–387.

[49] D. Jian. “Flow measurement in liquid metals using Lorentz force velocimetry: laboratory experiments and numerical simulations.” PhD thesis. Technische Universität Ilmenau, 2013.

[50] C. Karcher, Z. Lyu, T. Boeck, N. Tran, and U. Lüdtke. “Experimental and numerical investigation on particle-induced liquid metal flow using Lorentz force velocimetry.” In: *IOP Conference Series: Materials Science and Engineering*. Vol. 424. 1. IOP Publishing. 2018, p. 012006.

[51] O. Keplinger, N. Shevchenko, and S. Eckert. “Visualization of bubble coalescence in bubble chains rising in a liquid metal.” In: *International Journal of Multiphase Flow* 105 (2018), pp. 159–169.

[52] L. Kit, Y. B. Kolesnikov, A. Tsinober, and P. Shtern. “Use of a conduction anemometer in investigating the MHD wake behind a body.” In: *Magnetohydrodynamics* 5.4 (1969), pp. 46–50.

[53] Y. Kolesnikov, C. Karcher, and A. Thess. “Lorentz force flowmeter for liquid aluminum: laboratory experiments and plant tests.” In: *Metallurgical and Materials Transactions B* 42.3 (2011), pp. 441–450.

[54] D. v. Krevelen and P. Hoftijzer. “Studies of gas-bubble formation.” In: *Chemical Engineering Progress* 46.1 (1950), pp. 29–35.

[55] K. Krishnapisharody and G. Irons. “A critical review of the modified froude number in ladle metallurgy.” In: *Metallurgical and Materials Transactions B* 44.6 (2013), pp. 1486–1498.

[56] B. Krull, E. Strumpf, O. Keplinger, N. Shevchenko, J. Fröhlich, S. Eckert, and G. Gerbeth. “Combined experimental and numerical analysis of a bubbly liquid metal flow.” In: *IOP Conference Series: Materials Science and Engineering*. Vol. 228. 1. IOP Publishing. 2017, p. 012006.

[57] I. Leibson, E. G. Holcomb, A. G. Cacoso, and J. J. Jacmic. “Rate of flow and mechanics of bubble formation from single submerged orifices. I. Rate of flow studies.” In: *AIChE Journal* 2.3 (1956), pp. 296–300.

[58] F.-C. Li, T. Kunugi, and A. Serizawa. “MHD effect on flow structures and heat transfer characteristics of liquid metal–gas annular flow in a vertical pipe.” In: *International journal of heat and mass transfer* 48.12 (2005), pp. 2571–2581.

[59] O. Lielausis. “Liquid-metal magnetohydrodynamics.” In: *Atomic Energy Review* 13.3 (1975), pp. 527–581.

[60] Z. Lyu, T. Boeck, C. Karcher, and A. Thess. “Electromagnetic interaction between a permanent magnet and laminar flow of a moving sphere in a conducting liquid.” In: *Magnetohydrodynamics* 53.4 (2017), pp. 653–665.

[61] Z. Lyu and C. Karcher. “Non-contact electromagnetic flow measurement in liquid metal two-phase flow using Lorentz force velocimetry.” In: *Magnetohydrodynamics* 53.1 (2017), pp. 67–77.

[63] Z. Lyu, N. Tran, T. Boeck, and C. Karcher. “Electromagnetic interaction between a rising spherical particle in a conducting liquid and a localized magnetic field.” In: *IOP Conference Series: Materials Science and Engineering*. Vol. 228. 1. IOP Publishing. 2017, p. 012025.

[67] X. Ma, A. J. Peyton, R. Binns, and S. R. Higson. “Electromagnetic techniques for imaging the cross-section distribution of molten steel flow in the continuous casting nozzle.” In: *IEEE Sensors Journal* 5.2 (2005), pp. 224–232.

[68] S. Mallat. *A wavelet tour of signal processing: the sparse way*. Academic press, 2008.

[69] H. R. A. Mallock. “The damping of sound by frothy liquids.” In: *Proc. R. Soc. Lond. A* 84.572 (1910), pp. 391–395.

[70] R. R. Marangoni, J. Schleichert, I. Rahneberg, R. Mastylo, E. Manske, and T. Fröhlich. “Multi-component force measurement in micromachining.” In: *tm-Technisches Messen* 84.9 (2017), pp. 587–592.

[71] I. Michiyoshi, H. Funakawa, C. Kuramoto, Y. Akita, and O. Takahashi. “Local properties of vertical mercury-argon two-phase flow in a circular tube under transverse magnetic field.” In: *International Journal of Multiphase Flow* 3.5 (1977), pp. 445–457.

[72] V. Minchenya, C. Karcher, Y. Kolesnikov, and A. Thess. “Calibration of the Lorentz force flowmeter.” In: *Flow Measurement and Instrumentation* 22.3 (2011), pp. 242–247.

[73] M. Minnaert. “XVI. On musical air-bubbles and the sounds of running water.” In: *The London, Edinburgh, and Dublin Philosophical Magazine and Journal of Science* 16.104 (1933), pp. 235–248.

[74] W. Mirihanage, W. Xu, J. Tamayo-Ariztondo, D. Eskin, M. Garcia-Fernandez, P. Srirangam, and P. Lee. “Synchrotron radiographic studies of ultrasonic melt processing of metal matrix nano composites.” In: *Materials Letters* 164 (2016), pp. 484–487.

[75] C. Mistrangelo and L. Bühler. “Perturbing effects of electric potential probes on MHD duct flows.” In: *Experiments in fluids* 48.1 (2010), pp. 157–165.

[76] R. J. Moreau. *Magnetohydrodynamics*. Vol. 3. Springer Science & Business Media, 2013.

[77] K. Mori, Y. Ozawa, and M. Sano. “Characterization of gas jet behavior at a submerged orifice in liquid metal.” In: *Transactions of the Iron and Steel Institute of Japan* 22.5 (1982), pp. 377–384.

[78] Y. Mori, K. Hijikata, and I. Kuriyama. “Experimental study of bubble motion in mercury with and without a magnetic field.” In: *Journal of Heat Transfer* 99.3 (1977), pp. 404–410.

[79] N. B. Morley, S. Smolentsev, L. Barleon, I. R. Kirillov, and M. Takahashi. “Liquid magnetohydrodynamics—recent progress and future directions for fusion.” In: *Fusion Engineering and design* 51 (2000), pp. 701–713.

[80] L. G. Neal and S. Bankoff. “Local parameters in cocurrent mercury-nitrogen flow: Parts I and II.” In: *AIChE Journal* 11.4 (1965), pp. 624–635.

[81] A. V. Oppenheim and R. W. Schafer. *Discrete-time signal processing*. Pearson Education, 2014.

[82] C. Oseen. “Stokes’ formula and a related theorem in hydrodynamics.” In: *Arkiv. Mat. Astron. Fysik* 6 (1910), p. 20.

[83] R. Owen, J. Hunt, and J. Collier. “Magnetohydrodynamic pressure drop in ducted two-phase flows.” In: *International Journal of Multiphase Flow* 3.1 (1976), pp. 23–33.

[84] B. Petković. “Assessment of linear inverse problems in magnetocardiography and Lorentz force eddy current testing.” PhD thesis. Technische Universität Ilmenau, 2013.

[85] B. Petković, K. Weise, and J. Haueisen. “Computation of Lorentz force and 3-D eddy current distribution in translatory moving conductors in the field of a permanent magnet.” In: *IEEE Transactions on Magnetics* 53.2 (2017), pp. 1–9.

[86] A. Peyton. “Electromagnetic induction tomography.” In: *Industrial Tomography*. Elsevier, 2015, pp. 61–107.

[87] C. Pfeiler, M. Wu, and A. Ludwig. “Influence of argon gas bubbles and non-metallic inclusions on the flow behavior in steel continuous casting.” In: *Materials Science and Engineering: A* 413 (2005), pp. 115–120.

[88] A. Pothérat and R. Klein. “Why, how and when MHD turbulence at low Re_m becomes three-dimensional.” In: *Journal of Fluid Mechanics* 761 (2014), pp. 168–205.

[89] J. Priede, D. Buchenau, and G. Gerbeth. “Contactless electromagnetic phase-shift flowmeter for liquid metals.” In: *Measurement Science and Technology* 22.5 (2011), p. 055402.

[90] S. Prinz, V. Bandaru, Y. Kolesnikov, D. Krasnov, and T. Boeck. “Numerical simulations of magnetohydrodynamic flows driven by a moving permanent magnet.” In: *Physical Review Fluids* 1.4 (2016), p. 043601.

[92] I. Rahneberg. “Untersuchungen zu optischen Mehrkomponentenmesssystemen.” PhD thesis. Technische Universität Ilmenau, 2013.

[93] R. Rakoczy and S. Masiuk. “Experimental study of bubble size distribution in a liquid column exposed to a rotating magnetic field.” In: *Chemical Engineering and Processing: Process Intensification* 48.7 (2009), pp. 1229–1240.

[94] M. Ratajczak, D. Hernández, T. Richter, D. Otte, D. Buchenau, N. Krauter, and T. Wondrak. “Measurement techniques for liquid metals.” In: *IOP Conference Series: Materials Science and Engineering*. Vol. 228. 1. IOP Publishing. 2017, p. 012023.

[95] M. Ratajczak, T. Gundrum, F. Stefani, and T. Wondrak. “Contact-less inductive flow tomography: brief history and recent developments in its application to continuous casting.” In: *Journal of Sensors* Article ID 739161, 9 pages (2014).

[96] T. Richter, O. Keplinger, N. Shevchenko, T. Wondrak, K. Eckert, S. Eckert, and S. Odenbach. “Single bubble rise in GaInSn in a horizontal magnetic field.” In: *International Journal of Multiphase Flow* 104 (2018), pp. 32–41.

[97] R. Ricou and C. Vives. “Local velocity and mass transfer measurements in molten metals using an incorporated magnet probe.” In: *International Journal of Heat and Mass Transfer* 25.10 (1982), pp. 1579–1588.

[98] P. Saffman. “On the rise of small air bubbles in water.” In: *Journal of Fluid Mechanics* 1.3 (1956), pp. 249–275.

[99] M. Saito, S. Inoue, and Y. Fujii-e. “Gas-liquid slip ratio and MHD pressure drop in two-phase liquid metal flow in strong magnetic field.” In: *Journal of Nuclear Science and Technology* 15.7 (1978), pp. 476–489.

[100] Y. Saito, K. Mishima, Y. Tobita, T. Suzuki, and M. Matsubayashi. “Measurements of liquid–metal two-phase flow by using neutron radiography and electrical conductivity probe.” In: *Experimental thermal and fluid science* 29.3 (2005), pp. 323–330.

[101] F. Samsami, Y. Kolesnikov, and A. Thess. “Vortex dynamics in the wake of a magnetic obstacle.” In: *Journal of Visualization* 17.3 (2014), pp. 245–252.

[102] M. Sano and K. Mori. “Bubble formation from single nozzles in liquid metals.” In: *Transactions of the Japan Institute of Metals* 17.6 (1976), pp. 344–352.

[103] M. Sano and K. Mori. “Fluid flow and mixing characteristics in a gas-stirred molten metal bath.” In: *Transactions of the Iron and Steel Institute of Japan* 23.2 (1983), pp. 169–175.

[104] L. Sartini, F. Simeone, P. Pani, N. Lo Bue, G. Marinaro, A. Grubich, A. Lobko, G. Etiope, A. Capone, P. Favali, et al. “Nuclear instruments and methods in physics research section a: Accelerators, spectrometers, detectors and associated equipment.” In: *Nuclear Instruments and Methods in Physics Research A* (2010).

[105] M. Ščepanskis, M. Sarma, P. Vontobel, P. Trtik, K. Thomsen, A. Jakovičs, and T. Beinerts. “Assessment of electromagnetic stirrer agitated liquid metal flows by dynamic neutron radiography.” In: *Metallurgical and materials transactions B* 48.2 (2017), pp. 1045–1054.

[106] J. Schleichert. “Entwicklung und Untersuchung von Mehrkomponentensensoren für Kraft und Drehmoment.” PhD thesis. Technische Universität Ilmenau, 2015.

[107] J. Schleichert, M. Carlstedt, R. Marangoni, I. Rahneberg, and T. Fröhlich. “Dynamic characterization of a multi-component force transducer using a lorentz force load changer.” In: *Proceedings of 58th IWK Ilmenau Scientific Colloquium*. Vol. 24. 2014, p. 1360017.

[108] R. Schmidt, J. M. Otterbach, M. Ziolkowski, H. Brauer, and H. Toepfer. “Portable Lorentz Force Eddy Current Testing System With Rotational Motion.” In: *IEEE Transactions on Magnetics* 54.3 (2018), pp. 1–4.

[109] S. Schwarz and J. Fröhlich. “Numerical study of single bubble motion in liquid metal exposed to a longitudinal magnetic field.” In: *International Journal of Multiphase Flow* 62 (2014), pp. 134–151.

[110] A. Serizawa, T. Ida, O. Takahashi, and I. Michiyoshi. “MHD effect on Nak-nitrogen two-phase flow and heat transfer in a vertical round tube.” In: *International Journal of Multiphase Flow* 16.5 (1990), pp. 761–788.

[111] A. Serizawa, I. Kataoka, and I. Michiyoshi. “Turbulence structure of air-water bubbly flow—I. Measuring techniques.” In: *International Journal of Multiphase Flow* 2.3 (1975), pp. 221–233.

[112] S. Shin and I. Kang. “Effects of magnetic field on the shape of a bubble in a uniaxial straining flow.” In: *International journal of multiphase flow* 28.1 (2002), pp. 105–125.

[113] I. Sokolov. “Lorentz Force Velocimetry at High Magnetic Reynolds Numbers.” PhD thesis. Technische Universität Ilmenau, 2016.

[114] F. Stefani, T. Gundrum, and G. Gerbeth. “Contactless inductive flow tomography.” In: *Physical Review E* 70.5 (2004), p. 056306.

[115] E. Strumpf. “Experimental study on rise velocities of single bubbles in liquid metal under the influence of strong horizontal magnetic fields in a flat vessel.” In: *International Journal of Multiphase Flow* 97 (2017), pp. 168–185.

[116] C. Suzanne, K. Ellingsen, F. Risso, and V. Roig. “Local measurements in turbulent bubbly flows.” In: *Nuclear engineering and design* 184.2-3 (1998), pp. 319–327.

[117] Y. Suzuki, M. Aritomi, H. Kikura, M. Nakagawa, and M. Mori. “Measurement of the flow around bubbles using the ultrasonic velocity profile monitor. On the influence of the measuring volume.” In: *Bulletin of the Research Laboratory for Nuclear Reactors (Tokyo Institute of Technology)* 3.special issue (2000), pp. 93–99.

[118] M. Takahashi and Y. Momozaki. “Pressure drop and heat transfer of a mercury single-phase flow and an air–mercury two-phase flow in a helical tube under a strong magnetic field.” In: *Fusion engineering and design* 51 (2000), pp. 869–877.

[119] N. Takenaka, T. Fujii, A. Ono, K. Sonoda, S. Tazawa, and T. Nakanii. “Visualization of streak lines in liquid metal by neutron radiography.” In: *Nondestructive Testing And Evaluation* 11.2-3 (1994), pp. 107–113.

[120] S. Taneda. “Experimental investigation of the wake behind a sphere at low Reynolds numbers.” In: *Journal of the Physical Society of Japan* 11.10 (1956), pp. 1104–1108.

[121] J. Taylor. *Introduction to error analysis, the study of uncertainties in physical measurements*. 1997.

[122] N. Terzija, W. Yin, G. Gerbeth, F. Stefani, K. Timmel, T. Wondrak, and A. Peyton. “Electromagnetic inspection of a two-phase flow of GaInSn and argon.” In: *Flow Measurement and Instrumentation* 22.1 (2011), pp. 10–16.

[123] A. Thess, E. Votyakov, and Y. Kolesnikov. “Lorentz force velocimetry.” In: *Physical Review Letters* 96.16 (2006), p. 164501.

[124] A. Thess, E. Votyakov, B. Knaepen, and O. Zikanov. “Theory of the Lorentz force flowmeter.” In: *New Journal of Physics* 9.8 (2007), p. 299.

[125] R. J. Thome. *Effect of a transverse magnetic field on vertical two-phase flow through a rectangular channel*. Tech. rep. Argonne National Lab, Ill.; and Associated Midwest Universities, Lemont, Ill., 1964.

[126] K. Timmel, N. Shevchenko, M. Röder, M. Anderhuber, P. Gardin, S. Eckert, and G. Gerbeth. “Visualization of liquid metal two-phase flows in a physical model of the continuous casting process of steel.” In: *Metallurgical and Materials Transactions B* 46.2 (2015), pp. 700–710.

[127] N. Tran, T. Boeck, U. Lüdtke, Z. Lyu, and C. Karcher. “Numerical study of the interaction between a bubble rising in a column of conducting liquid and a permanent magnet.” In: *Magnetohydrodynamics* 53.4 (2017), pp. 619–631.

[128] N. Tran, Z. Lyu, and U. Lüdtke. “Numerical Model for the Detection of Single Particle in Two-Phase Lorentz Force Velocimetry.” In: *IEEE Transactions on Magnetics* 55.2 (2019), pp. 1–4.

[129] S. Tschisgale, T. Kempe, and J. Fröhlich. “A non-iterative immersed boundary method for spherical particles of arbitrary density ratio.” In: *Journal of Computational Physics* 339 (2017), pp. 432–452.

[130] S. Tympel. “Magnetohydrodynamic duct flow in the presence of a magnetic dipole.” PhD thesis. Technische Universität Ilmenau, 2013.

[131] R. P. Uhlig. “Identification of Material Defects in Metallic Materials Using Lorentz Force Eddy Current Testing.” PhD thesis. Technische Universität Ilmenau, 2012.

[132] O. Vakaliuk, M. Weidner, and B. Halbedel. “High-temperature superconducting magnet systems for Lorentz Force Velocimetry.” In: *Proceedings of XVIII International UIE-Congress: Electrotechnologies for Material Processing*. 2017.

[133] D. Van Krevelen and P. Hoftijzer. “Kinetics of gas-liquid reactions part I. General theory.” In: *Recueil des Travaux Chimiques des Pays-Bas* 67.7 (1948), pp. 563–586.

[134] S. Vasilyan. “High precision force measurements in horizontal direction in combination with high dead loads: non-contact flowmeter for low conducting electrolytes.” PhD thesis. Technische Universität Ilmenau, 2016.

[135] T. Wang, J. Wang, F. Ren, and Y. Jin. “Application of Doppler ultrasound velocimetry in multiphase flow.” In: *Chemical Engineering Journal* 92.1-3 (2003), pp. 111–122.

[136] A. Wegfraß. “Experimentelle Untersuchungen zur Anwendbarkeit der Lorentzkraft-Anemometrie auf schwach leitfähige Fluide.” PhD thesis. Technische Universität Ilmenau, 2013.

[137] C. Weidermann. “Design and laboratory test of a Lorentz force flowmeter for pipe flows.” PhD thesis. Technische Universität Ilmenau, 2013.

[138] M. Weidner, B. Halbedel, and E. Rädlein. "Expectable Forces of Lorentz Force Velocimetry in low conducting and slow flowing solutions by the use of high-T c superconductors." In: *Proceedings of 8th International Conference on Electromagnetic Processing of Materials*. 2015.

[139] K. Weise. "Advanced modeling in Lorentz force eddy current testing." PhD thesis. Technische Universität Ilmenau, 2016.

[140] K. Weise, R. Schmidt, M. Carlstedt, M. Ziolkowski, H. Brauer, and H. Toepfer. "Optimal magnet design for Lorentz force eddy-current testing." In: *IEEE Transactions on Magnetics* 51.9 (2015), pp. 1–15.

[141] M. Werner. "Design, optimierung, realisierung und test von passiven magnetsystemen für die lorentzkraftanemometrie an elektrolyten." PhD thesis. Technische Universität Ilmenau, 2012.

[142] A. Wiederhold, R. Ebert, M. Weidner, B. Halbedel, T. Fröhlich, and C. Resagk. "Influence of the flow profile to Lorentz force velocimetry for weakly conducting fluids—an experimental validation." In: *Measurement Science and Technology* 27.12 (2016), p. 125306.

[143] L. van Wijngaarden. "One-dimensional flow of liquids containing small gas bubbles." In: *Annual review of fluid Mechanics* 4.1 (1972), pp. 369–396.

[144] T. Wondrak, S. Eckert, G. Gerbeth, K. Klotsche, F. Stefani, K. Timmel, A. J. Peyton, N. Terzija, and W. Yin. "Combined electromagnetic tomography for determining two-phase flow characteristics in the submerged entry nozzle and in the mold of a continuous casting model." In: *Metallurgical and Materials Transactions B* 42.6 (2011), pp. 1201–1210.

[145] T. Wondrak, S. Eckert, G. Gerbeth, F. Stefani, K. Timmel, A. J. Peyton, N. Terzija, and W. Yin. "Visualization of the flow in a mold of continuous casting by contactless inductive flow tomography and mutual inductance tomography." In: *Steel research international* 85.8 (2014), pp. 1266–1273.

[146] T. Wondrak and M. Soleimani. "A novel metal flow imaging using electrical capacitance tomography." In: *Measurement Science and Technology* 28.6 (2017), p. 064001.

[147] N. Yan, M. Kuehnel, S. Vasilyan, and T. Fröhlich. "Torsion balance based system for high-precision force measurement in horizontal plane. Part I: Development concept." In: *Measurement Science and Technology* (2018).

[148] B.-J. Yun, S.-K. Sim, S.-H. Hwang, and G. C. Park. "Local characteristics of two-phase flow parameters in an annulus boiling channel." In: *KSME International Journal* 11.4 (1997), pp. 443–456.

[149] M. Zec. "Theory and numerical modelling of Lorentz force eddy current testing." PhD thesis. Technische Universität Ilmenau, 2012.

[150] C. Zhang, S. Eckert, and G. Gerbeth. "Experimental study of single bubble motion in a liquid metal column exposed to a DC magnetic field." In: *International journal of multiphase flow* 31.7 (2005), pp. 824–842.

[151] C. Zhang, S. Eckert, and G. Gerbeth. "The flow structure of a bubble-driven liquid-metal jet in a horizontal magnetic field." In: *Journal of Fluid Mechanics* 575 (2007), pp. 57–82.

[152] C. Zhang. "Liquid metal flows driven by gas bubbles in a static magnetic field." PhD thesis. Technische Universität Dresden, 2009.

[153] J. Zhang and M.-J. Ni. "Direct simulation of multi-phase MHD flows on an unstructured Cartesian adaptive system." In: *Journal of Computational Physics* 270 (2014), pp. 345–365.

[154] J. Zhang and M.-J. Ni. "What happens to the vortex structures when the rising bubble transits from zigzag to spiral?" In: *Journal of Fluid Mechanics* 828 (2017), pp. 353–373.

[155] J. Zhang, M.-J. Ni, and R. Moreau. "Rising motion of a single bubble through a liquid metal in the presence of a horizontal magnetic field." In: *Physics of Fluids (1994-present)* 28.3 (2016), p. 032101.

Acknowledgements

The present work has been financed by the Deutsche Forschungsgemeinschaft (DFG) within the Research Training Group Lorentz Force Velocimetry and Lorentz Force Eddy Current Testing (GRK 1567). The support by Helmholtz Alliance - Liquid Metal Technologies (LIMTECH) in the framework of the Young Investigator Group (YIG) is also gratefully acknowledged.

I am deeply indebted to my supervisor **Prof. Christian Karcher** who has initiated and then supervised my work by giving valuable advices and setting the directions. His support is indispensable. I am particularly grateful to **Dr. Thomas Boeck** for countless number of times when we sit together to discuss the obtained results. The door to his office was always open for me asking any questions. His help and contribution are irreplaceable in my work. I wish to extend my thanks to **Prof. André Thess**, **Prof. Yuri Kolesnikov**, **Dr. Christian Resagk**, **Prof. Thomas Fröhlich**, **Prof. Christian Cierpka** and **Prof. Jörg Schumacher** for the fruitful suggestions and comments during our scientific discussions. My special thanks goes to **Dr. Thomas Wondrak**, whose long discussions and patient explanations enriched my understanding of measurement techniques. I would like to express my gratitude to **Prof. Xiaodong Wang** and **Prof. Mingjiu Ni** who hosted and supervised my scientific stay in University of Chinese Academy of Sciences. I also appreciate **Jincan Zheng** who helped on the experiment of bubble rising under ambient magnetic field in Beijing. My appreciation goes to RTG colleagues for the cooperative environment, particularly, **Ninh Tran** for her very strong support on the numerical modelings, **Rafael Marangoni** and **Na Yan** for their help on the dynamic compensation of IOFS, **Till Zürner** for his advice on UDV measurement, **Dr. Daniel Hernandez** for his help on the Comsol model, **Dr. Nataliia Dubovikova** for helpful comments on Time-of-flight measurement, **Dr. Christiane Heinicke** for her long email from Mars of experimental hints, **Andreas Wiederhold** for discussion on new measurement results and **Sebastian Prinz** for the interesting side-project of rotating-permanent magnet. It is my pleasure to thank the experimental support of **Stefan Wahler**, **David Suarez-Burgos**, **Erik Nestler**, **Nikolay Lukin** and **Jonas Ketterer** with whom we have been staying long in the labs. I also wish to thank **Alexander Thieme**, **Helmut Hoppe**, **Vigimantas Mitschunas**, **Björn Herrnberger**, **Stefan Buchelt** and **Eckhard Roth** for their great technical supports. I wish to record my special gratitude to **Colette Wilhelm**, **Cindy Karcher**, **Janine Roth** and **Dr. Ulrich Lüdtke** who helped me a lot on administrative issues.

I would like to address thanks to my parents for raising me and their constant support. A special gratitude goes to my wife, **Shangdan Yang**, who supported me patiently for years and helped me through the depressing moments. To her I dedicate this thesis.

Erklärung

(gemäß Anlage 1 der Promotionsordnung der TU Ilmenau – Allgemeine Bestimmungen)

Ich versichere, dass ich die vorliegende Arbeit ohne unzulässige Hilfe Dritter und ohne Benutzung anderer als der angegebenen Hilfsmittel angefertigt habe. Die aus anderen Quellen direkt oder indirekt übernommenen Daten und Konzepte sind unter Angabe der Quelle gekennzeichnet.

Bei der Auswahl und Auswertung folgenden Materials haben mir die nachstehend aufgeführten Personen in der jeweils beschriebenen Weise unentgeltlich geholfen:

1. Die fachliche Betreuung der Arbeit erfolgte durch apl. Prof. Dr. Christian Karcher.
2. Sehr hilfreiche fachliche Diskussionen wurden zudem mit Prof. Dr. Andre Thess, Prof. Dr. Yuri Kolesnikov und Dr. Christian Resagk geführt.
3. Die dynamische Charakterisierungen des Kraftsensors in Kapitel 2.5.2 wurden von M.Sc. Rafael Marangoni durch fachliche Hinweise unterstützt.
4. Die numerischen Modellierungen in Kapitel 3.4.1 wurden von PD. Dr. Thomas Boeck durch fachliche Hinweise unterstützt.
5. Die numerische Modellierungen in den Kapiteln 3.4.2 und 4.3 wurden von M.Sc. Ninh Tran durch fachliche Hinweise unterstützt.
6. Das Experiment in Kapitel 4.5 hat M.Sc. Jincan Zheng (University of Chinese Academy of Sciences (UCAS), Peking, VR China) durch fachliche Hinweise unterstützt. Dieses Experiment wurde von mir im Rahmen eines wissenschaftlichen Gastaufenthalts an der UCAS durchgeführt.
7. Zu einigen Messungen haben folgende Studierende der TU Ilmenau im Rahmen ihrer Anstellung als studentische Assistenten beigetragen: Stefan Wahler (Kapitel 3.2), David Suarez-Burgos und Erik Nestler (Kapitel 3.3) sowie Nikolay Lukin und Jonas Ketterer (Kapitel 4.2 und 4.4).
8. Dr. Thomas Wondrak (Helmholtz-Zentrum Dresden Rossendorf) hat diese Dissertation im rein redaktionellen Sinn (Sprache, Grammatik, Rechtschreibung) Korrektur gelesen.

Es wurden keine inhaltlichen Änderungen, Ergänzungen oder weitere Beiträge von den aufgeführten Personen vorgenommen. Weitere Personen waren an der inhaltlich-materiellen

Erstellung der vorliegenden Arbeit nicht beteiligt. Insbesondere habe ich hierfür nicht die entgeltliche Hilfe von Vermittlungs bzw. Beratungsdiensten (Promotionsberater oder anderer Personen) in Anspruch genommen. Niemand hat von mir unmittelbar oder mittelbar geldwerte Leistungen für Arbeiten erhalten, die im Zusammenhang mit dem Inhalt der vorgelegten Dissertation stehen.

Die Arbeit wurde bisher weder im In- noch im Ausland in gleicher oder ähnlicher Form einer Prüfungsbehörde vorgelegt.

Ich bin darauf hingewiesen worden, dass die Unrichtigkeit der vorstehenden Erklärung als Täuschungsversuch bewertet wird und gemäß § 7 Abs.10 der Promotionsordnung den Abbruch des Promotionsverfahrens zur Folge hat.

Ilmenau, 06. November 2018

Ze Lyu